BRNO UNIVERSITY OF TECHNOLOGY

Faculty of Electrical Engineering
and Communication

DOCTORAL THESIS

Brno, 2024   Ing. Radim Zedka

BRNO UNIVERSITY OF TECHNOLOGY

FACULTY OF ELECTRICAL ENGINEERING AND COMMUNICATION

FAKULTA ELEKTROTECHNIKY
A KOMUNIKAČNÍCH TECHNOLOGIÍ

DEPARTMENT OF RADIO ELECTRONICS

ÚSTAV RADIOELEKTRONIKY

SPATIAL DIVERSITY AND TIME-FREQUENCY ORTHOGONALITY FOR ROBUST WIRELESS COMMUNICATIONS

PROSTOROVÁ DIVERZITA A ČASOVĚ-KMITOČTOVÁ ORTOGONALITA
PRO ROBUSTNÍ BEZDRÁTOVÉ KOMUNIKACE

DOCTORAL THESIS

DIZERTAČNÍ PRÁCE

AUTHOR   Ing. Radim Zedka
AUTOR PRÁCE

SUPERVISOR   doc. Ing. Tomáš Götthans, Ph.D.
ŠKOLITEL

SECONDARY SUPERVISOR prof. Ing. Roman Maršálek, Ph.D.
ŠKOLITEL SPECIALISTA

BRNO 2024

ABSTRACT

This dissertation thesis contains several contributions in the field of robust wireless communications. The first part is focused on developing and analyzing a novel technique of spatial diversity based on the recently discovered concept of space-time line codes (STLCs). Unlike the already known orthogonal STLC, this design is based on a quasi-orthogonal code structure which allows the utilization of four receiver antennas instead of two antennas, which is the limit of the orthogonal STLC for a full rate transmission. The work provides a rigorous theoretical analysis of the diversity gain and asymptotic SNR gain of the new STLC and compares it to the benchmark STLCs. The second part deals with the orthogonal-time-frequency-space (OTFS), a popular multi-carrier waveform showing excellent performance in high-mobility wireless communications. The contribution lies in designing a new OTFS-like system, which - unlike the vast majority of OTFS literature - considers the power-spectral-density (PSD) one of the key design parameters. The novel waveform is named unique-word OTFS (UW-OTFS), because its outer stage is adopted from the popular UW-OFDM. UW-OTFS inherits all of its benefits, including the improved bit-error-ratio (BER) and superb PSD properties. Moreover, the main issue of UW-OFDM, i.e., the multiple-tap equalization, is no longer problematic in the OTFS context. The proposed UW-OTFS is designed to operate in linear time-variant (LTV) fractional-Doppler channels by utilizing a modification of the basis-expansion-model (BEM). Due to this method, both the channel estimation and equalization are performed by the linear minimum-mean-square-error (LMMSE) technique. The proposed system is analyzed both theoretically and numerically (using the Monte Carlo method) and it shows excellent performance in fractional-Doppler channels.

KEYWORDS

STLC, quasi-orthogonal, STBC, unique word, OTFS, LMMSE.

ABSTRAKT

Předložená disertační práce přispívá do oblasti robustních bezdrátových komunikací dvěma zásadními nově navrženými technikami. První část práce je zaměřena na vývoj a analýzu nové techniky prostorové diverzity založené na nedávno objeveném konceptu časoprostorových kódů STLC. Na rozdíl od již známého ortogonálního STLC je tento návrh založen na kvazi-ortogonální kódové struktuře, která umožňuje použití čtyř antén přijímače namísto dvou, jak je tomu u ortogonálních STLC s plnou rychlostí. Práce obsahuje rigorózní teoretickou analýzu diverzitního zisku a asymptotického zisku poměru signál-šum (SNR) u nového STLC a porovnává je s dosud známými přístupy publikovanými v oblasti STLC. Druhá část se zabývá OTFS, v současnosti prudce se rozvíjející technikou přenosu dat s více nosnými, která vykazuje vynikající výsledky zejména v bezdrátové komunikaci uživatelů s vysokou mobilitou. Zde je prezentován nový systém založený na principu OTFS, který – na rozdíl od naprosté většiny OTFS publikací – jako jeden z klíčových návrhových parametrů využívá výkonovou spektrální hustotu (PSD) vysílaného signálu. Tento systém byl pojmenován UW-OTFS, protože jeho vnější stupeň je převzat z aktuálně rozšířeného systému UW-OFDM. UW-OTFS přebírá všechny výhody UW-OFDM, včetně vylepšené bitové chybovosti (BER) a definované spektrální výkonové hustoty zaručující výrazné omezení vyzařování do sousedních kanálů. S využitím konceptu OTFS navíc zaniká hlavní nevýhoda UW-OFDM, kterou je nemožnost použít ekvalizaci typu one-tap, tedy ekvalizace s jedním koeficientem. Systém UW-OTFS je navržen tak, aby pracoval v časově variantních kanálech s neceločíselným Dopplerovským posuvem, a to především díky využití modifikace známé metody BEM. Díky této metodě jsou jak odhad kanálu, tak ekvalizace prováděny technikou LMMSE. Navržený systém je následně analyzován jak teoreticky, tak numericky, a to pomocí metody Monte Carlo.

KLÍČOVÁ SLOVA

STLC, kvazi-ortogonální, STBC, unique word, OTFS, LMMSE.

Author's Declaration

Author:	Ing. Radim Zedka
Author's ID:	164441
Paper type:	Doctoral thesis
Academic year:	2023/24
Topic:	Spatial Diversity and Time-Frequency Orthogonality for Robust Wireless Communications

I declare that I have written this paper independently, under the guidance of the advisor and using exclusively the technical references and other sources of information cited in the paper and listed in the comprehensive bibliography at the end of the paper.

As the author, I furthermore declare that, with respect to the creation of this paper, I have not infringed any copyright or violated anyone's personal and/or ownership rights. In this context, I am fully aware of the consequences of breaking Regulation §11 of the Copyright Act No. 121/2000 Coll. of the Czech Republic, as amended, and of any breach of rights related to intellectual property or introduced within amendments to relevant Acts such as the Intellectual Property Act or the Criminal Code, Act No. 40/2009 Coll. of the Czech Republic, Section 2, Head VI, Part 4.

Brno . . . .

                                                      author's signature*

---

*The author signs only in the printed version.

ACKNOWLEDGEMENT

Contents

Introduction

Scientific research is a journey. It reflects the core need of an individual to gain knowledge and pursue whatever it is that drives us to a better understanding of the world. The path of a researcher is hardly ever consistent or loyal to a single topic and it often deviates in the process. My doctoral thesis is no exception. It contributes into two different branches of wireless communication. Hence the need to structure the work in two (mostly) separate parts.

The first part of the thesis is more theoretical in nature, situated into the field of narrowband spatial diversity communication systems. It rides the wave of a recently resurrected topic of space-time coding, which was in the spotlight of wireless communication and information theoretic researchers around year 2000. In the meantime, space-time block codes (STBC) became an integral part of many wireless communication standards for increasing the diversity gain, thus trading spectral efficiency for the system complexity.

Almost 20 years later, when base stations became massively populated by antennas, the STBC was reworked into the space-time line codes (STLC), which have a very similar properies, however, their MIMO topology is mirrored. While STBC proves useful in $M \times N$ topologies with $M \leq 4$ and $N \in \mathbb{N}$, STLC operates best in the $N \times M$ topology. Also, while STBC requires channel knowledge on the receiver, STLC uses it on the transmitter. This reflects the recent trend in the time-division-duplex (TDD) operation, where the channel knowledge is obtained in one direction (e.g., uplink) and used in the other (e.g., downlink). The discovery of STLC triggered a new wave of interest in the STBCs, since they are directly used for the STLC design. In my work, I once again revived the discussion of whether the four-TX-antenna STBC can achieve full diversity in a frequency-flat Rayleigh channel. Our work in this field brought interesting conclusions that are directly applicable for the design of STLCs.

The second part of the thesis deals with a much more practical area of wireless communications, more specifically, with the design of a broad-band multicarrier waveform called the Orthogonal-Time-Frequency-Space (OTFS). Due to growing demands of higher data-rates and lower latency, communication bandwidth increases accordingly and so does the need for effective spectrum utilization and protection from multi-path fading. In addition to that, the wireless communications are expected to cope with high mobility scenarios, where the channel is considered as linear and time-variant. The OTFS was first introduced in 2017 as a new waveform suitable for the high-mobility channels and it quickly became the number-one research topic in this area.

Our contribution in this field involves design of a new OTFS-based waveform

called the Unique-Word OTFS (UW-OTFS). That uses the benchmark Unique-Word Orthogonal-Frequency-Division-Multiplexing (UW-OFDM) as a modulator/demodulator, for its excellent spectral and energy efficiency. The UW-OTFS is designed to match (and in many aspects outperform) the benchmark OTFS designs in terms of spectral efficiency, Bit-Error-Ratio (BER), Peak-to-Average Power Ratio (PAPR), Out-of-Band (OOB) emissions and overall complexity.

Thesis Goals

The foundations of my research, regarding the field of narrow-band *Multiple Input Multiple Output* (MIMO) communications with focus on the *Space Time Block Code* (STBC) and *Space Time Line Code* (STLC) are discussed in the first part of the doctoral thesis. This part of the doctoral thesis is based on my first-author publications [1] and [2].

I have also been interested in the *Single Carrier* (SC) waveforms, especially in the beginning of my doctoral studies. In [3], I examined the performance of various STBC schemes implemented into the SC and *Orthogonal Frequency Domain Multiplexing* (OFDM) waveforms. Later, in [4] I compared the classic *Single-Carrier Frequency Domain Equalization* (SC-FDE) with a time-domain equalized SC in terms of spectral efficiency in frequency selective channels. In [5], I colaborated on the 802.11ay SC-PHY simulator for 60 GHz channels. Even though none of these works fit into the topic of the doctoral thesis, they were a valuable experience in my scientific journey towards my dissertation thesis.

My internship in TU Wien in 2021 steered my focus into another research topic - the *Orthogonal Time Frequency Space* (OTFS). Despite my best efforts, OTFS, for being a broad-band waveform, could hardly be related to the original dissertation topic, which was the STLC, i.e., originally a narrow-band technique. This is the reason for splitting the thesis into two parts, where the common denominator lies in the field of robust wireless communications. I have been working on OTFS ever since the internship and the results of more than two years of my work can partly be seen in [6] (where I am the second author), yet most of my efforts were put into [7]. The main goals of the thesis can now be defined as:

- Design and evaluation of a new full rate STLC with four receiver antennas.
- Design and evaluation of a new OTFS-based waveform adopting the frequency domain guard band and the *Unique Word* (UW) to the OTFS.

These goals are further elaborated in Sections 1.2 and 4.3, respectively.

Thesis Outline

The first part of the thesis is structured as follows: Chapter 1 contains an overview of the relevant STLC publications and summarizes the main contributions of the first part of the thesis. Chapter 2 defines some of the concepts and techniques frequently-used in the spatial diversity field. Chapter 3 contains the main contribution, which is a theoretical analysis of the conditional *Signal to Noise Ratio* (SNR)'s *Probability Density Function* (PDF) for all discussed techniques. Its remainder is devoted to the proposed STLC, specifically to the derivation of its PDF, average SNR, average

Bit Error Ratio (BER), diversity gain and asymptotic SNR gain. The last chapter of the first part is the Conclusion.

Part two begins with Chapter 4, which discusses the state-of-the-art OTFS publications, the motivation which lead to the proposal of the *Unique-Word Orthogonal Time Frequency Space* (UW-OTFS) and which introduces the main contributions of the second part of the thesis. Chapter 5 introduces the necessary background for understanding the proposed OTFS design, which is then the content of Chapter 6. That is structured into several sections, dealing with the UW-OTFS transmitter design, the proposed UW sequence example, channel estimation, data estimation, analysis of the Doppler Scaling Factor (DSF), comparison with a conventional OTFS and numerical simulations. The second part ends with its own conclusion. Chapter A contains the appendices.

Reproducibility

I believe that reproducibility is a key aspect of a quality scientific publication, therefore, I decided to share the MATLAB scripts of the proposed UW-OTFS to GitHub. Please refer to `https://github.com/rzedka/UW-OTFS-Simulator`.

Part I

Narrow-band Spatial Diversity Techniques

1   State-of-the-Art

Nowadays, in the field of wireless communication, a development of appropriate spatial diversity techniques for MIMO systems is in the spotlight of many research activities. The recently discovered STLC [8] is built on the concept of STBC with *Channel State Information* (CSI) located on the *Transmitter* (TX) side rather than the *Receiver* (RX) side. The STLC is the answer for high base-station antenna counts needed for advanced wireless communication systems. It allows having low-complexity (linear decoding) user terminal receivers with more than one antenna and with no or partial request of CSI at the RX side [8–10].

1.1   STLC

The pioneering work of Joung [8] introduced the *Orthogonal Space Time Line Code* (OSTLC), offering full diversity (spatial diversity gain equal to the product of TX and RX antennas) and in the case of having 2 RX antennas also full code rate (the number of information symbols matches the STLC length). For more efficient utilization of multiple TX antennas, the *Transmit Antenna Selection* (TAS) for $M \times 2$ OSTLC (where M is the TX antenna count) was developed in [9]. Later, the ergodic capacity of TAS for an OSTLC-based system employing four RX antennas was analyzed [11].

Recently, there has been an effort to extend the RX antenna count to four while preserving full code rate and full diversity. However, the design of OSTLC with more than two RX antennas generally suffers from code rate reduction due to compensation for having full diversity [8, 9, 11].

Even though the quantity of STBC literature is extensive, many popular STBC ideas, such as the signal constellation technique published in [12], are dependent on computationally very demanding decoding methods, such as the *Maximum Likelihood* (ML) detection. Those STBC ideas cannot be easily adopted for the STLC concept, which often uses linear decoding (using only addition and complex conjugation) and whose main computational burden lies on the TX side.

The Linear Toeplitz delay-diversity codes [13], the overlapped Alamouti codes [14] and the Group-Orthogonal Toeplitz codes [15] could also be of benefit to the STLC, due to their linear decoding and close-to-orthogonal performance.

Below are listed some of the current STLCs with four RX antennas. In [10], a compromise between the spatial diversity and spatial multiplexing gain for four RX antennas was achieved. Later, this idea was generalized for any even number of RX antennas [16], however, the multiplexing gain is not in the focus of our research. In [17], the attention was turned to achieving full code rate and full diversity in the

$M \times 4$ scheme for $M \to \infty$, however, no proof of full diversity was made in the case where $M \in \mathbb{N}$. Another elegant STLC solution based on the Golden code for 1×4 and 2×4 schemes, achieving full diversity, using a non-linear decoding algorithm emerged in [18]. Unfortunately, this idea cannot be extended for M TX antennas. A novel STLC based on the quasi-orthogonal space-time matrix [19] was proposed in our work [1], which outperforms the previously designed concept [17] in terms of average BER for small M.

1.2 Quasi-Orthogonal STLC - Scientific Contribution

Motivated by recent research activities in the field of STLCs, we proposed a novel full-rate *Quasi-orthogonal Space Time Line Code* (QSTLC) with linear decoding in [2]. We improved the STLC precoding scheme from our previous work [1], which now more tightly approaches the ideal $M \times 4$ STLC with full-diversity (Lemma 1 in [17]) and which also exhibits a full code rate. The PDF and the average BER performance of the proposed full-rate QSTLC are identical to the *Quasi-orthogonal Space Time Block Code* (QSTBC) presented in [20], where the researchers proved its full-diversity equal to $4M$ for the limiting case where $M \to \infty$. However, a rigorous analysis of the diversity gain for $M \in \mathbb{N}$ is missing. In [21], the same authors provided an analytical description of the PDF for $M = 1$ which we used in [2] to obtain the PDF of the proposed system for any $M \in \mathbb{N}$. Next, we calculated the exact diversity gain for $M \in \mathbb{N}$ and proved that it equals $2M$ and not $4M$ as was proven for the case $M \to \infty$. Since the proposed system matches the full-rate $M \times 2$ OSTLC in diversity gain, we evaluate their asymptotic difference in SNR (i.e., the asymptotic SNR gain) analytically. Finally, we compared the proposed FR-QSTLC with other state-of-the-art STLCs with linear decoding in terms of average BER and its derivative (which converges to the diversity gain for high E_b/N_0).

The contribution of the first part of the thesis is listed below:

1. A new STLC based on the QSTBC is introduced.
2. A thorough theoretical analysis of its diversity gain and asymptotical SNR gain is provided.
3. The proposed QSTLC is compared to the benchmark full-rate $M \times 4$ STLCs.

2 Introduction to Spatial Diversity Techniques

This chapter introduces some of the main concepts in the narrow-band spatial diversity systems which are then referred to in the following chapters.

2.1 Preliminaries

2.1.1 Narrow-band and Broad-band systems

The narrow-band and broad-band systems definition highly depends on the context of the discussion. In some research areas a system occupying 100 MHz of bandwidth may be labeled as narrow-band while in other areas it is a clear characteristic of a broad-band system.

In the context of this thesis, narrow-band systems are those whose bandwidth is smaller than coherence bandwidth of the channel and the channel model consists of complex channel gain [22]. The broad-band system channel model consists of a set of complex coefficients which together form the *Channel Impulse Response* (CIR).

2.1.2 Transmitter Signal to Noise Ratio

In order to present a fair comparison between MIMO systems with different counts of TX and RX antennas, constraints must be applied on the total TX power (in case of multiple TX antennas). For this purpose, the statistical operator named expected value $\mathrm{E}\{.\}$ is utilized. The m-ary *Quadrature Amplitude Modulation* (QAM) symbols at each one of $0 \geq p \geq N_T - 1$ TX antennas are looked at as independent, identically distributed (i.i.d) zero-mean complex random variables s_{p_n} with variance $\sigma_{s_p}^2 = \mathrm{E}\{|s_{p_n}|^2\}$. The receiver noise w_{q_n} is considered i.i.d zero-mean joint-complex Gaussian random variable with variance $\sigma_w^2 = \mathrm{E}\{|w_{q_n}|^2\}$ which is identical at each one of $0 \geq q \geq N_R - 1$ RX antennas. Finally, the TX SNR ρ is defined as

$$\rho = \frac{1}{\sigma_w^2} \sum_{p=0}^{N_T-1} \sigma_{s_p}^2 = \frac{\sigma_s^2}{\sigma_w^2}. \tag{2.1}$$

2.1.3 Ratio of Bit Energy to Noise Power Spectral Density

This performance measure, denoted E_b/N_0, is widely used in the literature alongside TX SNR, especially in order to compare systems that use various modulation formats with specific ratios of bits per symbol. E_b/N_0 is related to the TX SNR ρ according to

$$E_b/N_0 = \frac{\rho}{k_b}, \tag{2.2}$$

where k_b is the ratio of bits per time-domain sample.

2.1.4 Receiver Signal-to-Noise Ratio

The RX SNR, (also called conditional SNR) is a performance measure closely related to the TX SNR ρ. While ρ describes a ratio of total TX variance to the RX noise, SNR Ξ is purely a parameter of the RX side defined as a ratio of the decoded signal component to the sum of noise components [23]. In this work, SNR is treated as a random variable dependent on the channel coefficients, therefore, it is described by the PDF which is a function of Ξ and ρ. It is defined by $f_\Xi(\xi, \rho)$ where $\xi, \rho \in \langle 0, \infty \rangle$.

2.1.5 Bit Error Ratio

BER is the number-one performance measure in communication technology. It is defined as the ratio of successfully received data bits to the quantum of transmitted data and it is often defined as a function of path gain ρ or SNR. It is possible to analytically calculate BER from the PDF of the conditional SNR.

Conditional BER in models with normally-distributed RX noise-interference component is calculated with the Gaussian Q-function defined as

$$Q(x) = \frac{1}{\sqrt{2\pi}} \int_x^\infty e^{-\frac{u^2}{2}} \, du, \tag{2.3}$$

wherein our case, $x \geq 0$ is a quantity normalized by the standard deviation σ. The conditional BER formula for 4-QAM and 16-QAM constellations with gray-code bit mapping yields

$$\varepsilon(\Xi) = Q\left(\sqrt{\Xi}\right), \tag{2.4}$$

and

$$\varepsilon(\Xi) = \frac{1}{4}\left(3Q\left(\sqrt{\frac{\Xi}{5}}\right) + 2Q\left(\sqrt{\frac{9\Xi}{5}}\right) - Q\left(\sqrt{5\Xi}\right)\right), \tag{2.5}$$

respectively, where Ξ represents the conditional SNR.

In order to provide fair comparison between various communication systems we are often interested in *Average Bit Error Rate* (ABER) which is obtained:

- numerically - by averaging conditional BER over a sufficient number of channel realizations
- analytically - by using the *Law Of The Unconscious Statistician* (LOTUS) as in [2].

In the latter case, ABER $\bar{\varepsilon}(\rho)$ is calculated from conditional BER $\varepsilon(\Xi)$ and SNR PDF $f_\Xi(\xi, \rho)$ by

$$\bar{\varepsilon}(\rho) = \int_0^\infty \varepsilon(\xi) f_\Xi(\xi, \rho) \, d\xi. \tag{2.6}$$

2.1.6   Diversity Gain

Diversity gain is a key performance measure in describing MIMO systems with spatial diversity as their main characteristic. It is the limit of $\rho \to \infty$ of the ABER - path gain relation, written mathematically as

$$\mathcal{D} = -\lim_{\rho \to \infty} \frac{\partial \log_{10}(\bar{\varepsilon}(\rho))}{\partial \log_{10}(\rho)} = -\lim_{\rho \to \infty} \frac{\log_{10}(\bar{\varepsilon}(\rho))}{\log_{10}(\rho)}, \qquad (2.7)$$

and its typical unit is a decade per 10 dB of path gain.

2.1.7   Peak-to-Average Power Ratio

Peak to Average Power Ratio (PAPR) is frequently stated as one of the key design parameters in this work. It is worth mentioning that PAPR is related to systems with non-zero carrier frequencies and that for base-band models discussed here, *Peak to Mean-Average Power Ratio* (PMEPR) is more accurate. In m-QAM pass-band modulations (i.e. with non-zero carrier frequency), PAPR is 3 dB higher than PMEPR [24], however, because all systems in this work use m-QAM base-band models and absolute PAPR/PMEPR values are not relevant, PAPR is stated as an acronym throughout the whole work.

2.1.8   PAPR Penalty

The PAPR penalty is often recognized in STBC systems whose space-time matrices contain zero entries, e.g., schemes defined by (40), (41) and (79) in [25]. In that case, the TX energy regularly drops to zero, causing increased PAPR if compared to, e.g., the Alamouti scheme or the QSTBC in [19]. However, PAPR can be increased also by linearly transforming the input m-QAM symbol, e.g., by using the *Inverse Fast Fourier Transform* (IFFT) in the OFDM waveform.

Therefore, in this work the PAPR penalty of a given spatial diversity system is defined as an increase in PAPR related to the PAPR of the input m-QAM constellation.

2.2   Introducing Spatial Diversity Techniques

As it was previously remarked, most of the spatial-diversity techniques were developed for use in narrow-band systems. Listed below are some of the most influential MIMO spatial diversity techniques which are further referred to in this thesis.

2.2.1 Maximum-Ratio-Combining

The oldest of the *Single Input Multiple Output* (SIMO) techniques, *Maximum Ratio Combining* (MRC), was first published in [26] as a means to maximize the SNR by increasing the number of RX antennas. Its main characteristics are:

- CSI is only required on the RX side
- theoretically unlimited RX antenna count
- TX antenna count limited to one
- no PAPR penalty.

MRC offers a possibility of performing channel estimation on the RX side using pilot sequences, therefore, it is fully operational in both simplex and *Time Division Duplex* (TDD) communication modes.

A $1 \times M$ MRC system has a diversity gain equal to M, measured in decades of ABER per 10 dB of ρ. Full definition of the MRC can be found in Section 3.1.1.

2.2.2 Maximum-Ratio-Transmission

Although it was defined for a general $M_T \times M_R$ MIMO channel [27], in this thesis, *Maximum Ratio Transmission* (MRT) will be used in the case of $M_R = 1$, where it behaves as an exact counterpart to the MRC. Its main characteristics are symmetrical to those of the MRC:

- CSI is only required on the TX side (assuming use of TDD reciprocal channel)
- number of TX antennas is not limited (theoretically)
- RX antenna count limited to one
- increased PAPR due to TX precoding.

The fact that CSI is required on TX side obliges MRT to operate exclusively in downlink direction of the TDD communication mode where the base station may obtain CSI during an uplink transmission (e.g. using MRC and pilot sequences), provided that CSI is identical in both uplink and downlink. The diversity gain of an $M \times 1$ MRT system equals M. Full definition of the MRT can be found in Section 3.1.2.

2.2.3 Space-Time Block Codes

With the advent 3G mobile terminals there was a need to increase the diversity gain in both uplink (terminal to base station) and downlink direction. Since implementing more antennas at the terminal was not convenient (limitations in size and number of *Radio Frequency* (RF) chains) an urgent need of another spatial diversity principle emerged. STBC was designed for *Multiple Input Single Output* (MISO) systems in order to benefit from multiple TX antennas without need of CSI on the

TX side (and related PAPR penalty). STBC evolved from its predecessor, the *Space Time Trellis Code* (STTC), which required complex ML-based decoding algorithms. The main benefit of STBC was a linear block-based decoding, operating at only a fraction of STTC's computational complexity. Its main characteristics are:

- CSI is only required on the RX side
- CSI must remain static during the STBC block
- increased latency due to STBC block size (more notable in broad-band systems with *Frequency Domain Equalization* (FDE))
- TX antenna count is explicitly determined by the STBC scheme
- SNR penalty compared to MRT and MRC
- potencial PAPR penalty - depending on the STBC scheme.

In the STBC context, we often speak about **orthogonality** and such systems are referred to as the *Orthogonal Space Time Block Codes* (OSTBCs). The orthogonality of a given STBC can be easily verified by evaluating the Hermitian product of its space-time matrix $\bar{\mathbf{s}}$ (provided that $\bar{\mathbf{s}}$ is an $N \times N$ square matrix, see Theorem 5.4.1. in [28]),

$$\bar{\mathbf{s}}^H \bar{\mathbf{s}} = \bar{\mathbf{s}}\bar{\mathbf{s}}^H = \sum_{p=0}^{N-1} |s_i|^2 \mathbf{I}. \tag{2.8}$$

Undoubtedly, the most popular OSTBCs scheme was developed by Alamouti [29], yet there are numerous other designs, each having its original attributes and functionalities. It was proved that complex-valued *Orthogonal Space Time Block Code* (OSTBC) designs with unity code-rate, full diversity and no PAPR penalty exist only for two TX antennas [28]. However, in real-valued symbol constellations (e.g. *Binary Phase Shift Keying* (BPSK)) unity code-rate and full diversity OSTBCs exist also for higher TX antenna counts.

STBCs are often combined with MRC for increasing the number of RX antennas, and consequently the diversity gain which in case of $2 \times M$ OSTBC-MRC scheme equals $2M$. Full definition of the OSTBC can be found in Section 3.1.3.

2.2.4 Quasi-Orthogonal STBC

The QSTBC is any STBC that does not satisfy the orthogonality condition in (2.8). It was first published in [19] and [30] and it is an extension of the Alamouti code (OSTBC) for 4 TX antennas. Unlike the generalized complex orthogonal designs, which preserve orthogonality and trade the number of TX antennas for the code-rate [31], QSTBCs offer a different deal by preserving full rate and relaxing the orthogonality.

QSTBCs share most of the parameters with OSTBCs (no need for CSI on the TX side, full-rate, no PAPR penalty), however, direct calculation of the diversity

gain strongly depends on the RX decoding scheme. In general, non-linear ML decoding offers better diversity gain than the linear decoding, for the cost of greater complexity of the former. QSTBCs typically avoid zero entries in the space-time matrix, therefore, there is no PAPR penalty. Full definition of the QSTBC can be found in Section 3.1.4.

2.2.5   Space-Time Line Codes

Just as MRT is a counterpart to MRC, so is STLC to STBC. The original idea of STLC was published in [8] for an $M \times 2$ MIMO topology. Some important characteristics of the STLC are:

- CSI is only required on the TX side (assuming the channel is reciprocal)
- the channel must remain static during the STLC block
- increased latency due to STLC block size (similar to STBCs)
- RX antenna count is explicitly determined by the STLC scheme
- SNR loss if compared to MRT and MRC (similar to STBCs)
- PAPR penalty due to TX precoding.

The main convenience of STLC is the absence of CSI during STLC decoding on the receiver. Unlike the differential STBC, which also does not require CSI for the RX decoding, STLC is free of the additional SNR loss naturally occurring in differential STBC [32]. Due to the symmetry between STBC and STLC, any $N \times 1$ STBC design may be transformed into a $1 \times N$ STLC as long as the STBC uses linear decoding. The TX antenna count M may then be increased arbitrarily by combining STLC and MRT. Full definition of the OSTLC can be found in Section 3.1.5. Fig. 2.1 contains block schematics all of the aforementioned MIMO techniques.
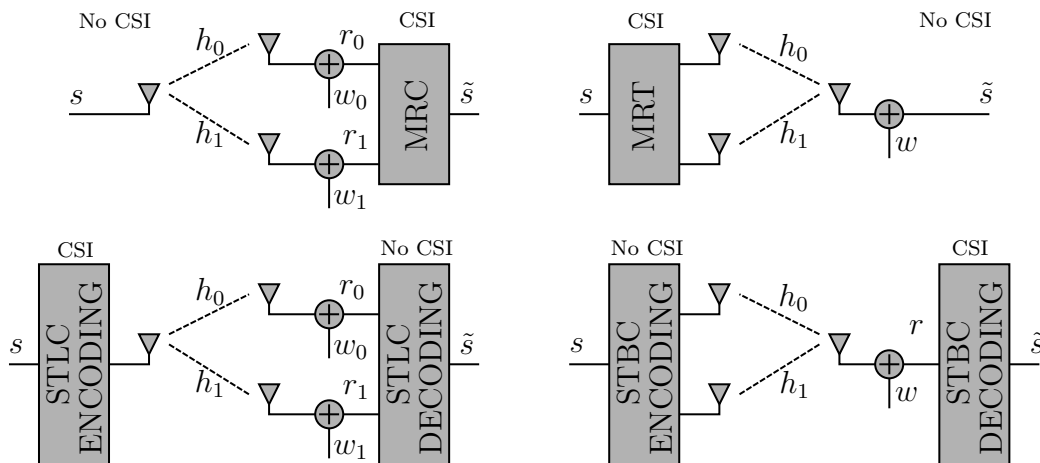
Fig. 2.1: Block diagrams of the MRC, MRT, STLC and STBC.

3 Theoretical Analysis

This chapter begins with detailed definitions of the benchmark systems, introduced in Section 2.2, as well as that of my original contribution, which is the QSTLC, described in Section 3.1.6. The chapter continues by a theoretical analysis of the proposed QSTLC published in [1] and [2], followed by analyses of the spatial-diversity techniques introduced in Section 2.2.

3.1 Detailed Definitions

3.1.1 Maximum-Ratio-Combining

One of the fundamental spatial-diversity systems is the MRC, which uses the MIMO topology $1 \times M$.

The MRC transmits the m-QAM modulated symbols directly, without any precoding. The symbol, received by the q-th RX antenna is defined as

$$r_q = h_q s + w_q, \tag{3.1}$$

where s is the m-QAM symbol of variance $\sigma_s^2 = \mathrm{E}\{|s|^2\}$, h_q is the complex channel gain, defined as a random variable $h_q \sim \mathcal{CN}(0, 1)$. The *Additive White Gaussian Noise* (AWGN) sample is defined as $w_q \sim \mathcal{CN}(0, \sigma_w^2)$.

Receiver

As the title already suggests, MRC is a combining scheme, designed to maximize the RX SNR for the $1 \times M$ MIMO topology. The result of MRC is defined as

$$\tilde{s} = \sum_{q=0}^{M-1} h_q^* r_q, \tag{3.2}$$

which expands into

$$\tilde{s} = s \sum_{q=0}^{M-1} |h_q|^2 + \sum_{q=0}^{M-1} h_q^* w_q, \tag{3.3}$$

where the signal component is a real and positive number.

3.1.2 Maximum-Ratio-Transmission

The reciprocal of MRC, MRT is used in the $M \times 1$ MIMO topology.

Transmitter

The transmitter uses a prior knowledge of CSI to precode the data symbol s differently for each TX antenna. The precoded symbol on the p-th antenna is defined as

$$v_p = \alpha h_p^* s, \tag{3.4}$$

where α is the TX normalization coefficient, defined as [27]

$$\alpha^{-2} = \sum_{p=0}^{M-1} |h_p|^2. \tag{3.5}$$

Receiver

On the receiver, without the need for further RX processing, we obtain the data symbol estimate, defined as

$$\tilde{s} = \sum_{p=0}^{M-1} h_p v_p + w, \tag{3.6}$$

which is expanded to

$$\tilde{s} = \alpha s \sum_{p=0}^{M-1} |h_p|^2 + w = \frac{1}{\alpha} s + w. \tag{3.7}$$

3.1.3 Orthogonal STBC

The most popular OSTBC is the full rate Alamouti scheme [29], defined by its space-time coding matrix

$$\bar{\mathbf{s}} = \begin{pmatrix} s_0 & s_1 \\ -s_1^* & s_0^* \end{pmatrix}. \tag{3.8}$$

OSTBC can be generalized for an arbitrary number of RX antennas M using the MRC.

Receiver

We consider that the transmitted signal is passed through a frequency-flat quasi-static fading channel (i.e., the channel remains static during one STBC block). The symbol, received at time i by the q-th RX antenna is defined as

$$r_{q,i} = \sum_{p=0}^{1} h_{p,q} \bar{\mathbf{s}}[i,p] + w_{q,i}, \quad \forall \quad q, i \in \{0, 1\}, \tag{3.9}$$

which can be written in a matrix notation as

$$\hat{\mathbf{r}}_q = \bar{\mathbf{H}}_q \mathbf{s} + \hat{\mathbf{w}}_q, \tag{3.10}$$

where $\hat{\mathbf{r}}_q = (r_{0,q} \ r_{1,q}^*)^T$, $\mathbf{s} = (s_0 \ s_1)^T$, $\hat{\mathbf{w}}_q = (w_{0,q} \ w_{1,q}^*)^T$ and

$$\bar{\mathbf{H}}_q = \begin{pmatrix} h_{0,q} & h_{1,q} \\ h_{1,q}^* & -h_{0,q}^* \end{pmatrix}. \tag{3.11}$$

The RX combining and decoding, inspired by MRC, is defined as

$$\tilde{\mathbf{s}} = \sum_{q=0}^{M-1} \bar{\mathbf{H}}_q^H \hat{\mathbf{r}}_q, \tag{3.12}$$

which is expanded into

$$\tilde{\mathbf{s}} = \sum_{q=0}^{M-1} \bar{\mathbf{H}}_q^H \bar{\mathbf{H}}_q \mathbf{s} + \sum_{q=0}^{M-1} \bar{\mathbf{H}}_q^H \hat{\mathbf{w}}_q. \tag{3.13}$$

The orthogonality of the Alamouti scheme caused the equivalent channel matrix $\bar{\mathbf{H}}_q$ to be orthogonal as well, therefore,

$$\sum_{q=0}^{M-1} \bar{\mathbf{H}}_q^H \bar{\mathbf{H}}_q = \sum_{q=0}^{M-1} \left(|h_{0,q}|^2 + |h_{1,q}|^2 \right) \mathbf{I}, \tag{3.14}$$

which is a proof, that the signal component in (3.13) has no self-interference.

3.1.4 Quasi-Orthogonal STBC

The $4 \times M$ QSTBC scheme described below represents the counter-part of our $M \times 4$ QSTLC, proposed in [1]. The TX part is fully defined by the space-time matrix (formula (5) in [19])

$$\bar{\mathbf{s}} = \begin{pmatrix} s_0 & s_1 & s_2 & s_3 \\ -s_1^* & s_0^* & -s_3^* & s_2^* \\ -s_2^* & -s_3^* & s_0^* & s_1^* \\ s_3 & -s_2 & -s_1 & s_0 \end{pmatrix}, \tag{3.15}$$

while the decoding scheme utilizes the MRC idea in order to exploit an arbitrary number RX antennas M. The vector of four RX symbols on the q-th RX antenna is given by

$$\hat{\mathbf{r}}_q = \bar{\mathbf{H}}_q \mathbf{s} + \hat{\mathbf{w}}, \tag{3.16}$$

where $\hat{\mathbf{r}}_q = (r_{0,q} \ r_{1,q}^* \ r_{2,q}^* \ r_{3,q})^T$, $\mathbf{s} = (s_0 \ s_1 \ s_2 \ s_3)^T$ and $\hat{\mathbf{w}}_q = (w_{0,q} \ w_{1,q}^* \ w_{2,q}^* \ w_{3,q})^T$, and where the equivalent channel matrix of the q-th RX antenna yields

$$\bar{\mathbf{H}}_q = \begin{pmatrix} h_{0,q} & h_{1,q} & h_{2,q} & h_{3,q} \\ h_{1,q}^* & -h_{0,q}^* & h_{3,q}^* & -h_{2,q}^* \\ h_{2,q}^* & h_{3,q}^* & -h_{0,q}^* & -h_{1,q}^* \\ h_{3,q} & -h_{2,q} & -h_{1,q} & h_{0,q} \end{pmatrix}. \tag{3.17}$$

The Hermitian product $\bar{\mathbf{H}}_q^H \bar{\mathbf{H}}_q$ is then evaluated as

$$\bar{\mathbf{H}}_q^H \bar{\mathbf{H}}_q = Y_q\big(\mathbf{I} + X_q\mathbf{Q}\big), \tag{3.18}$$

where

$$Y_q = \sum_{i=0}^{3} |h_{i,q}|^2 \quad\text{and}\quad X_q = \frac{2}{Y_q}\Re\{h_{0,q}h_{3,q}^* - h_{1,q}h_{2,q}^*\}, \tag{3.19}$$

and where

$$\mathbf{Q} = \begin{pmatrix} 0 & 0 & 0 & 1 \\ 0 & 0 & -1 & 0 \\ 0 & -1 & 0 & 0 \\ 1 & 0 & 0 & 0 \end{pmatrix}. \tag{3.20}$$

We can see that (3.18) is not a scaled unit matrix, and therefore, it is not orthogonal. The goal of the RX processing is to remove this non-orthogonality so that the self-interference caused by $\mathbf{Q}$ is mitigated. However, unlike in OSTBC, in QSTBC there are two ways to combine and decode the RX symbols, due to the quasi-orthogonal nature of the code. They will be referred to as "m1" and "m2", for method one and two, respectively.

RX Combining - Method One

The first method of the RX combining is defined by

$$\tilde{\mathbf{s}} = \sum_{q=0}^{M-1} \bar{\mathbf{M}}_q \bar{\mathbf{H}}_q^H \hat{\mathbf{r}}_q, \tag{3.21}$$

where $\bar{\mathbf{M}}_q$ is the orthogonalization matrix, defined as

$$\bar{\mathbf{M}}_q = Y_q\big(\mathbf{I} - X_q\mathbf{Q}\big), \tag{3.22}$$

Now, due to the property $\mathbf{Q}\mathbf{Q} = \mathbf{I}$, we obtain

$$\bar{\mathbf{M}}_q \bar{\mathbf{H}}_q^H \bar{\mathbf{H}}_q = Y_q^2\big(1 - X_q^2\big)\mathbf{I}, \tag{3.23}$$

where the absence of $\mathbf{Q}$ proves that the interference (i.e., non-orthogonality) has been removed.

RX Combining - Method Two

The second method is specific by having a single decoding matrix $\bar{\mathbf{M}}$ common for all RX antennas and it is defined as

$$\tilde{\mathbf{s}} = \bar{\mathbf{M}} \sum_{q=0}^{M-1} \bar{\mathbf{H}}_q^H \hat{\mathbf{r}}_q, \tag{3.24}$$

and because

$$\sum_{q=0}^{M-1} \bar{\mathbf{H}}_q^H \bar{\mathbf{H}}_q = \sum_{q=0}^{M-1} Y_q \big(\mathbf{I} + X_q \mathbf{Q}\big) = Y\mathbf{I} + \sum_{q=0}^{M-1} Y_q X_q \mathbf{Q},$$

and also due to the property $\mathbf{Q}\mathbf{Q} = \mathbf{I}$, the decoding matrix $\bar{\mathbf{M}}$ is defined as

$$\bar{\mathbf{M}} = \sum_{q=0}^{M-1} Y_q \big(\mathbf{I} - X_q \mathbf{Q}\big) = Y\mathbf{I} - \sum_{q=0}^{M-1} Y_q X_q \mathbf{Q}, \tag{3.25}$$

where

$$Y_q = \sum_{i=0}^{3} |h_{i,q}|^2, \quad X_q = \frac{2}{Y_q} \Re\{h_{0,q} h_{3,q}^* - h_{1,q} h_{2,q}^*\} \quad \text{and} \quad Y = \sum_{q=0}^{M-1} Y_q. \tag{3.26}$$

The signal term in (3.24) is evaluated as

$$\mathbf{M} \sum_{q=0}^{M-1} \bar{\mathbf{H}}_q^H \bar{\mathbf{H}}_q = \Big(Y\mathbf{I} - \sum_{q=0}^{M-1} Y_q X_q \mathbf{Q}\Big)\Big(Y\mathbf{I} + \sum_{q'=0}^{M-1} Y_{q'} X_{q'} \mathbf{Q}\Big) = \Big(Y^2 - \Big(\sum_{q=0}^{M-1} Y_q X_q\Big)^2\Big)\mathbf{I}, \tag{3.27}$$

and again, the absence of $\mathbf{Q}$ in (3.27) proves an interference-free result.

3.1.5 Orthogonal STLC

The OSTLC were the first STLC to be developed in [8]. They are based on the OSTBCs with linear decoding, such as the full rate Alamouti scheme [29], or the 3/4-rate, four-antenna OSTBC introduced in [31].

Transmitter

For the $M \times 2$ OSTLC, the transmit vector of the p-th TX antenna can be expressed as

$$\mathbf{v}_p = \alpha \bar{\mathbf{s}}^T \mathbf{h}_p^*, \tag{3.28}$$

where $\mathbf{v}_p = [v_{p,0} \ v_{p,1}]^T$, $\mathbf{h}_p = [h_{p,0} \ h_{p,1}]^T$, and where the TX power normalization coefficient is defined as

$$\alpha^{-1} = \sqrt{\sum_{p=0}^{N_T-1} |h_{p,0}|^2 + |h_{p,1}|^2}. \tag{3.29}$$

Receiver

The q-th RX antenna at time i receives a symbol defined as

$$r_{q,i} = \sum_{p=0}^{M-1} h_{p,q} v_{p,i} + w_{q,i}, \quad \forall \quad q, i \in \{0, 1\}, \tag{3.30}$$

where $w_{q,i}$ is the AWGN with variance $\sigma_w^2 = \mathrm{E}\{|w_{q,i}|^2\}$. The RX STLC decoding scheme is defined as

$$\tilde{s}_0 = \alpha\left(r_{0,0} + r_{1,1}^*\right), \quad \tilde{s}_1 = \alpha\left(r_{0,1} - r_{1,0}^*\right). \tag{3.31}$$

Note that the knowledge of α on the receiver is only required for non-PSK constellations.

3.1.6 Proposed FR-QSTLC

One of the first full-rate $M \times 4$ QSTLCs was proposed in our work [1]. In our newer publication, [2], the $M \times 4$ full-rate QSTLC was modified in order to improve the ABER performance. Both systems use the same receiver combining scheme, however, each has a different transmitter precoding scheme, which are analogous to the two RX combining methods of the QSTBC, shown in section 3.1.4. Therefore, the QSTLC from [1] will be denoted as "m1" and the one from as "m2" [2].

Transmitter - Method One

Using the QSTBC symbol matrix $\bar{\mathbf{s}}$ defined in (3.15), the STLC-precoded vector of symbols transmitted from the p-th TX antenna in times $i = \{0, 1, 2, 3\}$ is defined as (using notation similar to formula (1) in [10])

$$\mathbf{v}_p = \alpha \bar{\mathbf{M}}_p \bar{\mathbf{s}}^T \mathbf{h}_p^*, \tag{3.32}$$

where $\mathbf{v}_p = [v_{p,0} \ v_{p,1} \ v_{p,2} \ v_{p,3}]^T$, $\mathbf{h}_p = [h_{p,0} \ h_{p,1} \ h_{p,2} \ h_{p,3}]^T$. The TX normalization coefficient α is calculated to ensure that average sum of power from all M antennas equals $\sigma_s^2 = \mathrm{E}\{|s_i|^2\}$ and is calculated as

$$\alpha = \left(\sum_{p=0}^{M-1}(1 - X_p^2)Y_p\right)^{-1/2}, \tag{3.33}$$

where the auxiliary random variables Y_p and X_p are defined as

$$Y_p = \sum_{i=0}^{3}|h_{p,i}|^2 \quad \text{and} \quad X_p = \frac{2}{Y_p}\Re\{h_{p,0}h_{p,3}^* - h_{p,1}h_{p,2}^*\}. \tag{3.34}$$

The precoding matrix for the p-th TX antenna is given by $\bar{\mathbf{M}}_p = \mathbf{I} - X_p\mathbf{Q}$, where $\mathbf{I}$ represents 4×4 unit matrix and $\mathbf{Q}$ is defined in (3.20).

Transmitter - Method Two

The modified transmitter scheme in [2] also uses the QSTBC encoding matrix $\bar{\mathbf{s}}$ defined in (3.15), however, the STLC precoding is different from that in [1]. The

vector of symbols transmitted from the p-th TX antenna at times $i = \{0, 1, 2, 3\}$ is defined as

$$\mathbf{v}_p = \alpha \bar{\mathbf{M}} \bar{\mathbf{s}}^T \mathbf{h}_p^*, \tag{3.35}$$

where $\mathbf{v}_p$ and $\mathbf{h}_p$ definitions remain the same as in (3.32), and α is the TX power normalization coefficient given by

$$\alpha = \left((1 - X^2)Y\right)^{-1/2}. \tag{3.36}$$

Notice that $\bar{\mathbf{M}}$ is no longer dependent on p and it is defined as $\bar{\mathbf{M}} = \mathbf{I}_4 - X\mathbf{Q}$. In (3.35), $\mathbf{I}_4$ is a 4×4 unit matrix and $\mathbf{Q}$ is defined in (3.20). The auxiliary random variables Y and X are given as

$$Y = \sum_{p=0}^{M-1} \sum_{q=0}^{3} |h_{p,q}|^2, \quad X = \frac{2}{Y} \sum_{p=0}^{M-1} \Re\{h_{p,0}^* h_{p,3} - h_{p,1}^* h_{p,2}\}. \tag{3.37}$$

Receiver

The RX combining scheme is common for both [1] and [2]. The q-th RX antenna at time i receives a symbol defined as

$$r_{q,i} = \sum_{p=0}^{M-1} h_{p,q} v_{p,i} + w_{q,i}, \quad \forall \quad q, i \in \{0, 1, 2, 3\}, \tag{3.38}$$

where $w_{q,i} \sim \mathcal{CN}(0, \sigma_w^2)$ is the complex AWGN sample. The linear processing scheme is provided by summation and complex conjugation of the received symbols. Next, additional scaling provided by the positive real coefficient α is necessary only for m-QAM constellations. Finally, the symbol estimates are obtained by

$$\tilde{s}_0 = \alpha\left(r_{0,0} + r_{1,1}^* + r_{2,2}^* + r_{3,3}\right), \tag{3.39}$$

$$\tilde{s}_1 = \alpha\left(r_{0,1} - r_{1,0}^* + r_{2,3}^* - r_{3,2}\right), \tag{3.40}$$

$$\tilde{s}_2 = \alpha\left(r_{0,2} + r_{1,3}^* - r_{2,0}^* - r_{3,1}\right), \tag{3.41}$$

$$\tilde{s}_3 = \alpha\left(r_{0,3} - r_{1,2}^* - r_{2,1}^* + r_{3,0}\right). \tag{3.42}$$

3.2 Conditional SNR

Conditional SNR, denoted as Ξ, is considered a fundamental performance measure in communication systems. It is so especially because once we know the statistical distribution of Ξ, we are able to calculate most of the important average performance measures, including the ABER, avg. channel capacity, or outage probability [23]. In this section, I provide full derivations of the conditional SNR of the spatial-diversity systems defined in Section 3.1.

3.2.1 MRC and MRT

For the $1 \times M$ MRC and the $M \times 1$ MRT, defined in sections 3.1.1 and 3.1.2, the conditional SNR is defined identically, as

$$\Xi = \rho \sum_{i=0}^{M-1} |h_i|^2, \tag{3.43}$$

where $\rho = \sigma_s^2 / \sigma_w^2$ is the so-called TX SNR, introduced in Section 2.1.2.

3.2.2 Orthogonal STBC and STLC

The $2 \times M$ OSTBC system described in section 3.1.3 behaves identically to an $M \times 2$ OSTLC in section 3.1.5 and their relation has been thoroughly documented in [8]. For all $M \in \mathbb{N}$, their conditional RX SNR is given by

$$\Xi = \frac{\rho}{2} \sum_{i=0}^{M-1} \left(|h_{i,0}|^2 + |h_{i,1}|^2 \right). \tag{3.44}$$

3.2.3 Quasi-Orthogonal STBC - Method One

For the QSTBC with "m1" decoding, defined in section 3.1.4, the signal and noise variances are given by

$$P_S = \frac{\sigma_s^2}{4} \left(\sum_{q=0}^{M-1} Y_q^2 \left(1 - X_q^2 \right) \right)^2, \tag{3.45}$$

and

$$P_N = \sigma_w^2 \sum_{q=0}^{M-1} Y_q^3 \left(1 - X_q^2 \right), \tag{3.46}$$

respectively. The resulting conditional RX SNR of the first version is defined as

$$\Xi = \frac{\rho}{4} \frac{\left(\sum_{q=0}^{M-1} Y_q^2 \left(1 - X_q^2 \right) \right)^2}{\sum_{q'=0}^{M-1} Y_{q'}^3 \left(1 - X_{q'}^2 \right)}. \tag{3.47}$$

3.2.4 Quasi-Orthogonal STBC - Method Two

The "m2" decoding of the full rate QSTBC in section 3.1.4 has the conditional SNR defined by

$$\Xi = \frac{\rho}{4} Y (1 - X^2), \tag{3.48}$$

where

$$Y = \sum_{p=0}^{3} \sum_{q=0}^{M-1} |h_{p,q}|^2, \quad X = \frac{2}{Y} \sum_{q=0}^{M-1} \Re\{h_{0,q}^* h_{3,q} - h_{1,q}^* h_{2,q}\}. \tag{3.49}$$

3.2.5 Quasi-Orthogonal STLC - Method One

Our $M \times 4$ QSTLC, proposed in [1] and defined in 3.1.6 has Ξ evaluated as follows. By expanding the right side of (3.39) (e.g. for $\tilde{s}_0$) as

$$\tilde{s}_0 = s_0 + \alpha\left(w_{0,0} + w_{1,1}^* + w_{2,2}^* + w_{3,3}\right) = s_0 + \alpha\tilde{w}_0, \tag{3.50}$$

one obtains the RX noise power

$$P_N = \alpha^2 \, \mathrm{E}\left\{|\tilde{w}_0|^2\right\} = \frac{4\sigma_w^2}{\sum_{p=0}^{M-1}(1 - X_p^2)Y_p}, \tag{3.51}$$

where X_p and Y_p are defined in (3.34) as where the auxiliary random variables are defined as

$$Y_p = \sum_{i=0}^{3} |h_{p,i}|^2 \quad \text{and} \quad X_p = \frac{2}{Y_p}\Re\{h_{p,0}h_{p,3}^* - h_{p,1}h_{p,2}^*\}.$$

The signal power then equals $P_S = \mathrm{E}\{|s_0|^2\} = \sigma_s^2$ and the conditional RX SNR is defined as a ratio of P_S and P_N and it yields

$$\Xi = \frac{\rho}{4} \sum_{p=0}^{M-1}(1 - X_p^2)Y_p. \tag{3.52}$$

3.2.6 Quasi-Orthogonal STLC - Method Two

The conditional SNR of the second version of our QSTLC from [2] is derived similarly and yields

$$\Xi = \frac{\rho}{4}Y(1 - X^2), \tag{3.53}$$

where

$$Y = \sum_{q=0}^{3} \sum_{p=0}^{M-1} |h_{p,q}|^2, \quad X = \frac{2}{Y} \sum_{p=0}^{M-1} \Re\{h_{p,0}^* h_{p,3} - h_{p,1}^* h_{p,2}\}. \tag{3.54}$$

Note, that it matches the conditional SNR of the "m2"-decoded QSTBC in (3.49).

3.2.7 Full-rate STLC for 4 Antennas

The benchmark $M \times 4$ QSTLC defined in [17] has Ξ given by (formula (6) in [17])

$$\Xi = \frac{\rho}{4} \frac{\left(\sum_{p=0}^{M-1} Y_p(1 \pm X_p)\right)^2}{\sum_{p'=0}^{M-1} Y_{p'}}, \tag{3.55}$$

where

$$Y_p = \sum_{i=0}^{3} |h_{p,i}|^2 \quad \text{and} \quad X_p = \frac{2}{Y_p}\Re\{h_{p,0}h_{p,2}^* + h_{p,1}h_{p,3}^*\}. \tag{3.56}$$

3.3 Probability Density Function of the Conditional SNR

Once knowing the exact conditional SNR definition Ξ, it is possible for some distributions to derive the PDF, which can be used for analyzing the diversity gain and other important performance measures.

It should be pointed out that the Ξ in (3.53) is identical to formula (39) in [21] where authors express the PDF of Ξ for $M = 1$ using the Whittaker function. In this work, I apply a similar approach and derive the PDF for $M \in \mathbb{N}$. Such a PDF can later be used for the diversity gain analysis.

3.3.1 Gamma Distribution

Conditional SNR of the fundamental spatial diversity systems follows the scaled Chi-squared distribution (Gamma distribution) because it originates in a sum of independent squares of normal random variables. As an example, we could mention the MRT [27] or MRC [26] and also the STLC and STBC systems that are based on orthogonal designs [8]. PDF of the Gamma-distributed conditional SNR Ξ is defined as:

$$f_\Xi(\xi, \rho) = \frac{\xi^{nM-1}\, e^{-\frac{\xi m}{2\rho}}}{\left(2\rho/m\right)^{nM}\, \Gamma(nM)} \quad \forall \quad \xi \geq 0, \tag{3.57}$$

where $\Gamma(.)$ is the Gamma function and m and n are the scale and shape parameters, respectively. Gamma parameters of the systems used for comparison with the proposed design are summarized in Table 3.1.

Tab. 3.1: Gamma distribution PDF parameters

System	m	n
$M \times 1$ MRT, $1 \times M$ MRC	2	1
$M \times 2$ FR-OSTLC	4	2
Ideal $M \times 4$ (Lemma 1 in [17])	8	4

The quasi-orthogonal design, unlike the orthogonal one, no longer follows the Gamma distribution, although there has been an attempt to approximate the quasi-orthogonal design PDF with the Nakagami-m and Chi-squared distribution [33].

The following section provides an analytical PDF derivation of our QSTLC with "m2" precoding, published in [2].

3.3.2 QSTLC - Method Two

The conditional SNR has been defined in (3.53) as

$$\Xi = \frac{\rho}{4} Y (1 - X^2),$$

where Y and X were defined in (3.54) as

$$Y = \sum_{p=0}^{M-1} \sum_{q=0}^{3} |h_{p,q}|^2, \quad X = \frac{2}{Y} \sum_{p=0}^{M-1} \Re\{h_{p,0}^* h_{p,3} - h_{p,1}^* h_{p,2}\}.$$

The original idea leading to the precise PDF came from Appendix-A in [21], where it has been presented for $M = 1$. We extended it to $M \in \mathbb{N}$ in [2].

Random variable - Y

We begin by decomposing the complex channel gain $h_{p,q}$ into $a_{p,q} + jb_{p,q}$, where $a_{p,q}, b_{p,q} \sim \mathcal{N}(0, 1/2)$, so

$$Y = \sum_{p=0}^{M-1} \sum_{q=0}^{3} a_{p,q}^2 + b_{p,q}^2. \tag{3.58}$$

We can see that Y is Gamma distributed with a PDF defined by

$$f_Y(y) = \frac{y^{d-1} e^{-\frac{y}{a}}}{a^d \, \Gamma(d)} = \frac{y^{4M-1} e^{-y}}{\Gamma(4M)}, \quad \forall \quad y \geq 0, \tag{3.59}$$

where the $a = 1$ and $d = 4M$.

Random variable - X

The definition of X in (3.54) can be expanded into (using (3.58))

$$X = \frac{2 \sum_{p=0}^{M-1} a_{p,0} a_{p,3} + b_{p,0} b_{p,3} - a_{p,1} a_{p,2} - b_{p,1} b_{p,2}}{\sum_{p=0}^{M-1} a_{p,0}^2 + a_{p,1}^2 + a_{p,2}^2 + a_{p,3}^2 + b_{p,0}^2 + b_{p,1}^2 + b_{p,2}^2 + b_{p,3}^2},$$

and since it is more comfortable to work with $X + 1$, it can be expressed as

$$X + 1 = \frac{\sum_{p=0}^{M-1} \left(a_{p,0} + a_{p,3} \right)^2 + \left(b_{p,0} + b_{p,3} \right)^2 + \left(a_{p,1} - a_{p,2} \right)^2 + \left(b_{p,1} - b_{p,2} \right)^2}{\sum_{p=0}^{M-1} a_{p,0}^2 + a_{p,1}^2 + a_{p,2}^2 + a_{p,3}^2 + b_{p,0}^2 + b_{p,1}^2 + b_{p,2}^2 + b_{p,3}^2}.$$

Now we form a linear transformation (i.e., we define a new set of independent complex-normal distributed random variables)

$$u_p = (a_{p,0} + a_{p,3})/\sqrt{2} \qquad \bar{u}_p = (a_{p,0} - a_{p,3})/\sqrt{2},$$

$$v_p = (a_{p,1} - a_{p,2})/\sqrt{2} \qquad \bar{v}_p = (a_{p,1} + a_{p,2})/\sqrt{2},$$

$$y_p = (b_{p,0} + b_{p,3})/\sqrt{2} \qquad \bar{y}_p = (b_{p,0} - b_{p,3})/\sqrt{2},$$

$$z_p = (b_{p,1} - b_{p,2})/\sqrt{2} \qquad \bar{z}_p = (b_{p,1} + b_{p,2})/\sqrt{2}.$$

where all of them are $\sim \mathcal{N}(0, 1/2)$, and we use them in the $X + 1$ formula as

$$X + 1 = \frac{2\sum_{p=0}^{M-1} u_p^2 + y_p^2 + v_p^2 + z_p^2}{\sum_{p=0}^{M-1} u_p^2 + v_p^2 + y_p^2 + z_p^2 + \bar{u}_p^2 + \bar{v}_p^2 + \bar{y}_p^2 + \bar{z}_p^2}. \qquad (3.60)$$

After defining a new pair of RVs,

$$Z_1 = \sum_{p=0}^{M-1} u_p^2 + y_p^2 + v_p^2 + z_p^2, \qquad (3.61)$$

and

$$Z_2 = \sum_{p=0}^{M-1} \bar{u}_p^2 + \bar{v}_p^2 + \bar{y}_p^2 + \bar{z}_p^2, \qquad (3.62)$$

we may express $(X + 1)/2$ as

$$\check{X} = \frac{X+1}{2} = \frac{Z_1}{Z_1 + Z_2}, \qquad (3.63)$$

and because Z_1 and Z_2 are independent Gamma distributed RVs with $a = 1$ and $d = 2M$, $\check{X}$ is, by definition, **Beta distributed**, with PDF defined by

$$f_{\check{X}}(\check{x}) = \frac{\Gamma(a+b)}{c^a\,\Gamma(a)\Gamma(b)}\check{x}^{a-1}\,(1 - \check{x}/c)^{b-1}, \qquad (3.64)$$

and because $c = 1$, and $a = b = 2M$ we get

$$f_{\check{X}}(\check{x}) = \frac{\check{x}^{2M-1}\,(1-\check{x})^{2M-1}}{\mathrm{B}(2M, 2M)} = \frac{\check{x}^{2M-1}\,(1-\check{x})^{2M-1}\Gamma(4M)}{\Gamma^2(2M)}, \qquad (3.65)$$

where $\mathrm{B}(.,.)$ is the Beta function. In order to get $f_X(x)$ from $f_{\check{X}}(\check{x})$ we must perform the change of variable $\check{x} = (x+1)/2$, yielding

$$f_X(x) = \frac{(1-x^2)^{2M-1}\Gamma(4M)}{2^{4M-1}\Gamma^2(2M)}, \qquad \forall \quad |x| < 1. \qquad (3.66)$$

Statistical Independence of X and Y

Although we just derived the PDFs of Y and X, we must find out whether they are statistically independent or not. From (3.60) and (3.63) we see the relation of X, Y and Z_1, Z_2 as

$$Y = Z_1 + Z_2, \quad \text{and} \quad X = \frac{Z_1 - Z_2}{Z_1 + Z_2},$$

which may appear as if X was dependent on Y. This, however, is not the case. We may also express the formulae above as

$$Z_1 = \frac{1+X}{2}Y, \quad \text{and} \quad Z_2 = \frac{1-X}{2}Y. \qquad (3.67)$$

From the definitions of Z_1 and Z_2 in (3.61) and (3.62) we know, that they are statistically independent and identically distributed, with a PDF defined as

$$f_{Z_i}(z_i) = \frac{z_i^{2M-1} \, e^{-z_i}}{\Gamma(2M)} \quad \forall \quad z_i \geq 0. \tag{3.68}$$

Therefore, their joint-PDF is a product of their respective PDFs, defined as

$$f_{Z_1,Z_2}(z_1, z_2) = f_{Z_1}(z_1)f_{Z_2}(z_2) = \frac{(z_1 z_2)^{2M-1} \, e^{-z_1-z_2}}{\Gamma(2M)\Gamma(2M)} \quad \forall \quad z_1, z_2 \geq 0. \tag{3.69}$$

We now aim to obtain the joint PDF of X and Y by performing the **change of variables** in (3.69). First, we must calculate the Jacobian

$$J = \begin{vmatrix} \frac{\partial Z_1}{\partial X} & \frac{\partial Z_1}{\partial Y} \\ \frac{\partial Z_2}{\partial X} & \frac{\partial Z_2}{\partial Y} \end{vmatrix} = \begin{vmatrix} \frac{Y}{2} & \frac{1+X}{2} \\ -\frac{Y}{2} & \frac{1-X}{2} \end{vmatrix} = \left| \frac{Y}{2} \right| = \frac{Y}{2}, \tag{3.70}$$

after which we use the substitutions (3.67) along with the Jacobian (3.70) to obtain the joint PDF of X and Y as

$$f_{X,Y}(x,y) = \frac{((1-x)(1+x)y^2)^{2M-1} \, e^{-y}}{2^{4M-2} \, \Gamma(2M)\Gamma(2M)} \frac{y}{2} = \frac{(1-x^2)^{2M-1} \, y^{4M-1} \, e^{-y}}{2^{4M-1} \, \Gamma^2(2M)}. \tag{3.71}$$

We now see that $f_{X,Y}(x,y) = f_Y(y)f_X(x)$, which proves the statistical independence of X and Y. Fig. 3.1 compares the marginal PDFs to the simulations of all analyzed RVs (left) and it also provides a visual proof of statistical independence of X and Y (right), all for $M = 2$.
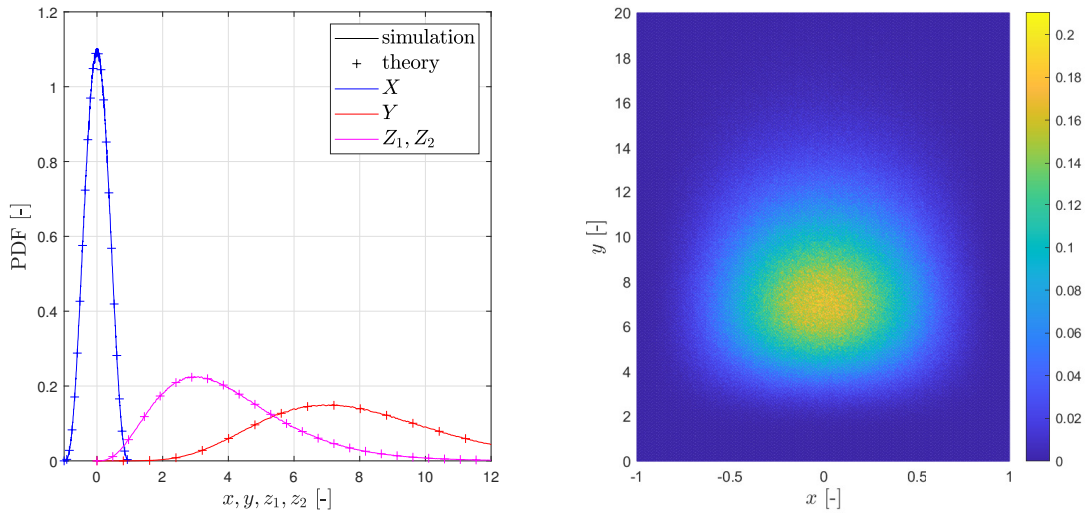

Fig. 3.1: Comparison of marginal PDFs (left) and the joint PDF (right) of X and Y for $M = 2$ and $\rho = 1$.

Joint PDF of the Conditional SNR

In order to obtain the PDF of Ξ in (3.53) we once again use the change of variables. Yet first, we must define another auxiliary random variable that is a function of X and Y, so that it can form a pair with Ξ. The definition of Ξ in (3.53) can be decomposed into

$$\Xi = \frac{\rho}{4} Y(1 - X^2) = \frac{\rho}{4}(1 - X)\frac{Y}{2}(1 + X) = \frac{\rho}{2}(1 - X)W,$$

and the following transformation can be defined

$$\Xi = \frac{\rho}{4} Y(1 - X^2), \quad W = \frac{Y}{2}(1 + X). \tag{3.72}$$

The reciprocial relation then yields

$$X = \frac{\rho W - 2\Xi}{\rho W} = \frac{W - 2\Xi/\rho}{W} \quad \text{and} \quad Y = \frac{\rho W^2}{\rho W - \Xi} = \frac{W^2}{W - \Xi/\rho}, \tag{3.73}$$

The Jacobian is evaluated as

$$J = \begin{vmatrix} \frac{\partial X}{\partial \Xi} & \frac{\partial X}{\partial W} \\ \frac{\partial Y}{\partial \Xi} & \frac{\partial Y}{\partial W} \end{vmatrix} = \begin{vmatrix} \frac{-2}{\rho W} & \frac{2Z}{\rho W^2} \\ \frac{\rho W^2}{(\rho W - \Xi)^2} & \frac{\rho W(\rho W - 2\Xi)}{(\rho W - \Xi)^2} \end{vmatrix} = \left| \frac{-2/\rho}{W - \Xi/\rho} \right|, \tag{3.74}$$

and because $Y \in \langle 0, \infty)$, consequently $W - \Xi/\rho \in (0, \infty)$ and the Jacobian equals

$$J = \frac{2/\rho}{W - \Xi/\rho}. \tag{3.75}$$

It is certain that $w \in (\xi/\rho, \infty)$ (since it is our auxiliary variable) and $\xi \in (0, \infty)$. After making the change of variables in (3.71) we obtain

$$f_{\Xi,W}(\xi, w) = \frac{1}{2^{4M-1}\Gamma^2(2M)} \left(1 - \frac{(w - 2\xi/\rho)^2}{w^2}\right)^{2M-1} \left(\frac{w^2}{w - \xi/\rho}\right)^{4M-1} e^{-\frac{w^2}{w - \xi/\rho}} J, \tag{3.76}$$

$$f_{\Xi,W}(\xi, w) = \frac{1}{2^{4M-1}\Gamma^2(2M)} \frac{2^{4M-1}}{\rho(w - \xi/\rho)} \left(\frac{\xi(w - \xi/\rho)}{\rho w^2}\right)^{2M-1} \left(\frac{w^2}{w - \xi/\rho}\right)^{4M-1} e^{-\frac{w^2}{w - \xi/\rho}},$$

$$f_{\Xi,W}(\xi, w) = \frac{1}{\rho^{2M}\Gamma^2(2M)} \frac{\xi^{2M-1}}{(w - \xi/\rho)} \left(\frac{w - \xi/\rho}{w^2}\right)^{2M-1} \left(\frac{w^2}{w - \xi/\rho}\right)^{2M-1} \left(\frac{w^2}{w - \xi/\rho}\right)^{2M} e^{-\frac{w^2}{w - \xi/\rho}},$$

and finally, the joint PDF of Ξ and W yields

$$f_{\Xi,W}(\xi, w) = \frac{\xi^{2M-1}}{\rho^{2M}\Gamma^2(2M)} \frac{w^{4M}}{(w - \xi/\rho)^{2M+1}} e^{-\frac{w^2}{w - \xi/\rho}}, \tag{3.77}$$

for $\xi \in \langle 0, \infty)$ and $w \in (\xi/\rho, \infty)$.

Marginal PDF of the Conditional SNR

Every joint PDF must fulfill the unity volume condition

$$1 = \int_0^\infty \int_{\xi/\rho}^\infty f_{\Xi,W}(\xi, w) \; dw \; d\xi,$$

which is expanded into

$$1 = \frac{1}{\rho^{2M}\Gamma(2M)} \int_0^\infty \xi^{2M-1} \frac{1}{\Gamma(2M)} \int_{\xi/\rho}^\infty \frac{w^{4M}}{\left(w - \xi/\rho\right)^{2M+1}} e^{-\frac{w^2}{w - \xi/\rho}} \; dw \; d\xi,$$

and into

$$1 = \frac{1}{\rho^{2M}\Gamma(2M)} \int_0^\infty \xi^{2M-1} f_C(\xi/\rho) \; d\xi, \tag{3.78}$$

where $f_C(\xi/\rho)$ is defined with substitution $y = \xi/\rho$ as

$$f_C(y) = \frac{1}{\Gamma(2M)} \int_y^\infty \frac{w^{4M}}{y^{2M+1}\left(w/y - 1\right)^{2M+1}} e^{-\frac{w^2}{y(w/y-1)}} \; dw.$$

We may also substitute $t = w/y$ to get

$$f_C(y) = \frac{y^{2M}}{\Gamma(2M)} \int_1^\infty \frac{t^{4M}}{\left(t - 1\right)^{2M+1}} e^{-y\frac{t^2}{(t-1)}} \; dt,$$

and another substitution, $v = t - 1$, yields

$$f_C(y) = \frac{y^{2M}e^{-2y}}{\Gamma(2M)} \int_0^\infty \frac{(v+1)^{4M}}{v^{2M+1}} e^{-y\left(v+\frac{1}{v}\right)} \; dv. \tag{3.79}$$

Now, if we expand $f_C(y)$ from (3.79) in (3.78), we obtain

$$1 = \frac{1}{\rho^{4M}\Gamma(2M)} \int_0^\infty \frac{\xi^{4M-1}e^{-2\frac{\xi}{\rho}}}{\Gamma(2M)} \int_0^\infty \frac{(v+1)^{4M}}{v^{2M+1}} e^{-\frac{\xi}{\rho}\left(v+\frac{1}{v}\right)} \; dv \; d\xi,$$

and after extracting the right side and removing the integral over ξ we obtain the marginal PDF of Ξ with parameter ρ (after replacing v with t again)

$$f_\Xi(\xi, \rho) = \frac{\left(\xi/\rho\right)^{4M-1}e^{-2\frac{\xi}{\rho}}}{\rho\Gamma^2(2M)} \int_0^\infty \frac{(t+1)^{4M}}{t^{2M+1}} e^{-\frac{\xi}{\rho}\left(t+\frac{1}{t}\right)} \; dt. \tag{3.80}$$

Since $(t+1)^{4M}t^{-2M-1}$ can be expressed in terms of a polynomial, we substitute $u = \xi/\rho$ and obtain

$$f_U(u, \rho) = \frac{u^{4M-1}e^{-2u}}{\rho\Gamma^2(2M)} \sum_{k=0}^{4M} \binom{4M}{k} \int_0^\infty t^{2M-1-k}e^{-u(t+\frac{1}{t})} \; dt, \tag{3.81}$$

where

$$\binom{n}{k} = \frac{n!}{k!(n-k)!}.$$

We now use formula 8.432-7 in [34], which is stated as

$$K_\nu(xz) = \frac{z^\nu}{2} \int_0^\infty \frac{1}{t^{\nu+1}} e^{-\frac{x}{2}\left(t+\frac{z^2}{t}\right)} dt, \quad \forall \quad |\arg z| < \frac{\pi}{4}, \tag{3.82}$$

where $K_\nu(.)$ is the modified Bessel function of the second kind. We also use identities 8.486-16

$$K_\nu(z) = K_{-\nu}(z), \tag{3.83}$$

and 8.486-10

$$zK_{\nu-1}(z) - zK_{\nu+1}(z) = -2\nu K_\nu(z), \tag{3.84}$$

which can be modified in a more comfortable form

$$K_{\nu+1}(2u) = \frac{\nu}{u} K_\nu(2u) + K_{\nu-1}(2u). \tag{3.85}$$

We now rewrite (3.82) into ($z = 1$, $u = x/2$)

$$2K_{\nu+1}(2u) = \int_0^\infty t^\nu e^{-u(t+\frac{1}{t})} dt, \tag{3.86}$$

and apply (3.86) to (3.81) which yields

$$f_U(u, \rho) = 2\frac{u^{4M-1} e^{-2u}}{\rho \Gamma^2(2M)} \sum_{k=0}^{4M} \binom{4M}{k} K_{2M-k}(2u). \tag{3.87}$$

After some more manipulations, we obtain the closed-form solution of the novel marginal PDF as stated in [2]

$$f_\Xi(\xi, \rho) = \frac{\xi^{4M-1} e^{-\frac{2\xi}{\rho}}}{\rho^{4M}} \sum_{\nu=0}^{2M} a_\nu K_\nu(2\xi/\rho), \quad \forall \quad \xi \in \langle 0, \infty \rangle, \tag{3.88}$$

where

$$a_\nu = \frac{2(1 + \mathrm{sgn}(\nu))}{\Gamma^2(2M)} \binom{4M}{2M + \nu} \quad \forall \quad \nu = \{0, 1, \ldots 2M\}, \tag{3.89}$$

and where sgn(.) is the signum function.

Fig. 3.2 displays the marginal PDFs (left) and joint PDF (right) of Ξ and W for $M = 2$. Formula (3.88) is graphically verified by comparison with simulation.

In Fig. 3.3 we can see the marginal PDF comparison of Ξ for all above-mentioned spatial diversity systems for $M = 4$. Also, the theoretical PDF in (3.88) has been verified by numerical simulations.

3.4 Average SNR

The conditional SNR of each spatial-diversity system is a random variable with a specific distribution. It makes sense to evaluate E$\{\Xi\}$ as it contributes to the overall
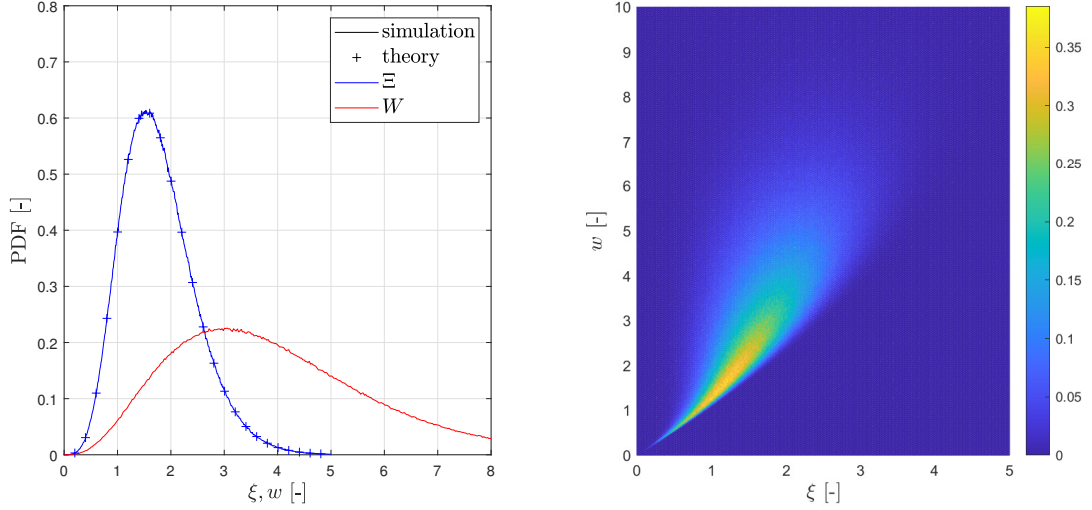
Fig. 3.2: Comparison of marginal PDFs (left) and the joint PDF (right) of Ξ and W for $M = 2$ and $\rho = 1$.

understanding of the system's behavior. The *Average Signal to Noise Ratio* (ASNR) is defined as

$$\bar{\xi}(\rho) = \mathrm{E}\{\Xi\} = \int_0^\infty \xi f_\Xi(\xi, \rho) \, d\xi, \tag{3.90}$$

where $f_\Xi(\xi, \rho)$ is the conditional RX SNR PDF at given ρ. Since ρ is always a scaling factor of ξ, formula (3.90) is simplified into

$$\bar{\xi}(\rho) = \rho \int_0^\infty \xi f_\Xi(\xi, 1) \, d\xi = \rho \bar{\xi}(1), \tag{3.91}$$

therefore, one only needs to calculate $\bar{\xi}(1)$ once for each design and the result is multiplied by ρ to obtain $\bar{\xi}(\rho)$. In case of the Gamma distribution (3.57), $\bar{\xi}(1)$ can be calculated analytically by using one of the Gamma function definitions

$$\int_0^\infty e^{-a\xi} \xi^{nM-1} \, d\xi = \frac{\Gamma(nM)}{a^{nM}}, \quad \forall \quad \mathcal{R}\{a\} > 0. \tag{3.92}$$

After using the Gamma distribution from (3.57), the definition in (3.90) is expanded into

$$\bar{\xi}(\rho) = \frac{(m/2)^{nM}}{\Gamma(nM)} \int_0^\infty \left(\xi/\rho\right)^{nM} e^{-\frac{\xi m}{\rho 2}} \, d\xi,$$

and after using (3.92), we obtain the final formula

$$\bar{\xi}(1) = \frac{2nM}{m}. \tag{3.93}$$

In case of the proposed QSTLC with PDF in (3.88), $\bar{\xi}(1)$ is given by (solution obtained from the MAPLE software)

$$\bar{\xi}(1) = \frac{4M^2}{4M + 1}. \tag{3.94}$$

45
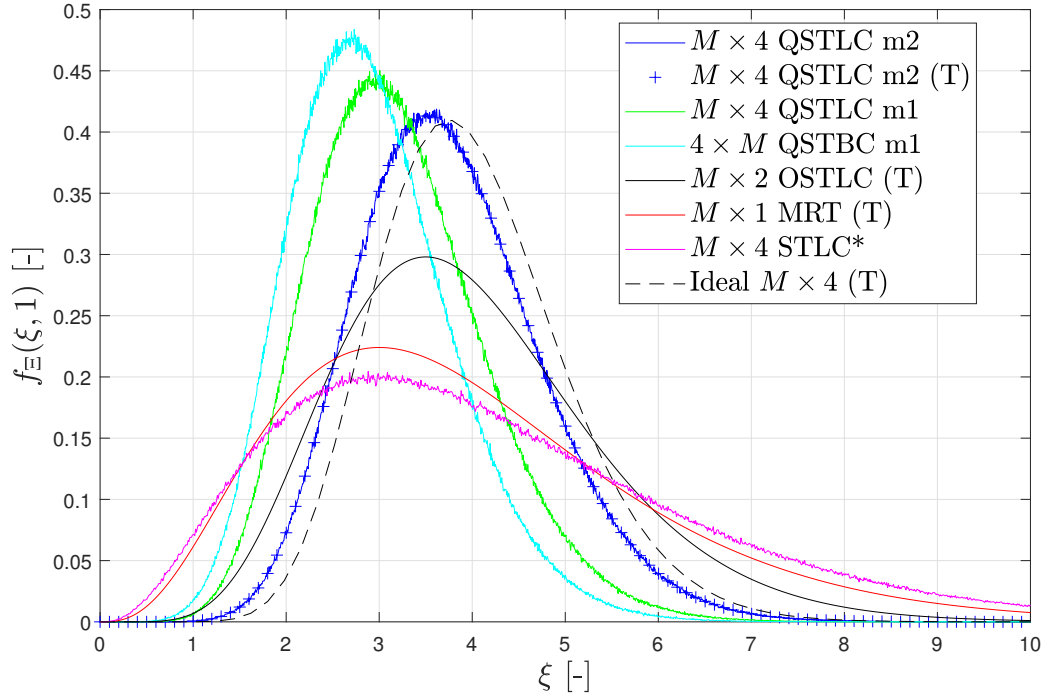
Fig. 3.3: PDF comparison for $M = 4$. The "m1" and "m2" represent method one and two, respectively, (T) represents theoretical results from (3.88) and (3.57) and * refers to [11].

Table 3.2 summarizes $\bar{\xi}(1)$ for all above mentioned systems. The symbol (N) appears for systems where ASNR was calculated numerically as $E\{\Xi\}$.

Tab. 3.2: ASNR Summary in the Linear Scale

System	$\bar{\xi}(1)$ @ $M = 2$	$\bar{\xi}(1)$ @ $M = 4$
$2M \times 1$ MRT (3.93)	4	8
$M \times 2$ OSTLC (3.93)	2	4
Ideal $M \times 4$ (3.93)	2	4
$4 \times M$ QSTBC m1 (N)	~ 1.5196	~ 2.912
$M \times 4$ STLC* (N)	~ 2.222	~ 4.235
$M \times 4$ QSTLC m1 (N)	1.6	3.2
$M \times 4$ QSTLC m2 (3.94)	$16/9 \cong 1.778$	$64/17 \cong 3.765$

3.5   Average Bit Error Ratio

The ABER is calculated from the conditional RX SNR as

$$\bar{\varepsilon}(\rho) = \int_0^\infty g(\rho u) \, f_U(u, 1) \, du, \tag{3.95}$$

where $g(x) = Q(\sqrt{x})$ for the 4-QAM constellation. For greater clarity of the analysis, the Gaussian Q-function will be replaced by its exponential approximation [35]

$$Q(\sqrt{x}) \cong \sum_{i=0}^{N-1} c_i e^{-d_i x}, \tag{3.96}$$

where $c_i, d_i \ \forall \ i \in \{0, 1, \dots N - 1\}$ are the optimized positive real coefficients also published in [35]. In case of the OSTLC with PDF in (3.57) (where $m = 4$, $n = 2$), the ABER is approximated by (using formula 3.351-3 in [34])

$$\bar{\varepsilon}(\rho) \cong \sum_{i=0}^{N-1} c_i \left(d_i \frac{\rho}{2} + 1 \right)^{-2M}. \tag{3.97}$$

The approximation of ABER of the proposed full rate QSTLC with PDF in (3.88) is given by ([34], 8.432-7)

$$\bar{\varepsilon}(\rho) \cong \sum_{i=0}^{N-1} c_i \sum_{\nu=0}^{2M} \tilde{a}_\nu \frac{F\left(4M + \nu, \nu + \frac{1}{2}; 4M + \frac{1}{2}; \frac{d_i \rho}{d_i \rho + 4}\right)}{(d_i \rho + 4)^{4M+\nu}}, \tag{3.98}$$

where $F(., .; .; .)$ is the Gaussian hypergeometric function and where

$$\tilde{a}_\nu = a_\nu 2^{2\nu + 8M - 1} \frac{\Gamma(4M)\Gamma(4M + \nu)\Gamma(4M - \nu)}{\Gamma(8M)}.$$

Note that a_ν is defined in (3.89).

3.6   Diversity Gain

The derivative of ABER w.r.t. the logarithm of ρ is defined as

$$\kappa(\rho) = -\frac{\partial \log_{10}(\bar{\varepsilon}(\rho))}{\partial \log_{10}(\rho)}, \tag{3.99}$$

and it asymptotically reaches the diversity gain defined by

$$\mathcal{D} = -\lim_{\rho \to \infty} \frac{\partial \log_{10}(\bar{\varepsilon}(\rho))}{\partial \log_{10}(\rho)} = -\lim_{\rho \to \infty} \frac{\rho}{\bar{\varepsilon}(\rho)} \frac{\partial \bar{\varepsilon}(\rho)}{\partial \rho}, \tag{3.100}$$

which is evaluated in decades of ABER per $10\,\mathrm{dB}$ of ρ (i.e., E_b/N_0) [36].

The diversity gain of OSTLCs can be derived directly from (3.97), and it equals $2M$ for $M \in \mathbb{N}$ [8]. The diversity gain of the proposed QSTLC with "m2" precoding is derived in the remainder of this section.

Lemma 1: The diversity gain in (3.100) equals $2M$ for $M \in \mathbb{N}$ for the case when $g(x)$ in the ABER definition (3.95) is substituted with $c\exp(-dx)$ where $c, d > 0$, independent of the choice of c, d.

Proof. Formula (3.100) may be expanded into $\mathcal{D} = -L_A L_B$, where

$$L_A = \lim_{\rho \to \infty} \frac{\rho}{\bar{\varepsilon}(\rho)}, \text{ and } L_B = \lim_{\rho \to \infty} \frac{\partial \bar{\varepsilon}(\rho)}{\partial \rho}. \tag{3.101}$$

Those are evaluated separately by using formula (3.98) (where $N = 1$, $c_i = c$ and $d_i = d$) for $\bar{\varepsilon}(\rho)$. The limit of $\bar{\varepsilon}(\rho)$ is evaluated by using Theorem 2.1.3 in [37] as

$$\lim_{\rho \to \infty} \bar{\varepsilon}(\rho) = \frac{2c}{d^{2M}} \lim_{\rho \to \infty} \rho^{-2M}, \tag{3.102}$$

therefore, the L_A yields

$$L_A = \frac{d^{2M}}{2c} \lim_{\rho \to \infty} \rho^{2M+1}. \tag{3.103}$$

Secondly, the L_B is elaborated as

$$L_B = \lim_{\rho \to \infty} c \sum_{\nu=0}^{2M} \tilde{a}_\nu \frac{d(4M+\nu)}{(d\rho+4)^{4M+\nu+1}} \left(\frac{4(2\nu+1)}{(8M+1)(d\rho+4)} \right.$$

$$\times F\left(4M+\nu+1, \nu+\frac{3}{2}; 4M+\frac{3}{2}; \frac{d\rho}{d\rho+4}\right)$$

$$\left. -F\left(4M+\nu, \nu+\frac{1}{2}; 4M+\frac{1}{2}; \frac{d\rho}{d\rho+4}\right) \right), \tag{3.104}$$

and after using Theorem 2.1.3 in [37] it yields

$$L_B = -4M \frac{c}{d^{2M}} \lim_{\rho \to \infty} \rho^{-2M-1}. \tag{3.105}$$

The product $-L_A L_B$ then equals $2M$. $\qquad\square$

Due to the result of *Lemma 1* and given the fact that $c\exp(-dx)$ may represent either the upper or the lower bound of $Q(\sqrt{x})$, we present the following theorem.

Theorem 1: The diversity gain of the proposed $M \times 4$ FR-QSTLC system equals $2M$ for $M \in \mathbb{N}$.

3.7 Asymptotic SNR Gain

In *Theorem 1*, we prove that our $M \times 4$ full rate QSTLC, proposed in [2], has the same diversity gain as the $M \times 2$ full rate OSTLC in [8], i.e., $2M$. Despite this fact, the proposed system achieves an additional asymptotic SNR gain due to the momentary overshoot of $\kappa(\rho)$ visible in Fig. 3.7. The ABER, displayed in log-log axes, asymptotically approaches a straight line defined by

$$\log_{10}\left(\tilde{\bar{\varepsilon}}(\rho)\right) = -2M\log_{10}(\rho) + \log_{10}\left(\tilde{\bar{\varepsilon}}_1\right), \tag{3.106}$$

where $\tilde{\bar{\varepsilon}}(\rho)$ is the asymptotic line approximation of $\bar{\varepsilon}(\rho)$, obeying

$$\lim_{\rho\to\infty} \frac{\log_{10}\left(\bar{\varepsilon}(\rho)\right)}{\log_{10}\left(\tilde{\bar{\varepsilon}}(\rho)\right)} = 1, \tag{3.107}$$

and where $\tilde{\bar{\varepsilon}}_1 = \tilde{\bar{\varepsilon}}(1)$. We obtain the SNR offset in dB for both full rate OSTLC and full rate QSTLC as

$$t[dB] = \frac{10}{2M}\log_{10}\left(\tilde{\bar{\varepsilon}}(1)\right), \tag{3.108}$$

and the asymptotic SNR gain is defined as the difference between the offsets.

3.7.1 Asymptotic SNR Offset of the Proposed FR-QSTLC

The limit of the logarithm of $\bar{\varepsilon}(\rho)$ defined in (3.98) is given by

$$\lim_{\rho\to\infty}\log_{10}\left(\bar{\varepsilon}(\rho)\right) \cong \lim_{\rho\to\infty}\log_{10}\left(a_0\Gamma(4M)\sum_{i=0}^{N-1}c_i\frac{\ln\left(d_i\rho+4\right)}{(d_i\rho+4)^{4M}}\right.$$

$$\left.+\sum_{i=0}^{N-1}c_i\sum_{\nu=1}^{2M}\frac{a_\nu}{2}\frac{\Gamma(\nu)\Gamma(4M-\nu)}{(d_i\rho+4)^{4M-\nu}}\right), \tag{3.109}$$

and its line approximation is found by its mere simplification into

$$\lim_{\rho\to\infty}\log_{10}\left(\tilde{\bar{\varepsilon}}(\rho)\right) = -2M\lim_{\rho\to\infty}\log_{10}\left(\rho\right) + \log_{10}\left(2\sum_{i=0}^{N-1}\frac{c_i}{d_i^{2M}}\right). \tag{3.110}$$

The SNR offset of the proposed system then yields

$$t_Q[dB] = \frac{5}{M}\log_{10}(2) + \frac{5}{M}\log_{10}\left(\sum_{i=0}^{N-1}\frac{c_i}{d_i^{2M}}\right). \tag{3.111}$$

3.7.2 Asymptotic SNR Offset of the FR-OSTLC

Formula (3.97) defines the approximated ABER of full rate OSTLC. The asymptotic line approximation can be evaluated as

$$\lim_{t\to\infty}\log_{10}\left(\tilde{\bar{\varepsilon}}(\rho)\right) = -2M\lim_{\rho\to\infty}\log_{10}\left(\rho\right) + \log_{10}\left(\sum_{i=0}^{N-1}\frac{c_i 2^{2M}}{d_i^{2M}}\right), \tag{3.112}$$
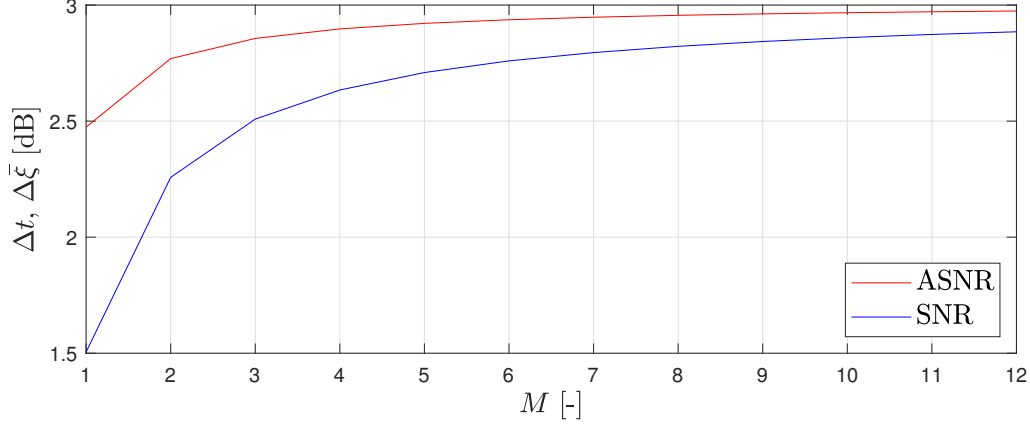
Fig. 3.4: SNR (3.114) and ASNR (3.115) asymptotic gain comparison for different M.

from which the asymptotic SNR offset can be readily defined as

$$t_O[dB] = 10 \log_{10}\left(2\right) + \frac{5}{M} \log_{10}\left(\sum_{i=0}^{N-1} \frac{c_i}{d_i^{2M}}\right). \tag{3.113}$$

3.7.3 Asymptotic SNR Gain

By subtracting (3.111) from (3.113) we obtain the precise asymptotic SNR gain (notice that the approximation term containing dataset coefficients c_i, d_i cancels-out)

$$\Delta t[dB] = t_O[dB] - t_Q[dB] = \left(10 - \frac{5}{M}\right) \log_{10}(2), \tag{3.114}$$

which ascends quickly to 3 dB as M increases.

3.7.4 Asymptotic ASNR Gain

The asymptotic gain may be evaluated also as a difference of ASNR. After involving (3.93) and (3.94), we may modify the asymptotic SNR gain (3.114) to

$$\Delta \bar{\xi}[dB] = \left(-10 - \frac{5}{M}\right) \log_{10}(2) + 10 \log_{10}\left(4 + \frac{1}{M}\right). \tag{3.115}$$

Fig. 3.4 shows how fast each of the asymptotic gains rises if plotted over M.

3.8 Performance Analysis

3.8.1 Asymptotic SNR Gain

Fig. 3.5 shows the comparison of the $M \times 2$ FR-OSTLC and the proposed $M \times 4$ FR-QSTLC, where $M = \{2, 4, 8\}$, for Gray-coded 4QAM constellation as ABER
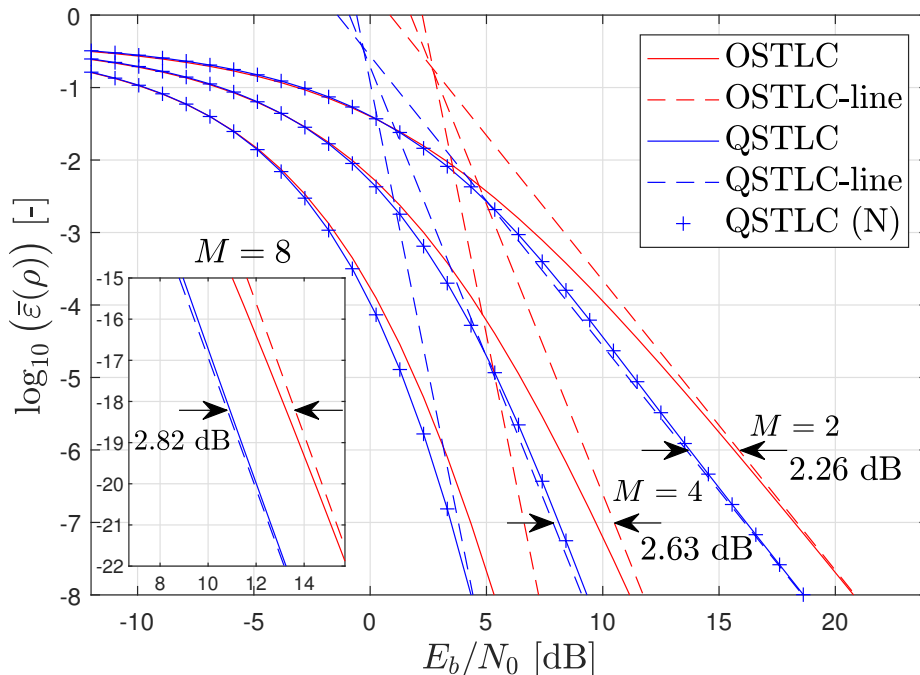
Fig. 3.5: ABER calculated using (3.97) (OSTLC) and (3.98) (QSTLC "m2") with asymptotic line approximations defined in (3.106) and the numerical model (N) for $M = \{2, 4, 8\}$.

versus E_b/N_0. It contains the ABER definitions (3.97) and (3.98), the straight line approximation (3.106) and the numerical simulation result obtained at 10^9 random channel realizations. We considered 100 4QAM symbols per channel realization. The numerical results are missing for ABER regions below 10^{-8} due to the enormous computational time requirements. Nevertheless, formula (3.98) perfectly matches the numerical results. It is due to the local overshoot of $\kappa(\rho) = 2M$ (visible in Fig. 3.7) that the proposed system achieves certain SNR gain (or identically, E_b/N_0 gain) that rises with M and equals $\Delta t = \{2.26, 2.63, 2.82\}$ dB for $M = \{2, 4, 8\}$, respectively, according to formula (3.114).

3.8.2 State-of-the-Art Comparison

This section focuses on the comparison of the full rate QSTLC in [2] with other benchmarked STLCs. Such a comparison is made for the Gray-coded 4QAM constellation via ABER (3.95) and its derivative (3.99) in relation to E_b/N_0. Note that since all the presented systems have a code rate equal to one, E_b/N_0 is related to ρ by $E_b/N_0[dB] = \rho[dB] - 10\log_{10}(2)$.

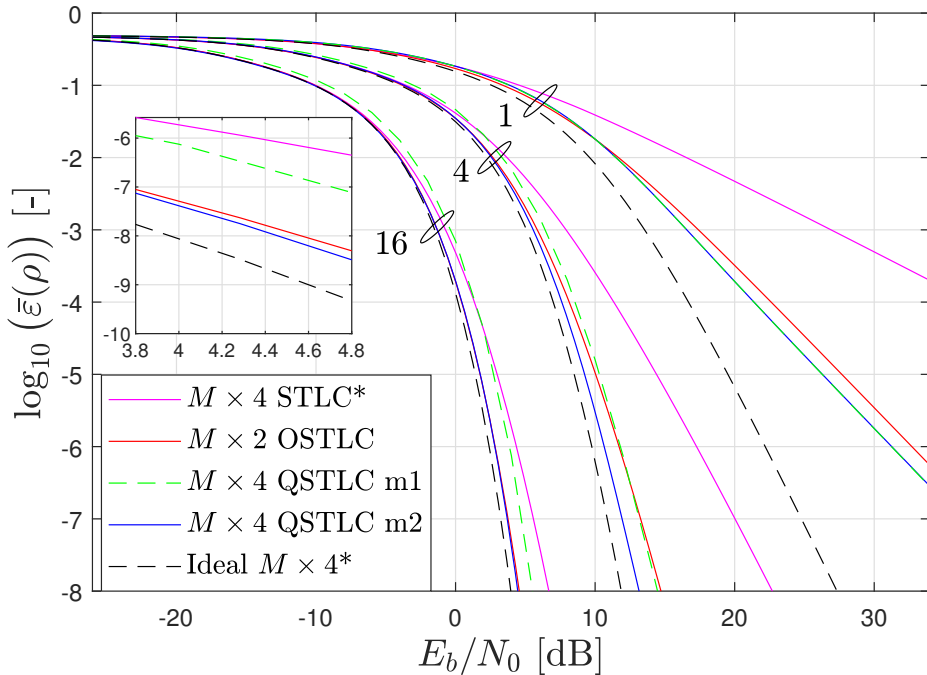Fig. 3.6 shows the ABER comparison of some of the above-mentioned systems

Fig. 3.6: ABER calculated using (3.97) (OSTLC) and (3.98) (QSTLC "m2") for $M = \{1, 4, 16\}$ with a detailed view of $M = 16$. The * symbol refers to [17].

for $M = \{1, 4, 16\}$. It is visible that the proposed "m2" $M \times 4$ QSTLC is located closest to the ideal $M \times 4$ OSTLC for all values of M. The $M \times 2$ OSTLC system is located behind the proposed one, followed by the design presented in [1], and lastly, by the system published in [17]. The derivative of ABER normalized to M for $M = \{1, 4, 16\}$ is plotted in Fig. 3.7. From the way M influences $\kappa(\rho)$ we can conclude that the diversity gain of the proposed $M \times 4$ QSTLC indeed equals to $2M$.

Fig. 3.8 provides an ABER comparison for all of the discussed systems. Above, ABER is plotted relative to the E_b/N_0, and below it is plotted relative to the ASNR. When ABER is related to ASNR the respective curves align along the x-axis, so that it appears as if all of them originated in a single curve at the low ASNR region. For the $2M \times 1$ MRT and $M \times 2$ OSTLC this literally is the case, since they unify for all values of ASNR.

Regardless of the x-axis, the "m2" QSTLC is still the best performing $M \times 4$ system as it is closest to the ideal $M \times 4$ system. The only exception is the $2M \times 1$ MRT in the upper part of Fig. 3.8, which outperforms the ideal $M \times 4$ in ABER (not in diversity gain) in low E_b/N_0 regions due to its high SNR gain, which disappears if ABER is displayed against ASNR (lower part of the figure).
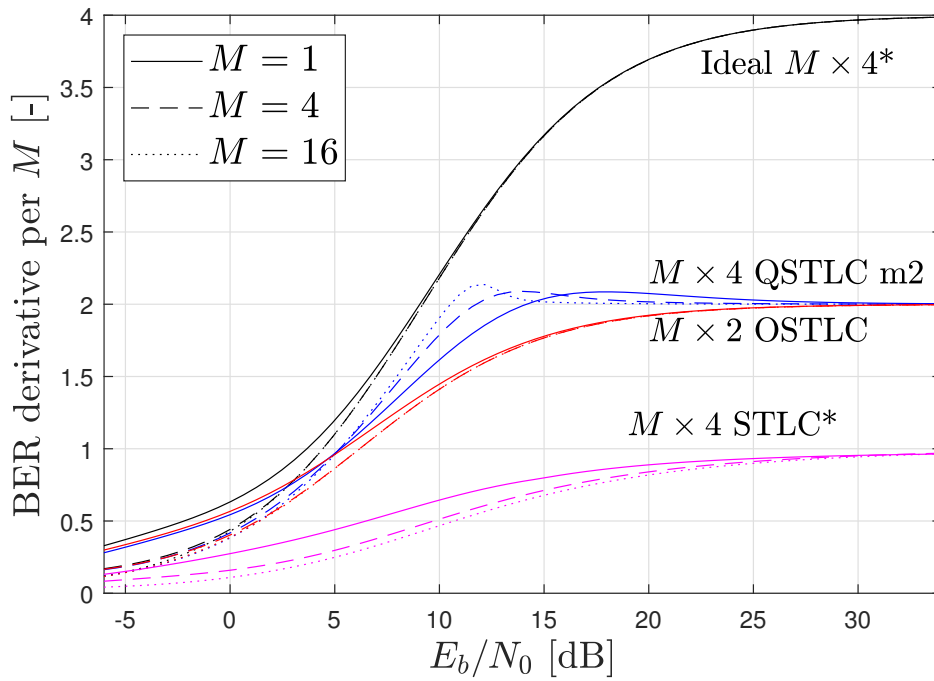
Fig. 3.7: Normalized derivative of ABER calculated using (3.99) combined with (3.97) (OSTLC) and (3.98) (QSTLC "m2") for $M = \{1, 4, 16\}$. The * symbol refers to [17].
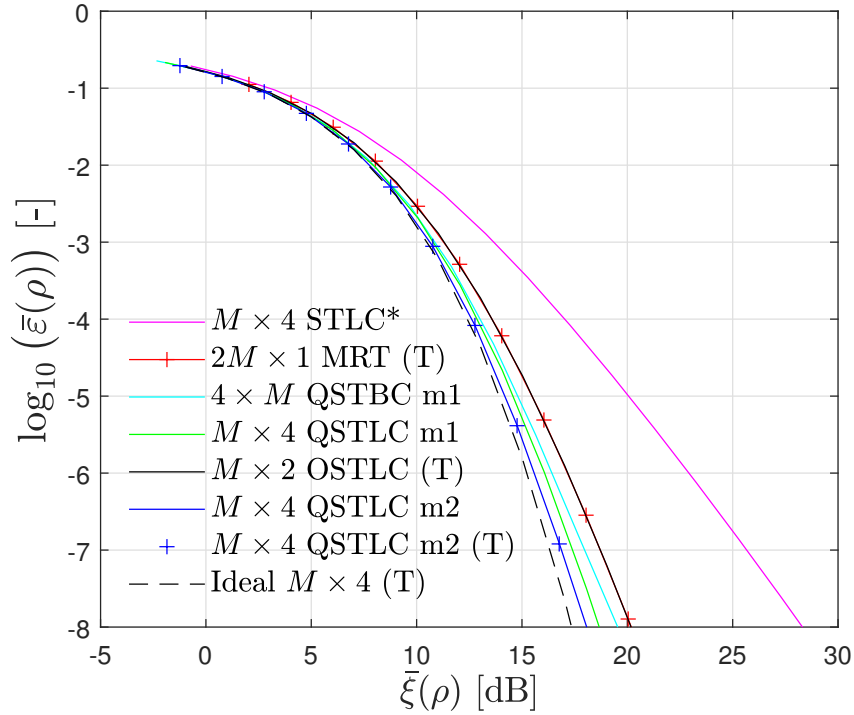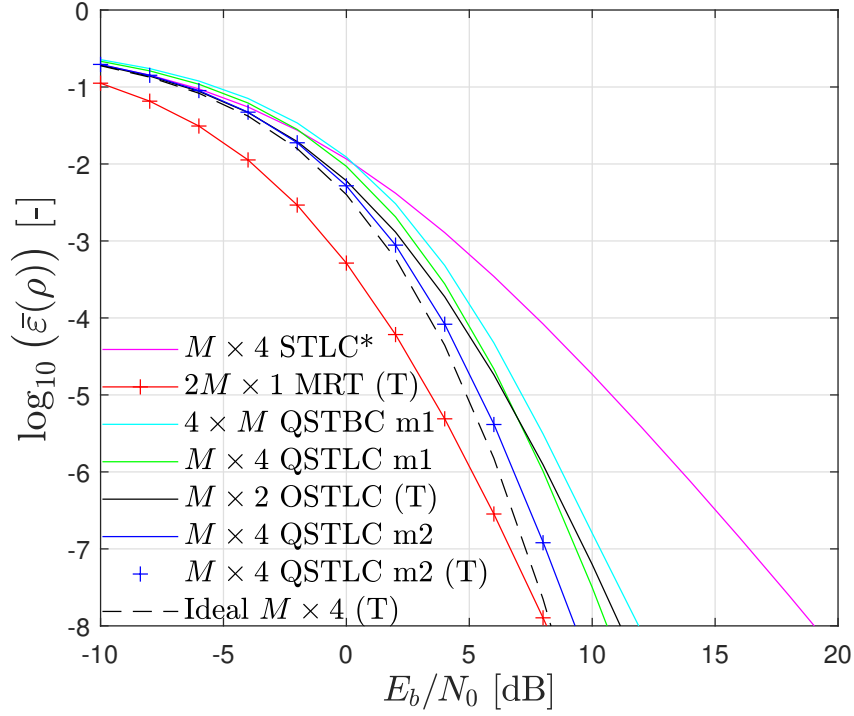
Fig. 3.8: ABER vs E_b/N_0 (top) and ABER vs ASNR (bottom) comparison for $M = 4$. (T) represents theoretical results from (3.97) and (3.98), and $*$ refers to [17].

Conclusions to the First Part

In the first part of the thesis, I introduced the fundamental spatial-diversity MIMO techniques and presented an original contribution of a full-rate quasi-orthogonal STLC for an arbitrary number of transmit antennas M and four receiver antennas.

All techniques were analyzed via the conditional receiver SNR, which is a channel-dependent random variable containing all information about the given spatial diversity technique in a flat-fading Rayleigh channel. This way a thorough and fair comparison can be made. For a proper analysis of the diversity gain it is essential to obtain the precise analytical PDF expression of the conditional SNR. In the early STBC years it was popular to approximate the system's PDF with an existing distribution, such as the Nakagami-m distribution, which lead to incorrect claims about the diversity gain, especially for $M \to \infty$. This thesis highlights the absolute necessity of having a precise PDF formula (for a given M) before attempting to draw conclusions about any performance measure, especially when it is an asymptotically defined quantity, such as the diversity gain. In other words, if the diversity gain is analyzed for $M \to \infty$, care must be taken before drawing any conclusions for the case where $M \in \mathbb{N}$.

Evaluating the diversity gain was trivial for the fundamental spatial-diversity systems as their PDF matches the Gamma distribution, for which there are straightforward solutions readily available in literature. However, the proposed system's PDF could not be described by any known statistical distribution, therefore, a novel distribution, based on a weighted sum of second-kind Bessel functions, was derived in (3.88) and it was shown in Fig 3.2 that it precisely matches the numerical simulations for all $M \in \mathbb{N}$.

After obtaining a precise PDF, the diversity gain was evaluated as equal to $2M$, which is the same as for the $M \times 2$ OSTLC. Nevertheless, the proposed $M \times 4$ QSTLC exhibits an asymptotic SNR (E_b/N_0) gain compared to $M \times 2$ OSTLC, rising quickly towards 3dB even for small M. This gain represents a certain motivation for having four RX antennas instead of just two. Interestingly enough, the asymptotic gain rises with M even faster if calculated from ASNR instead of SNR (see Fig. 3.4). Even though the standard metric in a majority of STBC and STLC literature remains the SNR (E_b/N_0), in my opinion, it is worth thinking about the importance of ASNR since unlike the SNR, it accounts for the channel statistics.

Part II

Unique Word Orthogonal Time Frequency Space

4 State-of-the-Art

4.1 OTFS

Wireless communication in channels with high selectivity in both the time and frequency domains is a hot research topic. One of the most popular waveforms for vehicular-to-everything (V2X) communications is the OTFS modulation [38]. If compared with the OFDM, OTFS is designed to cope with the doubly-dispersive channel effects by introducing an additional precoding known as the *Symplectic Fourier Transform* (SFT). The input m-QAM data symbols are spread across the frequency and time domain, which in the case of ideal TX/RX pulse shaping allows to achieve full diversity [39].

Just like in OFDM, it can be beneficial to use the *Cyclic Prefix* (CP) in OTFS. Even though most of the OTFS literature focuses on a single CP or no CP approach [40–48], there are numerous publications on the multiple-CP OTFS design [49–53].

The OTFS with a single CP benefits from high spectral efficiency (low redundancy), however, its receiver complexity becomes a major issue for large $M \times N$ *Delay-Doppler* (DD) matrices due to the need for $MN \times MN$ matrix inversion [46]. One possible workaround is the message passing algorithm, that exploits the channel sparsity for a reduced complexity of the data detection [41, 54]. Another way to prevent this is to use the CP in front of each OTFS symbol, which only requires N inversions of each $M \times M$ matrix [44, 49], and the complexity can be further reduced by using the *Lower-Upper* (LU) decomposition [46]. This multiple CP approach is often denoted as the OFDM-based OTFS [44, 49, 50, 55] because the standard OFDM modulator is used as the outer block.

The OTFS literature is vast and it mostly focuses on analysis in the continuous time domain [41–43]. This is preferred even among the OFDM-based OTFS publications [44, 55] and an absolute majority of publications leave out the important aspect of every OFDM modulator - the guard band located in the frequency domain. The major role of the guard band is to shape the TX waveform's spectrum and therefore, relax the otherwise strict design requirements on the TX and RX filters. Based on our best knowledge, there has been only one study published on OTFS with the guard band implemented in the frequency domain [56].

4.2 Unique Word OFDM

The term *Guard Interval* (GI) is often used to represent either the CP or some deterministic UW in the OFDM literature. The use of a UW instead of the CP has been first introduced in the single-carrier systems, in order to replace the random

redundancy of CP by a deterministic UW that could be used for *Channel Estimation* (CE) and possibly also assist in synchronization [57–59]. Since the primary use of the GI was to enable a block-wise RX processing (i.e., ISI mitigation), from this point of view it is irrelevant as to which type of the GI (i.e., a CP, zero guard or a UW sequence) is used. The particular type of GI becomes important when other performance measures are evaluated, such as PAPR, spectral *Out-of-Band* (OOB) emissions, spectral efficiency, CE performance and synchronization.

In [60], the UW was first adopted as a GI for the OFDM, thus *Unique-Word Orthogonal Frequency Division Multiplexing* (UW-OFDM) was born. The paper presents a method of generating a zero GI of length N_u on the *inverse Discrete Fourier Transform* (IDFT) output by adding a set of N_r redundant subcarriers to the data in the frequency domain. The pre-calculated matrix $\bar{\mathbf{G}}$ is responsible for inserting the redundant subcarriers, and consequently, for generating the GI in the time domain. However, the RX complexity of UW-OFDM is higher than that of the CP-OFDM, because the equivalent channel matrix in the *Frequency Domain* (FD) is not diagonal for UW-OFDM, due to the addition of redundant subcarriers on the TX side. The design in [60] clearly demonstrates how non-trivial the GI (UW) insertion is in OFDM compared to, e.g., UW SC-FDE [60, 61]. However, in [60] the reason why UW-OFDM has an improved BER against the CP-OFDM was not yet known.

Later, in [62], the data estimators based on classical and Bayesian approach were developed for UW-OFDM and their BER performance as well as their processing complexity were analyzed. The results revealed that the *Zero Forcing* (ZF) estimator offers the lowest complexity and good BER performance in the AWGN channel. The *Best Linear Unbiased Estimator* (BLUE), and especially the *Linear Minimum Mean Square Error* (LMMSE) estimator outperform the ZF in BER in the frequency-selective channels at the cost of higher RX complexity.

The idea of introducing redundant subcarriers that are systematically distributed among the data subcarriers [60] was later generalized to a non-systematic approach [63], where the redundant subcarriers were merged with the data subcarriers.

In [64] a new study on the redundant subcarrier optimization in UW-OTFS was published. The redundant energy is minimized and a more efficient algorithm for the optimization is proposed.

4.3   Unique Word OTFS - Scientific Contribution

In [7], we introduce a new OTFS design, which we call the UW-OTFS. This system belongs to the group of OFDM-based OTFS, however, here the UW-OFDM in

[62, 63] is used as the OFDM modulator. UW-OTFS, similarly to other OFDM-based OTFS designs, takes advantage of the reduced RX processing complexity (i.e., no *Inter-Block-Interference* (IBI)) due to the presence of a GI. In UW-OTFS (and also in UW-OFDM), GI is a part of each OTFS symbol, rather than being concatenated to it. More so, UW-OTFS is fully vectorized (i.e., designed in discrete time domain) and a guard band is an inherent part of its design (as it is for the UW-OFDM [62,63]). The non-systematic precoding, adopted from UW-OFDM [63], brings several benefits to the UW-OTFS:

- it is responsible for generating the GI in the *Time Domain* (TD)
- it adds redundancy to the data, which is equivalent to the Reed-Solomon encoding in the complex domain, effectively improving BER [63]
- along with the guard band it greatly improves the OOB emissions compared to conventional OFDM modulators with CP [63].

UW-OTFS comes with its own unique method of CE and UW sequence design. Instead of embedding the pilot among data in the DD domain [42, 44, 45, 65], UW-OTFS utilizes an idea where the UW sequence is superimposed to the *Fast Fourier Transform* (FFT) block, as it is shown in Fig. 6.1. The UW sequence is specifically designed to meet the following criteria:

1. CE quality
2. low data interference
3. *Power Spectral Density* (PSD) and its OOB emissions

The first criterion is evaluated in our work by the *Normalized Mean Square Error* (NMSE) simulations.

As for the second criterion, in conventional OTFS with the embedded pilot CE method, the received waveform must pass through the RX processing chain prior to obtaining the channel estimate, which increases the complexity [44,45,65]. Moreover, if a guard band was used in such a design, the fractional sampling ratio between the delay and time domain would cause the channel estimate to spread across the delay domain and interfere with data (see Section A.5 for a detailed explanation). In UW-OTFS, this problem is avoided by making the GI length M_{gi} twice the channel memory $M_{\tilde{\tau}}$, i.e., $M_{gi} \geq 2M_{\tilde{\tau}}$, and by focusing the most of the UW energy into the GI. The CE method then uses only the last $M_{gi}/2$ samples of the received waveform (i.e., the latter half of the GI), which do not interfere with the data waveform. As it is shown in Section 6.8, the increased redundancy due to this countermeasure is comparable to that of the conventional OTFS with CP and the embedded pilot.

The third criterion is split into another three sub-criteria:

a) The UW sequence overlaps the data part of the OTFS symbol. This provides more degrees of freedom for the UW sequence design.
b) The UW sequence is not periodic with a period of M' samples. This eliminates

the spectral spikes that would otherwise emerge due to periodicity.

    c) The UW sequence is designed to not increase the OOB emissions.

It is also shown in Section 6.8 that UW-OTFS has a similar PAPR and much lower OOB emissions than the conventional OTFS with the embedded pilot.

The contribution of the second part of the thesis is summarized as follows:

- A new type of the OFDM-based OTFS with a guard band is developed, using the UW-OFDM modulator.
- an example UW sequence is designed that shows excellent PSD properties and sufficient CE quality.
- the BER, *Mean Square Error* (MSE) and NMSE performances are analyzed in the *Linear-Time-Variant* (LTV) fractional Doppler channel.
- the spectral efficiency, transmitter complexity, and PAPR of the proposed UW-OTFS are compared to the conventional OTFS with the guard band, CP and the embedded pilot.

4.4 Basis Expansion Model in OTFS

The UW-OTFS CE method, introduced in Section 6.4, happens to be variant of the *Generalized Complex-Exponential Basis Extension Model* (GCE-BEM), which was one of *Basis Expansion Model* (BEM) types, popular CE methods in a high-mobility OFDM research [66, 67].

The first appearance of the BEM in the OTFS context was in [68], where the *Complex-Exponential Basis Extension Model* (CE-BEM) was implemented to replace the LTV channel model in order to reduce the number of CSI coefficients to be estimated. Until this day, several BEM-related OTFS publications have emerged [69] [70] [71] [72] [73] [74], all varying in types of the BEM basis vectors and pilot techniques. However, all of the references use positive integer values of the BEM resolution factor, which is equivalent to the *Doppler Scaling Factor* (DSF) used in our UW-OTFS, discussed in detail in Section 6.7. Please note, that our contribution in [7] is based on having positive-real values of the DSF, which justifies the novelty of our approach.

4.5 Related Research

The OTFS literature also includes publications where the low-PAPR *Zadoff-Chu* (ZC) sequences are used for CE in a doubly-dispersive channel. In [75], the waveform similar to OTFS is designed with UW sequences at the beginning and the end of the transmission, each protected by an attached CP. However, it is also admitted

in [75] that the ZC UW is not optimal for time-variant channels and its size must be reduced to minimize the distortion. The Doppler resolution of this method is also limited due to having only two UWs per transmission (for comparison, UW-OTFS utilizes N samples of the LTV channel per transmission, therefore offering a much finer Doppler resolution).

In [76] the waveform from [75] is adopted into the MIMO topology. In [77] a universal framework for the doubly-dispersive channel is presented for MIMO. Unlike [78], where UW was placed outside of the FFT block, our system uses the UW for channel estimation in the time domain.

In [79], a study on *Cyclic-Prefix Orthogonal Time Frequency Space* (CP-OTFS) in fractional Doppler channels and residual synchronization errors is presented. This work introduces the idea of a time-domain estimation of the fractional Doppler channel by sampling the LTV channel with N samples and using a polynomial spline to interpolate the rest. Our approach exploits a similar idea, only the pilot is located directly in the time domain, rather than in the DD domain, and a Bayesian estimator is used instead of polynomial interpolation. However, the guard band is omitted in [79], making it hard to compare with UW-OTFS.

In [80], a novel OFDM-based OTFS is designed with pilots located in the *Frequency-Time* (FT) domain. It is designed to cope with fractional delays, using the MUSIC algorithm, and with fractional Doppler frequencies, using a line-fitting. However, unlike in our approach, the guard band is omitted and a prior knowledge of the DD domain channel tap count N_t is necessary for the design in [80].

In [81], a pilot superposition idea (similar to ours) is utilized. However, there the pilots are superimposed directly into the delay-Doppler data matrix and no guard band is used. Therefore, the design cannot be compared with the UW-OTFS.

An interesting phenomenon, known as the Doppler squint effect has been published in [82]. In Section 5.1.6 we reflect this finding in our LTV channel model.

5 Introduction to the OTFS

This chapter introduces some of the main concepts necessary for a detailed understanding of the OTFS functionality.

5.1 Preliminaries

5.1.1 Notation

The following mathematical notation is used hereinafter:

- scalar variable example c
- column vector examples $\mathbf{v}$, $\mathbf{V}$, its single entry $\mathbf{v}[m]$, $\mathbf{V}[m]$
- size $M \times M$ unit matrix $\mathbf{I}_M$
- full matrix $\bar{\mathbf{F}}$; its single entry $\bar{\mathbf{F}}[m, n]$
- higher-dimensional matrix (tensor) $\bar{\bar{\mathbf{A}}}$; its single entry (3D example) $\bar{\bar{\mathbf{A}}}[m, n, p]$
- set definition $\mathcal{M} := \{0, 1, \ldots M - 1\}$; a single entry $\mathcal{M}[m]$
- function or a discrete sequence $f(.)$ or $s(.)$.

The entries of products of vectors/matrices/tensors can also be addressed via the square bracket notation, e.g., if $\check{\mathbf{X}} = \bar{\mathbf{G}}\bar{\mathbf{X}}$ then $\check{\mathbf{X}}[p, q]$ is the same as $\bar{\mathbf{G}}\bar{\mathbf{X}}[p, q]$.

5.1.2 Discrete Fourier Transform

Discrete Fourier Transform (DFT) is the fundamental element in digital signal processing. In this document, I will use the unitary matrix representation of DFT, defined as

$$\bar{\mathbf{F}}_M[p, q] = \frac{1}{\sqrt{M}} e^{-j2\pi \frac{pq}{M}} \quad \forall \quad p, q \in \{0, 1, \ldots, M - 1\}, \tag{5.1}$$

where the size of $\bar{\mathbf{F}}_M$ is $M \times M$. The IDFT is expressed by $\bar{\mathbf{F}}_M^*$ which is equivalent to $\bar{\mathbf{F}}_M^H$ (a more frequently used form in the OTFS literature).

5.1.3 Symplectic Fourier Transform

The SFT, or discrete SFT is a key operation in OTFS, as it transforms the signal from the FT domain to the DD domain. SFT is defined as IDFT in one dimension and DFT in the other, which is expressed by [41]

$$\bar{\mathbf{x}}[p, q] = \frac{1}{\sqrt{MN}} \sum_{m=0}^{M-1} \sum_{n=0}^{N-1} \bar{\mathbf{X}}[m, n] e^{j2\pi \frac{pm}{M}} e^{-j2\pi \frac{qn}{N}}, \tag{5.2}$$

or equivalently, using the matrix notation with the unitary DFT matrices,

$$\bar{\mathbf{x}} = \bar{\mathbf{F}}_M^* \bar{\mathbf{X}} \bar{\mathbf{F}}_N. \tag{5.3}$$

Here $\bar{\mathbf{x}}$ and $\bar{\mathbf{X}}$ represent arbitrary complex matrices of size $M \times N$ in the DD and FT domain, respectively. The reverse operation, i.e., from DD to FT domain, is performed by the *Inverse Symplectic Fourier Transform* (ISFT), which is defined by

$$\bar{\mathbf{X}} = \bar{\mathbf{F}}_M \bar{\mathbf{x}} \bar{\mathbf{F}}_N^*. \tag{5.4}$$

5.1.4 Subcarrier Mapping in OTFS

In multi-carrier systems such as OFDM, it is a common practice to introduce the guard band in the frequency domain, which has a purpose of reducing the spectral OOB emissions. There are two basic ways of implementing the guard band:

- the *Wireless Local Area Network* (WLAN) subcarrier mapping (with a suppressed DC subcarrier)
- asymmetrical subcarrier mapping - the DC subcarrier is not suppressed.

The difference between the WLAN and the asymmetrical type of subcarrier mapping is depicted in Fig. 5.1. The proposed UW-OTFS requires having a symmetrical subcarrier mapping because of the non-systematical precoding matrix $\bar{\mathbf{G}}$, therefore it uses the WLAN type. The CP-OTFS (discussed in Section 6.8) has no such requirements, therefore it may use either of them.
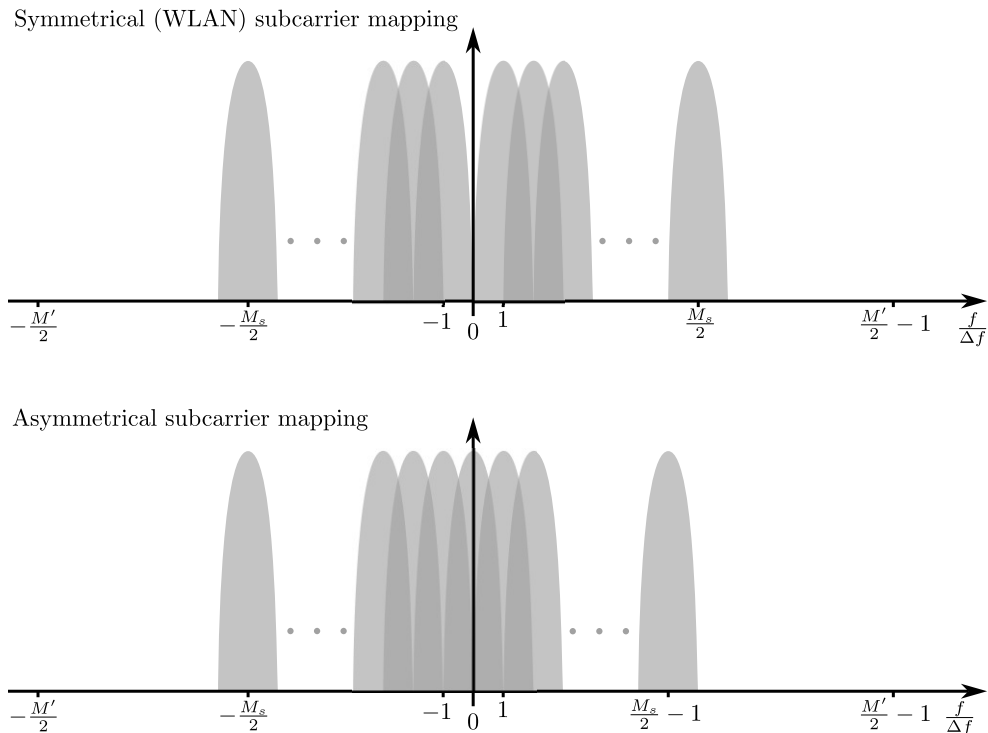

Fig. 5.1: Illustration of the WLAN and asymmetrical subcarrier mapping in OTFS (M_s is the number of active subcarriers, M' is the total number of subcarriers).

5.1.5 Linear Time-Variant Channel

The simulation framework used for the numerical BER analysis was created in MAT-LAB and as such, requires discretization of the time domain. For this reason, the UW-OTFS waveform, as well as the LTV channel, are defined in the discrete-time domain. The effects of the LTV channel on an arbitrary waveform $s(.)$ are described by

$$y(k) = \sum_{k_{\tilde{\tau}}=0}^{M_{\tilde{\tau}}-1} \mathbf{h}_k[k_{\tilde{\tau}}]s(k - k_{\tilde{\tau}}), \tag{5.5}$$

where $y(.)$ is the resultant waveform, $\mathbf{h}_k[.]$ is the $M_{\tilde{\tau}} \times 1$ vector of the LTV CIR at time k and $M_{\tilde{\tau}}$ is the maximum number of channel taps in the resampled delay domain[1]. Equivalently, this could be defined using the sparse channel model (similar to (20) in [44])

$$y(k) = \sum_{i=0}^{N_t-1} \mathbf{h}[i]s(k - \mathbf{k}_{\tilde{\tau}}[i])e^{j2\pi \mathbf{v}[i]k\Delta T}, \tag{5.6}$$

where ΔT is the sampling period and where instead of the delay-time domain CIR vector $\mathbf{h}_k$ we use an $N_t \times 1$ vector of complex gains $\mathbf{h}$, $N_t \times 1$ vector of delay indices $\mathbf{k}_\tau$ from within $\{0, 1, \ldots, M_{\tilde{\tau}} - 1\}$ and an $N_t \times 1$ vector of Doppler frequencies $\mathbf{v}$ from within the range $\langle -\nu_m, \nu_m \rangle$. Here, ν_m is the maximal expected Doppler frequency in Hz, calculated as

$$\nu_m = f_0 \frac{\mathbf{v}_0}{3.6 \cdot c_0}. \tag{5.7}$$

where $\mathbf{v}_0$ is the maximum velocity in km/h, f_0 is the carrier frequency in Hz and c_0 is the speed of light $2.998 \cdot 10^8$ m/s. Because the UW-OTFS RX processing takes advantage of zero IBI, and also to ensure a proper CE quality, we assume that

$$M_{\tilde{\tau}} \leq M_{gi}/2. \tag{5.8}$$

Fig. 5.2 displays an example of such a channel with $N_t = 4$ in the DD domain.

5.1.6 Doppler Squint Effect

In [82] an important phenomenon related to LTV channels called the *Doppler Squint Effect* (DSE) has been introduced. This section's purpose is to prove, that the discrete-time domain LTV channel, defined in (5.6) is respecting the DSE. DSE is best illustrated on the following scenario. A base-band waveform $s(t)$ has been

---

[1]As will be shown in Section 6.2, the use of a guard band demands to distinguish the delay domain of size M, where data symbols are located, from the delay domain of size M' that is located behind the transmitter's IDFT. Hence, we chose to call the latter the resampled delay domain, denoted by $\tilde{\tau}$.
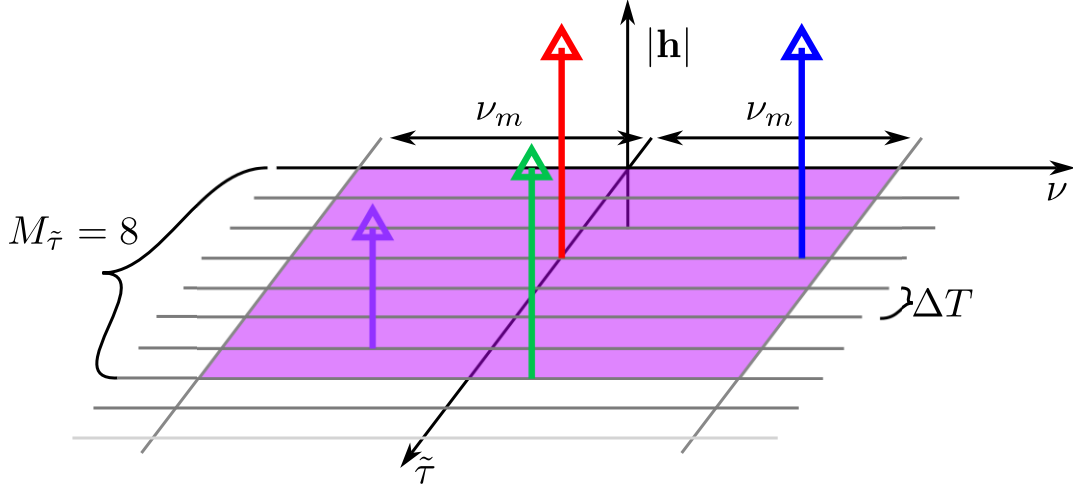
Fig. 5.2: Sparse LTV channel example ($N_t = 4$, displayed in the resampled-delay-Doppler domain).

up-converted to a pass-band carrier frequency f_c. After passing through the LTV channel with a finite number of taps N_t, the received waveform $\hat{r}(t)$ is described as

$$\hat{r}(t) = \sum_{i=0}^{N_t-1} \Re\left\{ h_i s\left(t - \tau_i(t)\right) e^{j2\pi f_c(t-\tau_i(t))} \right\}, \qquad (5.9)$$

where, h_i is the complex path gain, $\tau_i(t) = \tau_i - t\nu_i/f_c$ defines the time-variant delay of a path whose reflector is approaching with constant velocity v_i. Here $\nu_i = f_c v_i/3.6/c$, c is the speed of light in m/s and v_i is the mutual velocity between receiver and transmitter in km/h. After down-converting (5.9) to the base-band, we obtain

$$r(t) = \sum_{i=0}^{N_t-1} h_i s\left(t - \tau_i(t)\right) e^{-j2\pi f_c \tau_i(t)} = \sum_{i=0}^{N_t-1} h_i e^{-j2\pi f_c \tau_i} e^{j2\pi \nu_i t} s\left(t - \tau_i + \frac{\nu_i}{f_c} t\right). \quad (5.10)$$

Here $s\left(t - \tau_i + t\nu_i/f_c\right)$ is transferred into the discrete-time domain as $s\left(k - \mathbf{k}_{\tilde{\tau}}[i] + \lfloor k\nu_i/f_c \rfloor\right)$, where $\lfloor . \rfloor$ is the floor function. In case of our numerology (see Section 6.9), where $M' = 64$, $N = 16$, $f_c = 5~GHz$, $= 500~km/h$, and where $\nu_i = 1.853~kHz$, we evaluate the maximum time-variant delay $\lfloor M'N\nu_i/f_c \rfloor$ as $\lfloor 3.795e-4 \rfloor = 0$. Formula (5.10) in the discrete-time domain yields

$$r(k) = \sum_{i=0}^{N_t-1} h_i e^{-j2\pi \mathbf{k}_{\tilde{\tau}}[i] f_c \Delta T} e^{j2\pi \nu_i k \Delta T} s\left(k - \mathbf{k}_{\tilde{\tau}}[i] + \lfloor k\nu_i/f_c \rfloor\right), \qquad (5.11)$$

which, after defining the channel gain vector as

$$\mathbf{h}[i] = h_i e^{-j2\pi \mathbf{k}_{\tilde{\tau}}[i] f_c \Delta T}, \qquad (5.12)$$

becomes identical to the LTV channel model in (5.6). In other words, the LTV channel model (5.6), used in the remainder of this thesis, is in complete agreement with the DSE model as long as $\lfloor M'N\nu_i/f_c \rfloor$ equals to zero.

5.2 OTFS - Original Definition

According to the original publication [38], the OTFS transmission chain begins by placing data symbols in the DD domain, forming an $M \times N$ matrix $\bar{\mathbf{x}}$, which is then transformed to the FT domain $M \times N$ matrix using the ISFT, according to

$$\bar{\mathbf{X}}[p,q] = \frac{1}{\sqrt{MN}} \sum_{m=0}^{M-1} \sum_{n=0}^{N-1} \bar{\mathbf{x}}[m,n] e^{-j2\pi \frac{mp}{M}} e^{j2\pi \frac{nq}{M}}. \tag{5.13}$$

After this, the Heisenberg transform is applied, yielding the continuous TD waveform [41]

$$s(t) = \sum_{m=0}^{M-1} \sum_{n=0}^{N-1} \bar{\mathbf{X}}[m,n] g_{tx}(t-nT) e^{j2\pi m \Delta f(t-nT)}, \tag{5.14}$$

where $g_{tx}(.)$ is a TX pulse shape and the LTV channel model, widely used in many publications, is given by [38, 40, 41] (AWGN neglected)

$$r(t) = \int \int h(\tau, \nu) s(t-\tau) e^{j2\pi\nu(t-\tau)} \, d\tau \, d\nu, \tag{5.15}$$

where the sparse DD CIR function is defined by[2]

$$h(\tau, \nu) = \sum_{i=0}^{N_t-1} \mathbf{h}_i \delta(\tau - \tau_i) \delta(\nu - \nu_i). \tag{5.16}$$

for $\mathbf{h}_i \sim \mathcal{CN}(0,1)$. On the RX side, the matched filtering is performed according to the Wigner transform,

$$\bar{\mathbf{Y}}[m,n] = \int g_{rx}^*(t-nT) r(t) e^{-j2\pi m \Delta f(t-nT)} \, dt, \tag{5.17}$$

where g_{rx} is the RX pulse shape. The FT domain $M \times N$ matrix $\bar{\mathbf{Y}}$ can also be expressed as

$$\bar{\mathbf{Y}}[m,n] = \sum_{m'=0}^{M-1} \sum_{n'=0}^{N-1} \bar{\mathbf{H}}_{m,n}[m',n'] \bar{\mathbf{X}}[m',n'], \tag{5.18}$$

where $\bar{\mathbf{H}}_{m,n}$ represents the FT domain *Equivalent Channel Matrix* (ECM), encapsulating all of the LTV channel behavior including the TX/RX pulse shaping functions. Now, depending on the pulse shaping function design and on whether any GI was included, formula (5.18) may be simplified to

$$\bar{\mathbf{Y}}[m,n] = \sum_{m'=0}^{M-1} \bar{\mathbf{H}}_n[m,m'] \bar{\mathbf{X}}[m',n], \tag{5.19}$$

in case of a rectangular pulse shaping and multiple CP inclusion [51, 52], to

$$\bar{\mathbf{Y}}[m,n] = \sum_{m'=0}^{M-1} \sum_{n'=n-1}^{n} \bar{\mathbf{H}}_{m,n}[m',n'] \bar{\mathbf{X}}[m',n'], \tag{5.20}$$

---

[2]Please note, that this definition is may be inaccurate, i.e., in disagreement with the DSE [82]. Refer to Section 5.1.6 for further information.

in the case of rectangular pulse shaping and a single CP inclusion [40, 41], or to

$$\bar{\mathbf{Y}}[m, n] = \bar{\mathbf{H}}[m, n]\bar{\mathbf{X}}[m, n], \tag{5.21}$$

in the case of ideal bi-orthogonal pulse shaping [38, 41]. The equalization then progresses differently, depending on the particular OTFS waveform variant, the channel model, the CE technique, etc. The equalized data symbols are transformed back to the DD domain using the SFT.

6 Unique Word OTFS - Detailed Analysis

This chapter summarizes the contribution in the field of OTFS, which lies in a detailed description of the proposed UW-OTFS [7] and in its theoretical and numerical analysis.

6.1 System Parameters

We start with definitions of the UW-OTFS system parameters:
- subcarrier spacing Δf
- number of samples per OTFS symbol M' (preferably a power of two, so the FFT algorithm can be used)
- number of OTFS symbols per transmission N (the Doppler domain size; preferably a power of two)
- number of samples per guard interval M_{gi}
- number of redundant subcarriers M_r (must be greater or equal to M_{gi} [62,63])
- number of data symbols per OTFS symbol M (the delay domain size)
- number of active subcarriers (data plus redundancy) $M_s = M + M_r$
- number inactive subcarriers (i.e., the guard band) $M_z = M' - M_s$
- the DSF n_ν (explained in Section 6.7)
- nominal Doppler resolution $\Delta \nu = \frac{\Delta f}{N}$.

Note: In this work, we choose the redundant subcarrier count $M_r = M_{gi}$ as it was done in [60, 62].

6.2 UW-OTFS Transmitter Design

The transmitter structure of the UW-OTFS is shown in Fig. 6.2. The input $M \times N$ m-QAM symbol matrix $\bar{\mathbf{x}}$ defined in the DD domain is first transformed into the
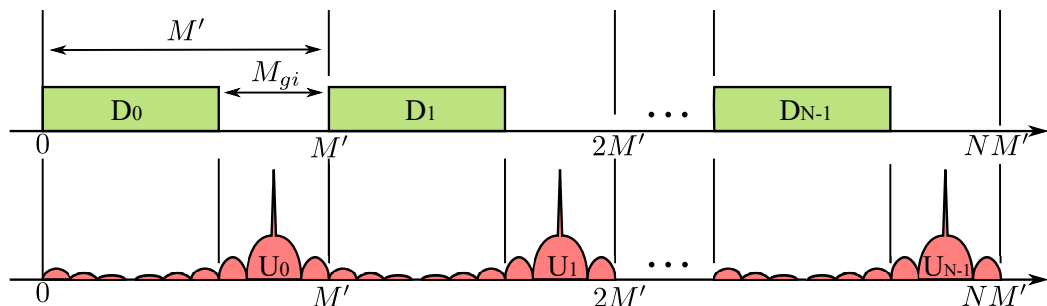

Fig. 6.1: Waveform diagram of the UW-OTFS split into the data part (top) and the UW sequence part (bottom).
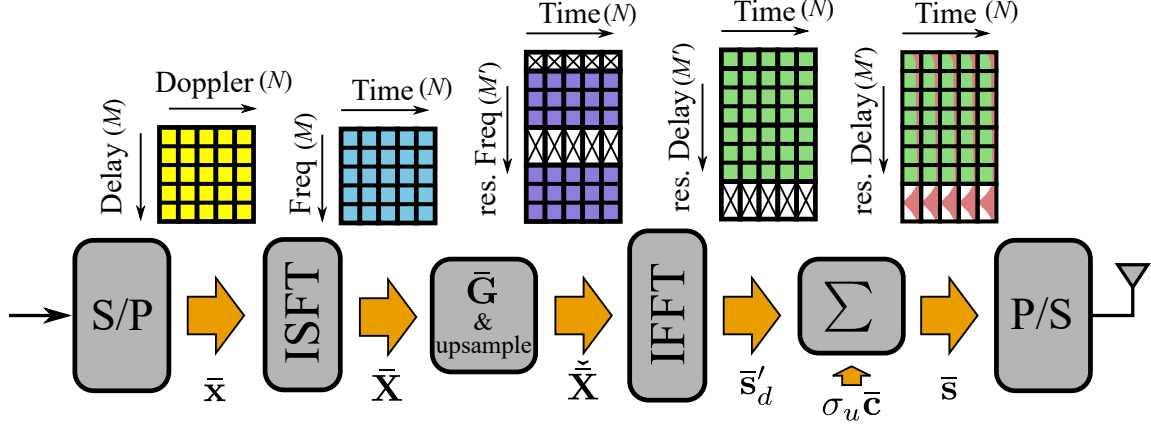
Fig. 6.2: UW-OTFS transmitter block schematic.

FT domain using the ISFT, according to

$$\bar{\mathbf{X}} = \bar{\mathbf{F}}_M \bar{\mathbf{x}} \bar{\mathbf{F}}_N^*, \tag{6.1}$$

The FT domain matrix $\bar{\mathbf{X}} \in \mathbb{C}^{M \times N}$ is then transformed into the $M_s \times N$ precoded matrix as

$$\check{\bar{\mathbf{X}}} = \bar{\mathbf{G}} \bar{\mathbf{X}}, \tag{6.2}$$

where $\bar{\mathbf{G}}$ is the so-called "non-systematic" precoding matrix of size $M_s \times M$ that is pre-calculated offline. $\bar{\mathbf{G}}$ was first introduced in [63] as the case-2 matrix $\check{\mathbf{G}}''$, which automatically adds M_r redundant subcarriers to the M data subcarriers such that a GI of length M_{gi} with all elements being zero is then created in time domain. The guard band is essential for preventing the IBI. Note that $M_r = M_s - M$ and that in our case $M_r = M_{gi}$. The complete time domain UW-OTFS waveform matrix of size $M' \times N$ is given by

$$\bar{\mathbf{s}} = \alpha \bar{\mathbf{F}}_{M'}^* \bar{\mathbf{B}} \bar{\mathbf{G}} \bar{\mathbf{X}} + \sigma_u \bar{\mathbf{c}} = \left(\bar{\mathbf{s}}_d^T \quad \bar{\mathbf{0}}_{M_{gi} \times N}^T \right)^T + \sigma_u \bar{\mathbf{c}}, \tag{6.3}$$

where $\bar{\mathbf{0}}_{M_{gi} \times N}$ is the GI, occurring naturally due to $\bar{\mathbf{G}}$, $\bar{\mathbf{c}}$ is the energy-normalized UW sequence matrix (see Section 6.3), and $\bar{\mathbf{B}}$ is a sparse guard-band insertion matrix, defined as $\bar{\mathbf{B}}\big[\mathcal{M}_s[p], p\big] = 1$ for $p \in \{0, 1, \ldots, M_s - 1\}$. Here, $\mathcal{M}_s$ is the set of active subcarrier indices (using the symmetrical WLAN subcarrier mapping with a suppressed DC subcarrier [62, 63]), defined as

$$\mathcal{M}_s := \left\{ 1, 2, \ldots, \frac{M_s}{2}, M' - \frac{M_s}{2}, M' - \frac{M_s}{2} + 1, \ldots, M' - 1 \right\}. \tag{6.4}$$

70

Note that any modification of $\mathcal{M}_s$ requires new optimization of $\bar{\mathbf{G}}$. Next, we define the TX data part windowing function as

$$g_d(k) = \begin{cases} \frac{1}{\sqrt{M'}} & \forall \quad k \in \{0, 1, \ldots, M' - M_{gi} - 1\} \\\\ 0 & \text{otherwise.} \end{cases} \tag{6.5}$$

and the UW-OTFS waveform (just the data part) is then defined as

$$s_d(k) = \alpha \sum_{n'=0}^{N-1} \sum_{m'=0}^{M_s-1} \breve{\mathbf{X}}[m', n'] g_d(k - n'M') e^{j2\pi \mathcal{M}_s[m']\frac{k}{M'}}. \tag{6.6}$$

The TX power normalization coefficient is defined as

$$\alpha^2 = \frac{M'(1 - \sigma_u^2)}{\text{tr}\left\{\bar{\mathbf{G}}^H \bar{\mathbf{G}}\right\}}. \tag{6.7}$$

where σ_u^2 represents the mean UW sequence energy.

6.3 UW Sequence Design

The UW, as used in UW-OTFS, represents a GI inserted within the FFT block of a given waveform. For this type of GI, the particular UW sequence would not be so important, since it is the absence of data symbols in the GI that enables the block-wise RX processing and causes *Inter-Symbol Interference* (ISI) mitigation. The UW sequence, for being deterministic and known to receiver, can be treated as a separate waveform that is superimposed to the data, rather than concatenated to it. It is a common misconception in both the UW SC-FDE and UW-OTFS literature, that the UW must necessarily fit into the GI. In fact, there is no reason not to spread the UW sequence across the whole FFT block, since it can be readily subtracted on the RX side, due to the superposition principle. More so, there can be a different UW sequence for each FFT block (i.e., for each OTFS symbol), for that matter. This is one of the key ideas in this thesis.

In the original UW-OFDM, the UW sequence was located strictly in the guard interval, therefore, it was limited to the length of M_{gi} samples. We prove not only that the UW sequence can stretch out to the whole OTFS symbol length (i.e., M' samples), but also that the UW sequences need not be identical for all OTFS symbols in the waveform. More precisely, by introducing deterministic variations between the UW sequences, we are able to smooth out the spectrum spikes, that would be present otherwise.

There are many ways of generating a unique word for CE purposes, the most popular being the ZC sequences [75]. Even though they are optimal in the sense

of PAPR and PSD flatness, both of these advantages are lost if the sequence is appended by zeros in the time domain. Also, in LTV channels only short ZC sequences can be used effectively [75].

In this work, we decided to relax the low PAPR requirement and maximize the CE quality while also preserving the superb OOB emissions natural to UW-OFDM.

The UW design begins in the frequency domain, by specifying the set of active subcarriers as $\mathcal{M}'_s = \mathcal{M}_s \cup \{0\}$ (i.e., by adding the DC subcarrier). The normalized UW vector of size $M'N \times 1$ is defined as

$$\mathbf{c}_0[p] = \frac{1}{\sqrt{M' - M_s - 1}} \sum_{k \in \mathcal{M}'_s} e^{j2\pi \frac{k}{M'} \left(p + \frac{M_{gi}}{2} \right)}. \tag{6.8}$$

This sequence has a period of M' samples and it is shifted by $M_{gi}/2$ samples in order to move its high energy region (98.4% of total UW energy, given $M' = 64$ and $M_{gi} = 16$) into the guard interval. However, due to its periodicity, this sequence contains spikes in the spectrum, that are more than 6 dB above the mean spectral density level. This problem can easily be solved by multiplying $\mathbf{c}_0$ with a linear chirp sequence with a period of $M'N$ samples, yielding the final sequence

$$\mathbf{c}[p] = \frac{e^{-j\pi \frac{p}{M'} \left(\frac{p}{M'N} - 1 \right)}}{\sqrt{M' - M_s - 1}} \sum_{k \in \mathcal{M}'_s} e^{j2\pi \frac{k}{M'} \left(p + \frac{M_{gi}}{2} \right)}. \tag{6.9}$$

The $M' \times N$ UW matrix is defined by reshaping $\mathbf{c}$ according to $\bar{\mathbf{c}}[m, n] = \mathbf{c}[m + nM']$ for $m \in \{0, 1, \ldots M' - 1\}$ and $n \in \{0, 1, \ldots N - 1\}$. The left side of Fig. 6.3 shows the average PSD of the UW-OTFS with the proposed UW in (6.9) compared with the Dirac impulse UW sequence, defined in (6.10). This way, we may notice how an improper UW design can destroy the otherwise superb OOB emissions of the original UW-OFDM [63]. The right side of Fig. 6.3 contains a statistical analysis of the transmit waveform energy within one UW-OTFS symbol (i.e., in the time domain) simulated numerically using 4000 transmissions. Here, D1 and D9 represent the first and the ninth decile of the energy in each bin of the UW-OTFS symbol, therefore, we may tell apart the random and deterministic sections of the waveform. This display also gives some insight into the PAPR, which will be discussed more in Section 6.8. In Fig. 6.4, we can see the same type of comparison, only for the proposed UW with and without the chirp sequence spreading. It is not surprising that using the linear chirp spread does not alter the energy profile, however, as it was already mentioned, it is responsible for smoothing-out the spectral spikes visible in the PSD.
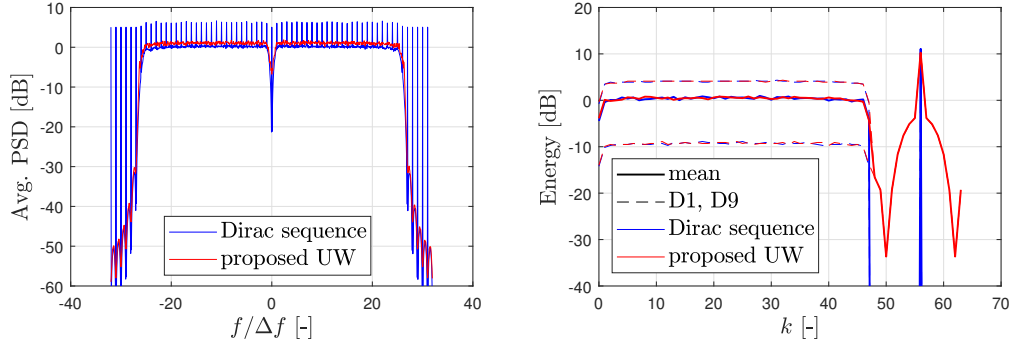
Fig. 6.3: Average PSD (left) and waveform energy (right) comparison of the UW-OTFS transmit waveform (i.e., data and UW) with the Dirac UW sequence (6.10) and the proposed UW sequence (6.9).
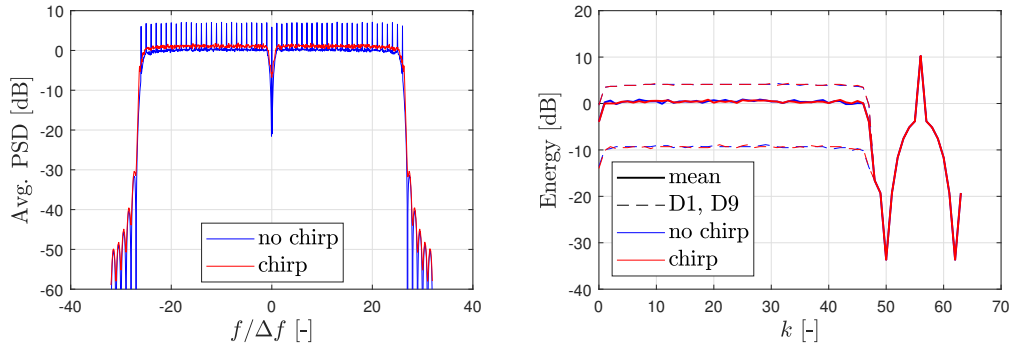

Fig. 6.4: Average PSD (left) and waveform energy (right) comparison of the UW-OTFS transmit waveform (i.e., data and UW) using the proposed UW sequence with and without the chirp sequence, i.e., (6.9) and (6.8).

6.4 Channel Estimation

CE is a lively topic in the recent OTFS literature. Originally, CE was performed by embedding a pilot symbol in the DD domain and extracting it on the RX side [42, 44, 45]. However illustrative it may be, the main inconveniences of the embedded pilot CE method are:

- a need to perform SFT on the receiver prior to CE
- troublesome in channels with fractional Doppler.

The straightforward way of improving the CE in fractional Doppler channels is to decrease the Doppler resolution, $\Delta\nu$. In OTFS, the Doppler resolution is reciprocal to the total OTFS transmission time $T_{tx} = N/\Delta f$ [41, 52] and in UW-OTFS it equals $\Delta\nu = \Delta f/N$, where Δf is the subcarrier spacing. A refinement of $\Delta\nu$ can be achieved either by decreasing Δf or by increasing the number of OTFS symbols

N. However, both approaches increase the total transmission time T_{tx}, which is an unwanted effect due to the latency. To keep the latency small, the following CE method was developed.

6.4.1 The Proposed CE Method - Dirac Impulse UW Sequence

We begin by describing the CE chain with the most illustrative type of the UW sequence. This would be a sequence of N discrete Dirac delta functions, defined by

$$s_u(k) = \sigma_u \sqrt{M'} \sum_{n'=0}^{N-1} \delta\big(k - n'M' - k_x\big), \tag{6.10}$$

where $k_x = M' - M_{gi}/2$, which passes through the channel (5.6) as (without AWGN)

$$y_u(k) = \sigma_u \sqrt{M'} \sum_{i=0}^{N_t-1} \mathbf{h}[i] \sum_{n'=0}^{N-1} \delta\big(k - \mathbf{k}_{\tilde{\tau}}[i] - n'M' - k_x\big)e^{j2\pi\mathbf{v}[i]k\Delta T}. \tag{6.11}$$

The first step of the proposed CE method is an extraction of the last $M_{gi}/2$ samples of each received OTFS symbol (as long as $M_{\tilde{\tau}} \le M_{gi}/2$, the extracted samples are not contaminated by the data). The $M_{gi}/2 \times N$ CE matrix is defined as

$$\bar{\mathbf{y}}_{ce}[m, n] = y_u(m + M'n + k_x), \tag{6.12}$$

and after including (6.11) it is expanded into

$$\bar{\mathbf{y}}_{ce}[m, n] = \sigma_u \sqrt{M'} \sum_{i=0}^{N_t-1} \mathbf{h}[i]\delta\big(m - \mathbf{k}_{\tilde{\tau}}[i]\big)e^{j2\pi \frac{\mathbf{v}[i]}{\Delta f} \frac{m+M'n+k_x}{M'}}. \tag{6.13}$$

Unlike in [80], here we assume that the number of channel taps N_t is not known to the receiver. Because the CSI is distributed into three different vectors of unknown length N_t, i.e., $\mathbf{h}$, $\mathbf{k}_{\tilde{\tau}}$ and $\mathbf{v}$, it is hard to extract it directly from $\bar{\mathbf{y}}_{ce}$. Therefore, we unify the CSI into a single matrix (of known dimensions) that can be estimated from the CE matrix (6.12). As I found out by accident later on, this method of CE is very similar to the already known GCE-BEM [71], which was mentioned in Section 4.4.

The proposed unification of the CSI begins by sampling the continuous Doppler domain into a lattice of size N with Doppler resolution $\Delta\nu$, defined as

$$\mathcal{V} := \Big\{-N/2, -N/2 + 1\ldots, N/2 - 1\Big\}. \tag{6.14}$$

Once both delay and Doppler form a lattice, the (estimated) CSI can be contained by an $M_{gi}/2 \times N$ matrix of complex channel gains $\bar{\mathbf{h}}$, denoted as the **root matrix**[1][2].

---

[1]We chose to fix the resampled delay domain size for the root matrix to $M_{gi}/2$, regardless of the actual $M_{\tilde{\tau}}$, as long as $M_{\tilde{\tau}} \le M_{gi}/2$

[2]Notice the similarity to the GCE-BEM coefficient matrix

The LTV channel model in (5.6)

$$y(k) = \sum_{i=0}^{N_t-1} \mathbf{h}[i]s(k - \mathbf{k}_{\tilde{\tau}}[i])e^{j2\pi \mathbf{v}[i]k\Delta T},$$

is then modified into the **discrete LTV channel model**, defined as

$$\tilde{y}_u(k) = \sum_{k_{\tilde{\tau}}=0}^{M_{gi}/2-1} s_u(k - k_{\tilde{\tau}}) \sum_{k_\nu=0}^{N-1} \bar{\mathbf{h}}[k_{\tilde{\tau}}, k_\nu]e^{j2\pi \frac{\mathcal{V}[k_\nu]k}{n_\nu NM'}}, \tag{6.15}$$

and the CE matrix yields

$$\tilde{\bar{\mathbf{y}}}_{ce}[m, n] = \sigma_u \sqrt{M'} \sum_{k_\nu=0}^{N-1} \bar{\mathbf{h}}[m, k_\nu]e^{j2\pi k_\nu \frac{m+M'n+k_x}{n_\nu M'N}}. \tag{6.16}$$

Unlike in (6.13), the CSI in (6.16) (i.e., the root matrix) has the same dimensions as $\tilde{\bar{\mathbf{y}}}_{ce}$, thus forming a linear system of equations from which $\bar{\mathbf{h}}$ may be estimated using the LMMSE estimator. Please note, that (6.15) was created only for the sake of explaining the proposed CE method. The actual LTV channel is defined in (5.6). One important parameter of the discrete LTV channel model (6.15) is the DSF, n_ν, which is essential for improving the CE quality in the fractional Doppler channels. The DSF will be analyzed in Section 6.7.

6.4.2 Relation between the Original and Unified CSI

The relation between the original three CSI vectors, $\mathbf{h}$, $\mathbf{k}_{\tilde{\tau}}$ and $\mathbf{v}$ and the root matrix $\bar{\mathbf{h}}$ can be found once we force an equality of $\tilde{\bar{\mathbf{y}}}_{ce}$ in (6.16) and $\bar{\mathbf{y}}_{ce}$ in (6.13). In other words, we may express the m-th transposed row of $\tilde{\bar{\mathbf{y}}}_{ce}$ (i.e., an $N \times 1$ vector) as

$$\tilde{\mathbf{y}}_{ce,m}[n] = \sum_{k_\nu=0}^{N-1} \bar{\mathbf{A}}_{ce,m}[n, k_\nu]\mathbf{h}_m[k_\nu], \tag{6.17}$$

where $\mathbf{h}_m$ is the m-th transposed row of the root matrix and where

$$\bar{\mathbf{A}}_{ce,m}[n, k_\nu] = \sigma_u \sqrt{M'}e^{j2\pi \frac{\mathcal{V}[k_\nu]}{n_\nu} \frac{m+M'n+k_x}{M'N}}, \tag{6.18}$$

in an $N \times N$ matrix. The root matrix can now be calculated from the original CE matrix, $\bar{\mathbf{y}}_{ce}$, separately for each row index m, by solving

$$\mathbf{y}_{ce,m} = \bar{\mathbf{A}}_{ce,m}\mathbf{h}_m. \tag{6.19}$$

Because the rank of $\bar{\mathbf{A}}_{ce,m}$ is lower than N, it is impossible to invert such a matrix. The solution can be approximated via the pseudo-inversion

$$\tilde{\mathbf{h}}_m = \bar{\mathbf{A}}_{ce,m}^H \left(\bar{\mathbf{A}}_{ce,m}\bar{\mathbf{A}}_{ce,m}^H + \gamma \mathbf{I}_N \right)^{-1} \mathbf{y}_{ce,m}, \tag{6.20}$$

where $\gamma = \sigma_w^2 M_{gi}N/2$ is a constant originating in the LMMSE criterion, which takes AWGN into consideration. Fig. 6.5 shows this relation for a random example of the LTV channel.
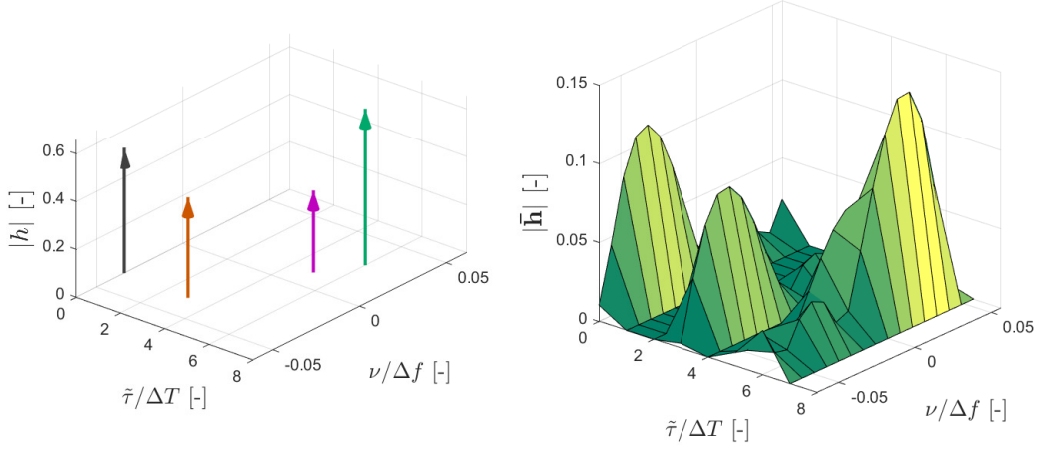
Fig. 6.5: An example of the sparse LTV channel (5.6) and the corresponding channel root matrix (i.e., GCE-BEM coefficient matrix), defined by (6.20).

6.4.3 The Proposed CE Method - Generalized UW

While being simple to work with, the sequence of discrete Dirac delta functions has a very wide bandwidth which increases the otherwise low OOB emissions of UW-OTFS. Therefore, for further evaluations we use a generalized UW sequence matrix $\bar{\mathbf{c}}$, which was fully described in Section 6.3. The UW waveform is defined as

$$s_u(k) = \sigma_u \sqrt{M'} \sum_{n'=0}^{N-1} \bar{\mathbf{c}}\Big[(k)_{M'}, n'\Big] g_0(k - n'M'), \tag{6.21}$$

where

$$g_0(k) = \begin{cases} \dfrac{1}{\sqrt{M'}} & \forall \quad k \in \{0, 1, \dots, M'-1\} \\[2mm] 0 & \text{otherwise.} \end{cases} \tag{6.22}$$

Please note, that even though the UW-OTFS waveform consists of $s_d(k) + s_u(k)$, the data part $s_d(k)$ does not affect the CE matrix (6.12) as long as $M_{\tilde{\tau}} \leq M_{gi}/2$. Once $s_u(k)$ passes through the discrete LTV channel (6.15), $\tilde{y}_u(k)$ is obtained and the CE matrix in (6.12) is evaluated as (without AWGN)

$$\bar{\tilde{\mathbf{y}}}_{ce}[m, n] = \sum_{k_{\tilde{\tau}}=0}^{M_{gi}/2-1} \sum_{k_\nu=0}^{N-1} \bar{\bar{\mathbf{A}}}_{ce}[m, n, k_{\tilde{\tau}}, k_\nu] \bar{\mathbf{h}}[k_{\tilde{\tau}}, k_\nu], \tag{6.23}$$

where the $M_{gi}/2 \times N \times M_{gi}/2 \times N$ tensor is defined as

$$\bar{\bar{\mathbf{A}}}_{ce}[m, n, k_{\tilde{\tau}}, k_\nu] = \sigma_u e^{j2\pi \frac{\mathcal{V}[k_\nu](m+M'n+k_x)}{n_\nu N M'}} \bar{\mathbf{c}}\Big[(m - k_{\tilde{\tau}} - \frac{M_{gi}}{2})_{M'}, n\Big]. \tag{6.24}$$

The relation in (6.23) can be reshaped into a linear system (after adding the AWGN matrix $\bar{\mathbf{w}}_{ce}$)

$$\mathbf{r}_{ce} = \bar{\mathbf{A}}_{ce}\hat{\mathbf{h}} + \mathbf{w}_{ce}, \tag{6.25}$$

where $\mathbf{r}_{ce} = \text{vect}\{\bar{\mathbf{y}}_{ce}+\bar{\mathbf{w}}_{ce}\}$, $\mathbf{w}_{ce} = \text{vect}\{\bar{\mathbf{w}}_{ce}\}$, $\hat{\mathbf{h}} = \text{vect}\{\bar{\mathbf{h}}\}$ and where the $M_{gi}N/2\times M_{gi}N/2$ matrix $\bar{\mathbf{A}}_{ce}$ is defined as

$$\bar{\mathbf{A}}_{ce}[p,q] = \bar{\bar{\mathbf{A}}}_{ce}\left[(p)_{\frac{M_{gi}}{2}}, \left\lfloor \frac{2p}{M_{gi}} \right\rfloor, (q)_{\frac{M_{gi}}{2}}, \left\lfloor \frac{2q}{M_{gi}} \right\rfloor\right], \tag{6.26}$$

for $p,q \in \{0,1,\ldots,M_{gi}N/2-1\}$. Here, $(.)_M$ and $\lfloor . \rfloor$ are the modulo-M and floor operations, respectively. The reshaped root matrix estimate $\tilde{\mathbf{h}}$ can be obtained with the LMMSE estimator

$$\tilde{\mathbf{h}} = \bar{\boldsymbol{\Omega}}_{ce}\mathbf{r}_{ce} = \bar{\mathbf{A}}_{ce}^{H}\left(\bar{\mathbf{A}}_{ce}\bar{\mathbf{A}}_{ce}^{H} + \gamma\mathbf{I}\right)^{-1}\mathbf{r}_{ce}, \tag{6.27}$$

where $\gamma = \sigma_w^2 M_{gi}N/2$. The estimated root matrix is then given by $\tilde{\tilde{\mathbf{h}}} = \text{vect}^{-1}\{\tilde{\mathbf{h}}\}$. Since $\bar{\mathbf{A}}_{ce}$ contains no CSI, it can be pre-calculated, and the noise variance σ_w^2 remains the only variable in the matrix inversion. Therefore, $\bar{\boldsymbol{\Omega}}_{ce}$ can be simplified into (using eigendecomposition)

$$\bar{\boldsymbol{\Omega}}_{ce} = \bar{\mathbf{A}}_{ce}^{H}\left(\bar{\mathbf{A}}_{ce}\bar{\mathbf{A}}_{ce}^{H} + \gamma\mathbf{I}\right)^{-1} = \bar{\mathbf{A}}_{ce}^{H}\bar{\mathbf{Q}}\left(\boldsymbol{\Lambda}_{ce} + \gamma\mathbf{I}\right)^{-1}\bar{\mathbf{Q}}^{H}, \tag{6.28}$$

and where $\boldsymbol{\Lambda}_{ce}$ is a diagonal matrix, containing the eigenvalues of $\bar{\mathbf{A}}_{ce}\bar{\mathbf{A}}_{ce}^{H}$ and where $\bar{\mathbf{Q}}$ is the matrix of eigenvectors. The matrix inversion of size $NM_{gi}/2\times NM_{gi}/2$ was therefore reduced into a simple vector inversion, where $\bar{\mathbf{A}}_{ce}^{H}\bar{\mathbf{Q}}$, $\boldsymbol{\Lambda}_{ce}$ and $\bar{\mathbf{Q}}^{H}$ can be pre-calculated.

6.5   Data Estimation

In order to design the data estimator, we first need to derive the input-output relation in the FT domain featuring the ECM. The ECM serves as a compact way of encapsulating all of the channel effects into a single 3D tensor. The UW-OTFS RX processing begins with DFT that produces the $M' \times N$ FT domain RX matrix, defined as

$$\bar{\mathbf{R}}[m,n] = \sum_{k=-\infty}^{\infty} g_0(k-nM')r(k)e^{-j2\pi\frac{mk}{M'}}, \tag{6.29}$$

where $r(k)$ is the received UW-OTFS waveform (including AWGN). At this point, we take advantage of the absence of IBI, allowing us to express each OTFS symbol separately. The n-th received OTFS symbol in the FT domain, $\mathbf{R}_n$, is related to the n-th column of the FT domain symbol matrix $\mathbf{X}_n$ as

$$\mathbf{R}_n = \bar{\mathbf{H}}_n\mathbf{X}_n + \mathbf{Y}_{uw,n} + \mathbf{W}_n, \tag{6.30}$$

where $\mathbf{R}_n = \bar{\mathbf{R}}\mathbf{e}_n$, $\mathbf{X}_n = \bar{\mathbf{X}}\mathbf{e}_n$, $\mathbf{Y}_{uw,n} = \bar{\mathbf{Y}}_{uw}\mathbf{e}_n$, and where $\mathbf{W}_n$ is the AWGN. Here, $\mathbf{e}_n$ is a sparse $N \times 1$ vector with 1 at the n-th position.

6.5.1 UW Subtraction

The $M' \times N$ UW matrix on the receiver side in the FT domain is calculated as (perfect CSI knowledge case, see Appendix A.1)

$$\bar{\mathbf{Y}}_{uw}[m,n] = \frac{\sigma_u}{M'} \sum_{i=0}^{N_t-1} \mathbf{h}[i] e^{-j2\pi \frac{m\mathbf{k}_\tau[i]}{M'}} e^{j2\pi \frac{\mathbf{v}[i]n}{\Delta f}} e^{j2\pi \frac{\mathbf{v}[i]\mathbf{k}_\tau[i]}{\Delta f M'}}$$

$$\times \sum_{m'=0}^{M'-1} \left\{ \bar{\mathbf{C}}[m',n-1] e^{-j2\pi \frac{\mathbf{v}[i]}{\Delta f}} \sum_{k'=M'-\mathbf{k}_\tau[i]}^{M'-1} e^{j2\pi \frac{k'}{M'}\left(m'-m+\frac{\mathbf{v}[i]}{\Delta f}\right)} \right.$$

$$\left. + \bar{\mathbf{C}}[m',n] \sum_{k'=0}^{M'-\mathbf{k}_\tau[i]-1} e^{j2\pi \frac{k'}{M'}\left(m'-m+\frac{\mathbf{v}[i]}{\Delta f}\right)} \right\}, \tag{6.31}$$

$\bar{\mathbf{C}} = \bar{\mathbf{F}}_{M'}\bar{\mathbf{c}}$. The original idea was that $\mathbf{Y}_{uw,n} = \bar{\mathbf{Y}}_{uw}\mathbf{e}_n$ would be subtracted from $\mathbf{R}_n$ before the data estimation [62]. However, while the computation of $\mathbf{Y}_{uw,n}$ is non-trivial in the perfect CSI knowledge case, it is not any less complex in the estimated CSI case, where it is calculated from the root matrix according to (see Appendix A.2)

$$\tilde{\bar{\mathbf{Y}}}_{uw}[m,n] = \sum_{k_{\tilde{\tau}}=0}^{M_{gi}/2-1} \sum_{k_\nu=0}^{N-1} \bar{\bar{\mathbf{A}}}_{uw}[m,n,k_{\tilde{\tau}},k_\nu] \tilde{\bar{\mathbf{h}}}[k_{\tilde{\tau}},k_\nu], \tag{6.32}$$

where the pre-calculated tensor of size $M' \times N \times M_{gi}/2 \times N$ is defined as

$$\bar{\bar{\mathbf{A}}}_{uw}[m,n,k_{\tilde{\tau}},k_\nu] = \frac{\sigma_u}{M'} e^{-j2\pi \frac{mk_{\tilde{\tau}}}{M'}} e^{j2\pi \frac{n\mathcal{V}[k_\nu]}{n_\nu N}} e^{j2\pi \frac{k_{\tilde{\tau}}\mathcal{V}[k_\nu]}{n_\nu NM'}}$$

$$\times \sum_{m'=0}^{M'-1} \left\{ \bar{\mathbf{C}}[m',n-1] e^{-j2\pi \frac{\mathcal{V}[k_\nu]}{n_\nu N}} \sum_{k'=M'-k_{\tilde{\tau}}}^{M'-1} e^{j2\pi \frac{k'}{M'}\left(m'-m+\frac{\mathcal{V}[k_\nu]}{n_\nu N}\right)} \right.$$

$$\left. + \bar{\mathbf{C}}[m',n] \sum_{k'=0}^{M'-k_{\tilde{\tau}}-1} e^{j2\pi \frac{k'}{M'}\left(m'-m+\frac{\mathcal{V}[k_\nu]}{n_\nu N}\right)} \right\}, \tag{6.33}$$

where $\bar{\mathbf{C}}[m',-1] = 0$ for all $m' \in \{0,1,\ldots,M'-1\}$. However, it needs to be determined how big of a benefit the UW subtraction is to the system performance, and most of all, whether it would significantly increase the overall receiver complexity (see Sections 6.6.2 for a complexity analysis).

There exists an intuitive reason for not subtracting $\mathbf{Y}_{uw,n}$ from $\mathbf{R}_n$. After the data estimation, the influence of the product of the data estimator matrix $\mathbf{\Omega}_n$ and $\mathbf{Y}_{uw,n}$ is insignificant, mostly due to the fact that the UW energy is focused around the last $M_{gi}/2$ samples of the OTFS symbol (see Fig. 6.1), which are naturally suppressed by the data estimator. This claim is supported by the numerical MSE analysis of the UW subtraction dilemma in Section 6.9.2.

6.5.2 Data Estimator - Perfect CSI Knowledge

The $M' \times M$ ECM of the n-th OTFS symbol for the perfect CSI case is defined as (see Appendix A.3)

$$\bar{\mathbf{H}}_n[p,q] = \frac{\alpha}{M'} \sum_{i=0}^{N_t-1} \mathbf{h}[i] e^{-j2\pi \frac{p\mathbf{k}_{\tilde{\tau}}[i]}{M'}} e^{j2\pi \frac{\mathbf{v}[i]\mathbf{k}_{\tilde{\tau}}[i]}{\Delta f M'}} e^{j2\pi \frac{\mathbf{v}[i]n}{\Delta f}}$$

$$\times \sum_{l=0}^{M_s-1} \sum_{k=0}^{M'-M_{gi}-1} e^{j2\pi \frac{k}{M'}\left(\mathcal{M}_s[l]-p+\frac{\mathbf{v}[i]}{\Delta f}\right)} \bar{\mathbf{G}}[l,q]. \tag{6.34}$$

The data estimation is done in the FT domain, separately for each OTFS symbol, according to

$$\tilde{\mathbf{X}}_n = \bar{\boldsymbol{\Omega}}_n \mathbf{R}_n, \tag{6.35}$$

where $\bar{\boldsymbol{\Omega}}_n$ is the LMMSE data estimator matrix of size $M \times M'$ for the n-th OTFS symbol, defined as

$$\bar{\boldsymbol{\Omega}}_n = \left(\bar{\mathbf{H}}_n^H \bar{\mathbf{H}}_n + \sigma_w^2 \mathbf{I}\right)^{-1} \bar{\mathbf{H}}_n^H. \tag{6.36}$$

The $M \times N$ matrix of DD domain m-QAM symbol estimates is then given by the SFT, defined as

$$\tilde{\bar{\mathbf{x}}} = \bar{\mathbf{F}}_M^* \sum_{n=0}^{N-1} \bar{\boldsymbol{\Omega}}_n \mathbf{R}_n \mathbf{e}_n^T \bar{\mathbf{F}}_N. \tag{6.37}$$

6.5.3 Data Estimator - Estimated CSI

To calculate the ECM with estimated CSI, the input-output ratio must be derived using the discrete LTV channel (6.15) instead of (5.6). The ECM of the n-th OTFS symbol of size $M' \times M$ yields (see A.4 for full derivation)

$$\tilde{\bar{\mathbf{H}}}_n[p,q] = \frac{\alpha}{M'} \sum_{l=0}^{M_s-1} \bar{\mathbf{G}}[l,q] \sum_{k_{\tilde{\tau}}=0}^{M_{gi}/2-1} \sum_{k_\nu=0}^{N-1} \tilde{\bar{\mathbf{h}}}[k_{\tilde{\tau}}, k_\nu] e^{-j2\pi \frac{pk_{\tilde{\tau}}}{M'}}$$

$$\times e^{j2\pi \frac{\mathcal{V}[k_\nu]n}{n_\nu N}} e^{j2\pi \frac{\mathcal{V}[k_\nu]k_{\tilde{\tau}}}{n_\nu N M'}} \sum_{k=0}^{M'-M_{gi}-1} e^{j2\pi \frac{k}{M'}\left(\mathcal{M}_s[l]-p+\frac{\mathcal{V}[k_\nu]}{n_\nu N}\right)}. \tag{6.38}$$

The FT domain data estimation and the SFT are performed by (6.36) and (6.37), respectively, where the ECM for perfect CSI is replaced by (6.38). Fig. 6.6 illustrates the receiver processing of UW-OTFS, including the UW subtraction section.

6.6 Computational Complexity Analysis

This section provides a computational complexity and memory requirement analysis of the proposed UW-OTFS data estimator and that of the UW part to be subtracted on the receiver. Even though it strongly depends on the choice of hardware
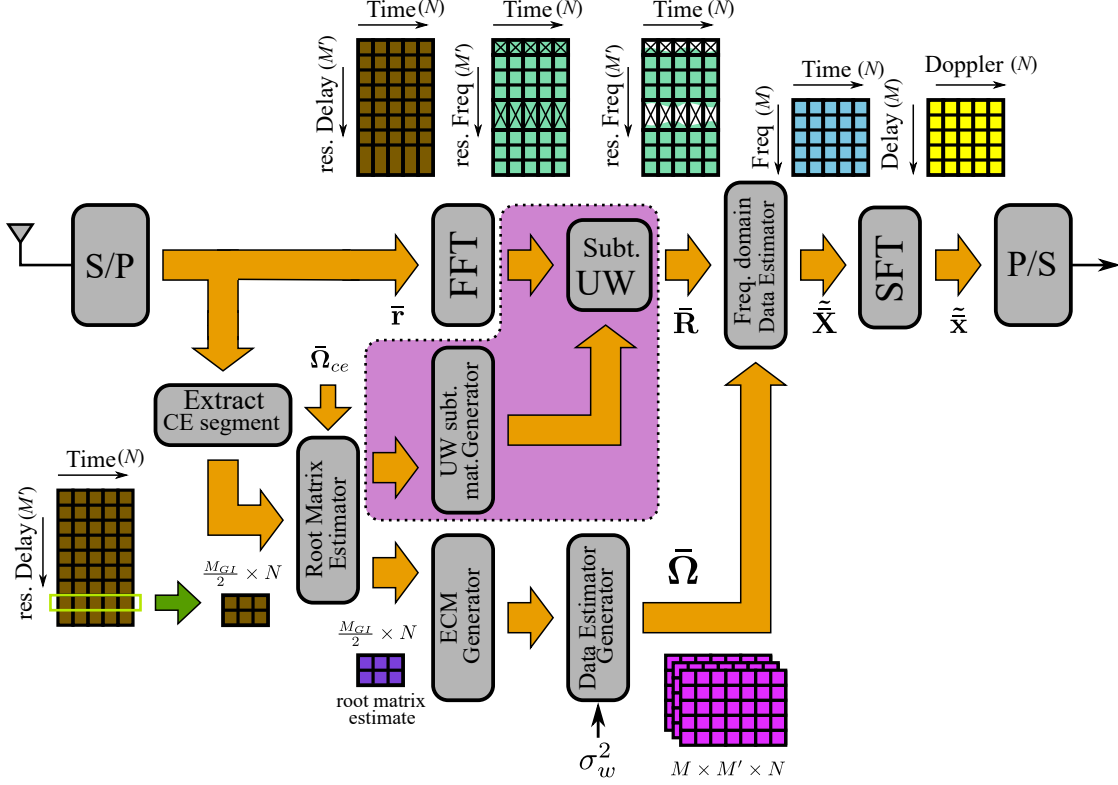
Fig. 6.6: UW-OTFS receiver block schematic with the optional UW subtraction section highlighted.

and software implementation, one way to analyze the computational complexity is to count the number of *Complex Multiplication Equivalent* (CME) units (as it was done in [62]) together with the number of pre-allocated memory entries. One complex division is counted as a single CME and complex additions are ignored in the analysis.

6.6.1   Data Estimator ECM Complexity

As it was stated in Section 6.4, all of the CSI is concentrated within the estimated root matrix $\tilde{\bar{\mathbf{h}}}$. Therefore, (6.38) can also be viewed as

$$\tilde{\bar{\mathbf{H}}}_n[p,q] = \sum_{k_{\tilde{\tau}}=0}^{M_{gi}/2-1} \sum_{k_\nu=0}^{N-1} \bar{\mathbf{h}}[k_{\tilde{\tau}}, k_\nu] \bar{\bar{\mathbf{A}}}_d[p,q,k_{\tilde{\tau}}, k_\nu, n], \tag{6.39}$$

where $\bar{\bar{\mathbf{A}}}_d$ is a pre-calculated $M' \times M \times M_{gi}/2 \times N \times N$ tensor, defined as

$$\bar{\bar{\mathbf{A}}}_d[p,q,k_{\tilde{\tau}},k_\nu,n] = \frac{\alpha}{M'} e^{-j2\pi \frac{pk_{\tilde{\tau}}}{M'}} e^{j2\pi \frac{\mathcal{V}[k_\nu]k_{\tilde{\tau}}}{n_\nu N M'}} e^{j2\pi \frac{\mathcal{V}[k_\nu]n}{n_\nu N}} \sum_{l=0}^{M_s-1} \bar{\mathbf{G}}[l,q]$$

$$\times \sum_{k=0}^{M'-M_{gi}-1} e^{j2\pi \frac{k}{M'}\left(\mathcal{M}_s[l]-p+\frac{\mathcal{V}[k_\nu]}{n_\nu N}\right)}. \tag{6.40}$$

For storing this tensor, $MM'M_{gi}N^2/2$ memory entries need to be allocated and $MM'M_{gi}N^2/2$ CME units would be needed for calculating $\tilde{\bar{\mathbf{H}}}_n$. Given the current system's numerology ($M' = 64$, $N = 16$, $M = 36$, $M_{gi} = 16$), and a 16-bit fixed-point arithmetics, this would be 9.4 MB of memory and 4718592 CME units. Both complexity and memory requirements can be improved by introducing the following modification. We begin by computing

$$\bar{\mathbf{M}}[p, k_\nu] = \sum_{k_{\tilde{\tau}}=0}^{M_{gi}/2-1} \bar{\bar{\mathbf{M}}}[p, k_{\tilde{\tau}}, k_\nu]\tilde{\bar{\mathbf{h}}}[k_{\tilde{\tau}}, k_\nu], \qquad (6.41)$$

which is executed only once in each OTFS transmission. Here, $\bar{\bar{\mathbf{M}}}$ is a tensor of size $M' \times M_{gi}/2 \times N$ which can be pre-calculated according to

$$\bar{\bar{\mathbf{M}}}[p, k_{\tilde{\tau}}, k_\nu] = e^{-j2\pi \frac{pk_{\tilde{\tau}}}{M'}} e^{j2\pi \frac{\mathcal{V}[k_\nu]k_{\tilde{\tau}}}{n_\nu NM'}}.$$

The n-th ECM is then calculated by

$$\tilde{\bar{\mathbf{H}}}_n[p, q] = \sum_{k_\nu=0}^{N-1} \bar{\bar{\mathbf{G}}}[p, q, k_\nu]\bar{\mathbf{N}}[n, k_\nu]\bar{\mathbf{M}}[p, k_\nu], \qquad (6.42)$$

where the remaining pre-calculated tensors are

$$\bar{\bar{\mathbf{G}}}[p, q, k_\nu] = \frac{\alpha}{M'} \sum_{l=0}^{M_s-1} \bar{\mathbf{G}}[l, q] \sum_{k=0}^{M'-M_{gi}-1} e^{j2\pi \frac{k}{M'}\left(\mathcal{M}_s[l]-p+\frac{\mathcal{V}[k_\nu]}{n_\nu N}\right)}, \qquad (6.43)$$

of size $M' \times M \times N$ and

$$\bar{\mathbf{N}}[n, k_\nu] = e^{j2\pi \frac{\mathcal{V}[k_\nu]n}{n_\nu N}}, \qquad (6.44)$$

of size $N \times N$. The memory requirement after this modification is $N^2 + M'MN + M'M_{gi}N/2$ which equals 90.6 kB. As for the CME count:

- (6.41) requires $M'NM_{gi}/2$ CME units
- (6.42) requires $2M'MN^2$ CME units.

Added together, $M'N(M_{gi}/2 + 2MN) = 1187840$ CME units are needed for the modified algorithm. Therefore, the CME count is reduced to 1/4 of the original, and the memory space drops to 1/100.

6.6.2 UW Subtraction Complexity

The UW subtraction matrix defined in Section 6.5.1 is calculated as a product of the estimated root matrix $\tilde{\bar{\mathbf{h}}}$ and a pre-calculated tensor $\bar{\bar{\mathbf{A}}}_{uw}$ of size $M' \times N \times M_{gi}/2 \times N$, defined in (6.33). The number of memory entries required to store the tensor is $M'N^2M_{gi}/2$, which equals 262144 Bytes considering our system numerology. The CME count is also equal to $M'N^2M_{gi}/2$ which is evaluated as 131072 units. Unfortunately, there is no way (to the best of my knowledge) to simplify the calculation

of (6.32) as it was done for the ECM in Section 6.6.1. Therefore, the memory space required to store $\bar{\bar{\mathbf{A}}}_{uw}$ for the given system numerology is approximately 2.9 higher than the memory space to store the tensors required for calculating $\tilde{\bar{\mathbf{H}}}_n$ in (6.42).

6.7 DSF Analysis

DSF is an important parameter to the UW-OTFS receiver, as it allows resizing of the receiver Doppler grid $\mathcal{V}$ according to the maximum Doppler spread ν_m. It differs from the conventional GCE-BEM resolution factor [71] by being a positive-real constant, rather than just positive integer. This section contains a detailed analysis of its influence on the NMSE of the ECM, which is defined as

$$J = \frac{1}{N} \sum_{n=0}^{N-1} \frac{\left(\tilde{\mathbf{H}}_n - \mathbf{H}_n\right)^H \left(\tilde{\mathbf{H}}_n - \mathbf{H}_n\right)}{\mathbf{H}_n^H \mathbf{H}_n}. \tag{6.45}$$

Here, $\mathbf{H}_n$ and $\tilde{\mathbf{H}}_n$ are the vectorized ECMs for the perfect and estimated CSI, respectively, defined as $\mathbf{H}_n = \text{vect}\{\bar{\mathbf{H}}_n\}$ and $\tilde{\mathbf{H}}_n = \text{vect}\{\tilde{\bar{\mathbf{H}}}_n\}$.

6.7.1 Simplified Case ECM Derivation

It is obvious from the location of n_ν in (6.15), that its effect is exactly related to the Doppler domain. Therefore, to isolate its functionality from other phenomenons, the following simplifications are introduced:
- A single tap channel is used ($N_t = 1$),
- the channel gain is $h_0 = 1$,
- zero resampled delay is assumed, i.e., $\mathbf{k}_{\tilde{\tau}}[i] = 0$
- the normalized Doppler frequency of the tap is defined as $\xi = \nu/\Delta\nu$,
- the Dirac impulse UW sequence is used, i.e., $\bar{\mathbf{c}}[p, q] = \sqrt{M'}\delta(p - k_x) \quad \forall \quad p \in \{0, 1, \ldots M' - 1\}$, where $k_x = M' - M_{gi}/2$,
- the AWGN term in (6.25) is neglected,
- in (6.45), only the case for $n = 0$ is used for simplicity, therefore we simplify the NMSE definition into

$$J_0 = \frac{\left(\tilde{\mathbf{H}}_0 - \mathbf{H}_0\right)^H \left(\tilde{\mathbf{H}}_0 - \mathbf{H}_0\right)}{\mathbf{H}_0^H \mathbf{H}_0}. \tag{6.46}$$

Now, we derive the simplified ECM for the perfect and estimated CSI case. We start with the channel model in (5.6) which is simplified into

$$y(k) = s(k)e^{j2\pi \frac{\xi k}{M'N}}, \tag{6.47}$$

therefore, the perfect CSI ECM definition in (6.34) is now reduced to

$$\bar{\mathbf{H}}_0[p,q] = \alpha \sum_{l=0}^{M_s-1} \bar{\mathbf{G}}\Big[l,q\Big] \sum_{k=0}^{M'-M_{gi}-1} e^{j2\pi \frac{k}{M'}\left(\mathcal{M}_s[l]-p\right)} \mathbf{a}[k], \tag{6.48}$$

where $\mathbf{a} = 1/M'\mathbf{h}_\xi$ and where $\mathbf{h}_\xi$ is an $M'N \times 1$ vector, defined as

$$\mathbf{h}_\xi[k] = e^{j2\pi \frac{\xi k}{M'N}}. \tag{6.49}$$

Next, the estimated CSI ECM is needed. The CE matrix in (6.13) yields

$$\bar{\mathbf{y}}_{ce}[m,n] = \sigma_u \sqrt{M'}\delta(m)e^{j2\pi \xi \frac{M'n+k_x}{M'N}}, \tag{6.50}$$

and the CE tensor in (6.24) is simplified to

$$\bar{\bar{\mathbf{A}}}_{ce}[m,n,k_\tau,k_\nu] = \sigma_u \sqrt{M'}\delta(m-k_\tau)e^{j2\pi \frac{\mathcal{V}[k_\nu]}{n_\nu NM'}\left(k_\tau-k_x+M'n\right)}. \tag{6.51}$$

After reshaping $\bar{\bar{\mathbf{A}}}_{ce}$ into an $M_h \times M_h$ matrix $\bar{\mathbf{A}}_{ce}$ using (6.26), we discover that the matrix inverse in (6.27) can be written as

$$\left(\bar{\mathbf{A}}_{ce}\bar{\mathbf{A}}_{ce}^H + \gamma\mathbf{I}_{M_h}\right)^{-1} = \bar{\mathbf{A}}_{c0}^{-1} \otimes \mathbf{I}_{M_{gi}/2},$$

where $\gamma = \sigma_w^2 M_h$ and where $\otimes$ is the Kronecker product. Therefore, we now analyze the much smaller $N \times N$ matrix $\bar{\mathbf{A}}_{c0}$, which is defined as

$$\bar{\mathbf{A}}_{c0} = \sigma_u^2 M'\bar{\mathbf{D}}\bar{\mathbf{Q}}\bar{\mathbf{D}}^T + \gamma\mathbf{I}_N, \tag{6.52}$$

where the $M'N \times M'N$ matrix $\bar{\mathbf{Q}}$ and the $N \times M'N$ downsampling matrix $\bar{\mathbf{D}}$ are defined as

$$\bar{\mathbf{Q}}[p,q] = \sum_{n=0}^{N-1} e^{j2\pi \mathcal{V}[n]\frac{p-q}{n_\nu NM'}} \text{ and } \bar{\mathbf{D}}[p,q] = \delta(pM' + k_x - q),$$

respectively. Finally, the simplified version of the estimated CSI ECM in (6.38) is given by

$$\tilde{\bar{\mathbf{H}}}_0[p,q] = \alpha \sum_{l=0}^{M_s-1} \bar{\mathbf{G}}[l,q] \sum_{k=0}^{M'-M_{gi}-1} e^{j2\pi \frac{k}{M'}(\mathcal{M}_s[l]-p)} \tilde{\mathbf{a}}[k], \tag{6.53}$$

where the $M'N \times 1$ vector $\tilde{\mathbf{a}}$ is defined as

$$\tilde{\mathbf{a}} = \sigma_u^2 \bar{\mathbf{Q}}\bar{\mathbf{D}}^T \bar{\mathbf{A}}_{c0}^{-1}\bar{\mathbf{D}}\mathbf{h}_\xi. \tag{6.54}$$

We may notice that (6.48) and (6.53) only differ in the presence of vectors $\mathbf{a}$ and $\tilde{\mathbf{a}}$. Therefore, to make it simple, instead of analyzing $\tilde{\mathbf{H}}_0$ and $\mathbf{H}_0$ we will first analyze the difference between $\tilde{\mathbf{a}}$ and $\mathbf{a}$.

6.7.2 Time-Domain Analysis

Because both $\tilde{\mathbf{a}}$ and $\mathbf{a}$ depend on the time domain LTV channel vector $\mathbf{h}_\xi$, we now provide a time domain analysis of the DSF phenomenon. First, we need to visualize the function of $\tilde{\mathbf{a}}$. Since $\bar{\mathbf{A}}_{c0}^{-1}$ cannot be expressed analytically for $n_\nu \neq 1$, we begin with analyzing the case $n_\nu = 1$. Here, (6.54) evolves into

$$\tilde{\mathbf{a}} = \frac{\sigma_u^2 N \sqrt{M'}}{\gamma_0} \bar{\mathbf{P}}_A^T \bar{\mathbf{F}}_{M'N}^* \bar{\mathbf{B}} \bar{\mathbf{F}}_N \bar{\mathbf{P}}_B \bar{\mathbf{D}} \mathbf{h}_\xi, \tag{6.55}$$

where $\gamma_0 = N(\sigma_u^2 M' + \sigma_w^2 M_{gi}/2)$, and where $\bar{\mathbf{F}}_{M'N}^* \bar{\mathbf{B}} \bar{\mathbf{F}}_N$ represents the $M'N \times N$ DFT interpolation matrix. Here, $\bar{\mathbf{P}}_A$ and $\bar{\mathbf{P}}_B$ are the permutation matrices, defined as $\bar{\mathbf{P}}_A[p,q] = \delta\big((p - q + M_{gi}/2)_{M'N}\big)$ for $p, q \in \{0, 1, \ldots M'N - 1\}$ and $\bar{\mathbf{P}}_B[p,q] = \delta\big((p - q + 1)_N\big)$ for $p, q \in \{0, 1, \ldots N - 1\}$, respectively, and $\bar{\mathbf{B}}$ is the zero-padding $M'N \times N$ matrix, defined as

$$\bar{\mathbf{B}} = \begin{pmatrix} \mathbf{I}_{N/2} & \bar{\mathbf{0}}_{N/2} \\ \bar{\mathbf{0}}_{(M'-1)N \times N/2} & \bar{\mathbf{0}}_{(M'-1)N \times N/2} \\ \bar{\mathbf{0}}_{N/2} & \mathbf{I}_{N/2} \end{pmatrix}. \tag{6.56}$$

The DFT interpolation (or sinc interpolation) gives perfect results for $\xi \in \mathcal{V}$ (i.e., for integer Doppler channels), however, it performs much worse for all other frequencies. The following comparison of $\tilde{\mathbf{a}}$ and $\mathbf{a}$ illustrates the importance of the DSF, n_ν. Fig. 6.7 shows the time domain comparison of (6.54) w.r.t. the perfect CSI vector $\mathbf{a}$ and the downsampled input to $\tilde{\mathbf{a}}$, $1/M' \bar{\mathbf{D}} \mathbf{h}_\xi$ for $\xi = 0.5$ and $n_\nu = \{1, 1.1, 2\}$. We can see that already $n_\nu = 1.1$ is a great improvement compared to the DFT interpolation result (i.e., $n_\nu = 1$).

6.7.3 Doppler-Domain Analysis

Some more insight into the DSF phenomenon can be gained from evaluating the NMSE in (6.46) w.r.t. the normalized Doppler frequency $\xi = \nu/\Delta\nu$. This is shown in Fig. 6.8 for various values of n_ν, where we can see that the novel interpolation scheme in (6.54) provides a trade-off between NMSE and the useful range of Doppler frequencies. In other words, there exists an optimal n_ν for a given maximum Doppler spread ν_m, which can be approximated by an empirically found formula

$$n_{\nu_0} \cong \frac{\Delta f}{2\nu_m}. \tag{6.57}$$

Fig. 6.9 shows the dependence of NMSE on E_b/N_0. Since the AWGN variance σ_w^2 is an input parameter of the novel interpolation scheme (see (6.52)) and E_b/N_0 is directly related to σ_w^2 according to
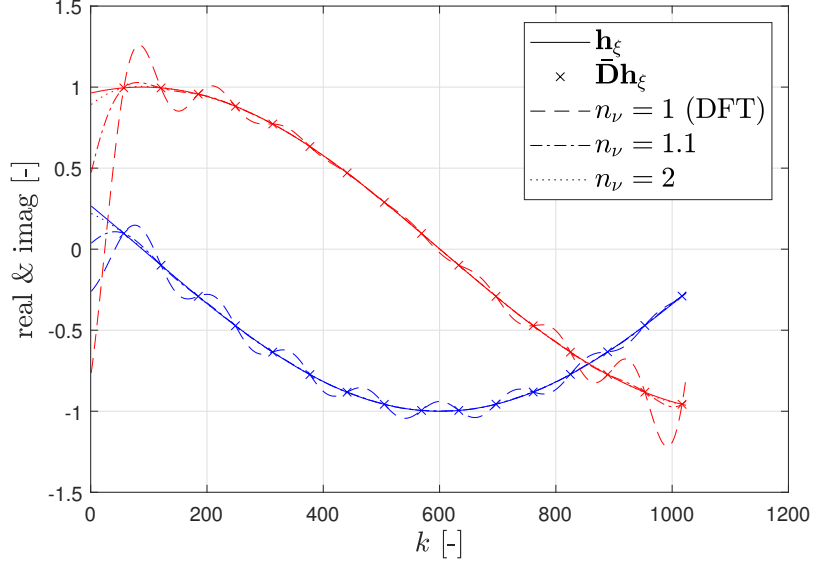
$$E_b/N_0 = \frac{1}{\sigma_w^2} \frac{M'}{Mk_b}, \tag{6.58}$$

Fig. 6.7: Interpolation example for $\xi = 0.5$, where blue and red are the $\Re\{.\}$ and $\Im\{.\}$, respectively ($E_b/N_0 = 40$ dB).

where k_b is the bits-per-symbol ratio of the m-QAM constellation.

We observe in Fig. 6.8 and Fig. 6.9 that the useful Doppler region is proportional in size to $1/n_\nu$, while the NMSE floor within this region is lower bounded by the noise. For instance, the scenario where $n_\nu = 16$ reaches a minimum NMSE of approx. -39 dB for $E_b/N_0 = 40$ dB, and for for $E_b/N_0 = 80$ dB it reaches approx. -78 dB. Therefore, not only is there an optimal n_ν, approximated by (6.57), due to the limited size of the Doppler region (and due to the steep rise of NMSE outside this region), but one must also keep in mind the practical values of E_b/N_0 that become the lower bound of NMSE.
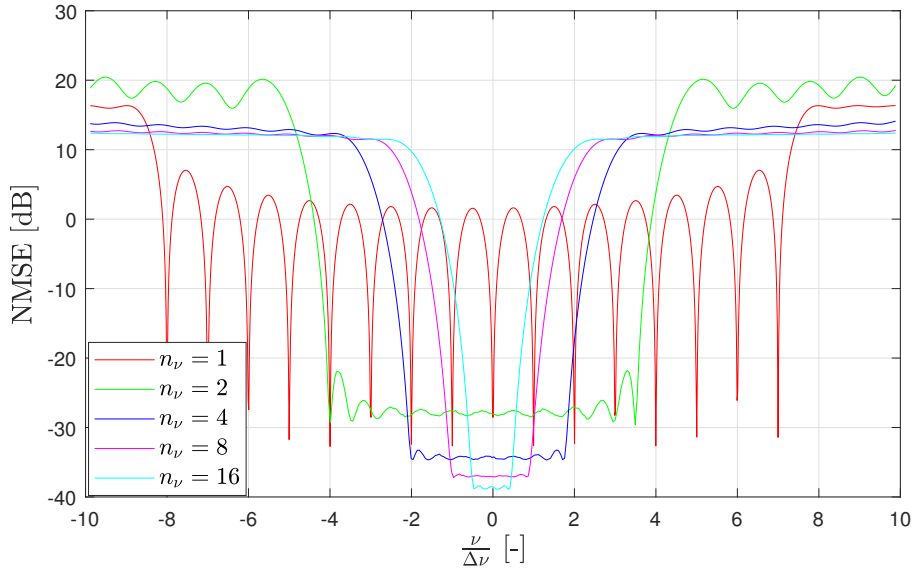
Fig. 6.8: NMSE versus the normalized Doppler frequency for various n_ν ($E_b/N_0 = 40\ dB$).
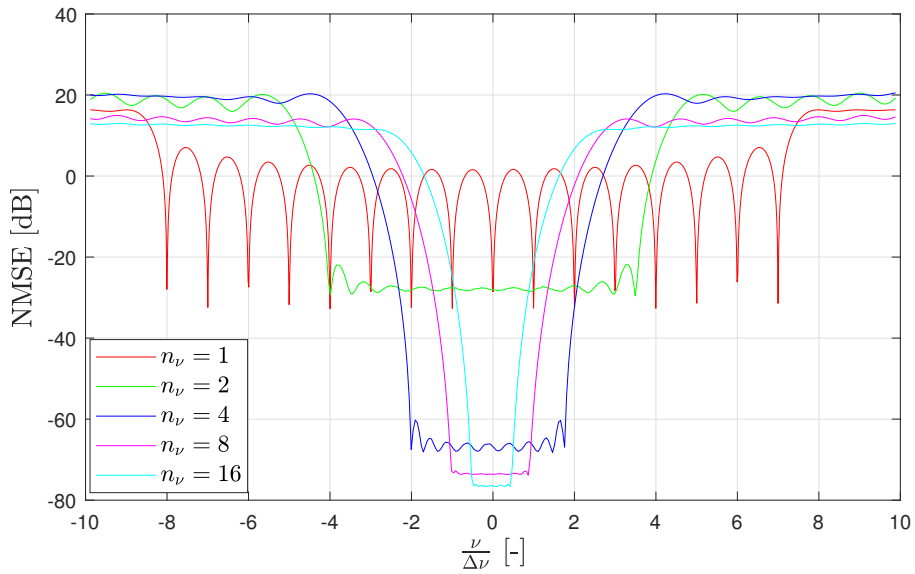

Fig. 6.9: NMSE versus the normalized Doppler frequency for various n_ν ($E_b/N_0 = 80\ dB$).

6.8   Comparison with CP-OTFS

In this section, we present a transmitter model of the OFDM-based OTFS with a guard band (i.e., upsampling) and a pilot embedded in the DD domain, which will be denoted as CP-OTFS. This model will be compared with the proposed UW-OTFS in terms of PAPR and PSD. The concept of CP-OTFS is elaborated further in Appendix A.5, which contains a full-scale derivation of the CE method and a proof, that the guard band is a cause of data interference in the CE.

6.8.1   CP-OTFS Transmitter

The CP-OTFS waveform consists of N OTFS symbols, each M' samples long with an attached CP of length M_{cp}. Note, that the CP length must satisfy

$$M_{\tilde{\tau}} \leq M_{cp}, \tag{6.59}$$

therefore, it is half the size of the UW-OTFS guard interval.

Since there are no redundant subcarriers in CP-OTFS, the number of active subcarriers M_s is set to match the data subcarrier count M in order to have identical bandwidth in both systems, i.e., $(M_s + 1)\Delta f$.

The $M \times N$ DD matrix of m-QAM symbols is denoted $\bar{\mathbf{x}}$. Next, we define the sets of row and column indices of $\bar{\mathbf{x}}$, that limit the rectangular pilot guard region as

$$\mathcal{M}_\tau := \{0, 1, \dots 2M_\tau - 2\}, \tag{6.60}$$

for the delay domain and

$$\mathcal{M}_\nu := \{0, 1, \dots, 2M_\nu - 2\}, \tag{6.61}$$

for the Doppler domain. Here M_τ and M_ν are the expected numbers of channel taps in the the delay and Doppler domain, respectively. Given the fractional relation between the delay and resampled delay domain (due to the guard band) and also the fact that the Doppler frequencies of the channel taps are continuously distributed within $\langle -\nu_m, \nu_m \rangle$, selecting the optimal values of M_τ and M_ν is no trivial task. An optimistic choice from the redundancy point of view is to set $M_\tau = M_{\tilde{\tau}}$ and $M_\nu = 2\lceil \nu_m/\Delta\nu \rceil$, where the Doppler resolution in the CP-OTFS with multiple CPs is

$$\Delta v = \frac{\Delta f M'}{N(M' + M_{cp})}. \tag{6.62}$$

However, as it was shown in [42], for an LTV channel with fractional Doppler, a much wider guard region in the Doppler domain is needed than for an integer Doppler LTV

channel. Therefore, to obtain sufficient CE quality, we must set $M_\nu = N/2 - 1$. The DD matrix is now defined as

$$\bar{\mathbf{x}}[p,q] = \begin{cases} 0 & \forall \quad p \in \mathcal{M}_\tau \cap q \in \mathcal{M}_\nu \\ \rho_0\sqrt{M_0} & \forall \quad p = M_\tau - 1 \ \cap \ q = M_\nu - 1 \\ \text{m-QAM symbols} & \text{otherwise,} \end{cases} \quad (6.63)$$

where $M_0 = (2M_\tau - 1)(2M_\nu - 1)$ and where ρ_0^2 is the pilot energy coefficient. Fig. 6.10 illustrates the CP-OTFS input data matrix with the embedded pilot for $M_\tau = 8$ and $M_\nu = 5$.
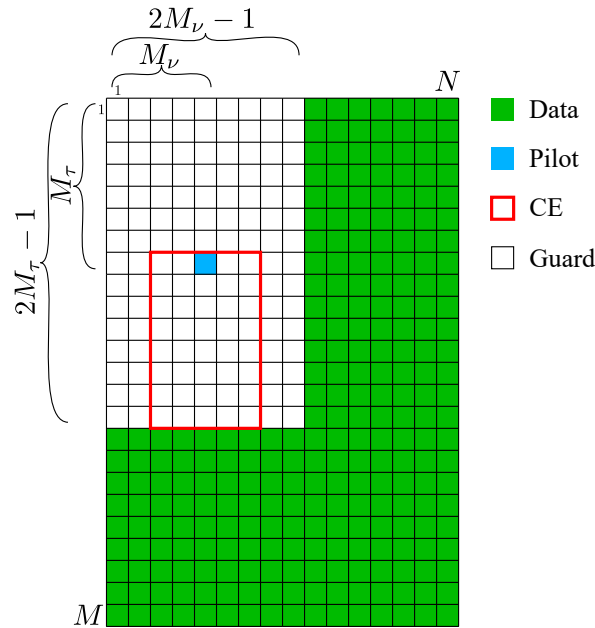

Fig. 6.10: CP-OTFS $M \times N$ input data matrix with the embedded pilot.

The DD matrix is then transformed into the FT domain $\bar{\mathbf{X}} = \bar{\mathbf{F}}_M \bar{\mathbf{x}} \bar{\mathbf{F}}_N^*$, the guard band is added and the Heisenberg transform is performed by IDFT, producing the TX waveform

$$s(k) = \sum_{n=0}^{N-1} \sum_{m=0}^{M_s-1} \bar{\mathbf{X}}[m,n] g_{tx}(k - nM_x') e^{j2\pi \frac{\mathcal{M}_s[m](k-nM_{cp})}{M'}}, \quad (6.64)$$

where $M_x' = M' + M_{cp}$, $\mathcal{M}_s$ is defined in (6.4) and where the TX windowing function for the CP-OTFS is defined as

$$g_{tx}(k) = \begin{cases} \frac{1}{\sqrt{M_s}} & \forall \quad k \in \langle -M_{cp}, M' - 1 \rangle \\ \\ 0 & \text{otherwise.} \end{cases} \quad (6.65)$$

6.8.2 Spectral Efficiency Comparison

While in UW-OTFS, only the guard interval M_{gi} dependent on the maximum delay $M_{\tilde{\tau}}$ according to the condition $M_{gi} \geq 2M_{\tilde{\tau}}$ defined in (5.8), in CP-OTFS, both the delay and Doppler dimensions of the guard region $(2M_\tau - 1) \times (2M_\nu - 1)$ are dependent on the LTV channel parameters. Therefore, even though we compare the TX waveforms, we must also specify the LTV channel parameters to ensure a fair comparison. The parameters common for both systems are:

- subc. spacing $\Delta f = 15\ kHz$, IFFT size $M' = 64$, num. of OTFS symbols $N = 16$, num. of active subcarriers $M_s = 52$,
- carrier frequency $f_0 = 5$ GHz, max. velocity 400 kmph,
- max. number of delay taps $M_{\tilde{\tau}} = 8$.

The derived parameters common for both systems are:

- sampling frequency $F = \Delta f M' = 960$ kHz,
- approx. bandwidth $BW \cong (M_s + 1)\Delta f = 795$ kHz,
- max. Doppler spread $\nu_m = 1853$ Hz, according to (5.7),
- max. delay $M_{\tilde{\tau}}/F = 8.333\ \mu$s.

It is a common practice to set the embedded pilot energy equal to the sum of energy of the symbols taken by the guard region, i.e., $\rho_0^2 \sim 1$ [44, 45, 65]. The source [42] further advises to set $\rho_0^2 \geq 1$ if 16QAM constellation is used. Therefore, we chose $\rho_0^2 = 1.2$ for this comparison. The mean UW energy in UW-OTFS was set to $\sigma_u^2 = 0.2$ as it is an empirically found optimum in terms of BER for $N_t = 4$ (see Fig. 6.11).

TABLE. 6.1 then numerically compares both systems in terms of total TX duration T_{tx}, number of data symbols per transmission M_d (i.e., $M_d = MN$ in UW-OTFS and $M_d = MN - M_0$ in the CP-OTFS), the symbol rate $R_s = M_d/T_{tx}$ and the upper bound of the spectral efficiency $\eta = k_b R_s/BW$, where $k_b = 4$ is the bit-per-symbol ratio for 16QAM.

Fig. 6.13 provides a comparison in terms of the TX waveform energy. After performing 4000 transmissions, the solid line represents the mean energy in each bin of the OTFS symbol, while the dashed lines represent the first (D1) and the last (D9) decile of the statistical distribution in each bin. This way, the deterministic parts of the waveforms can be distinguished from the random ones. In Fig. 6.12, the waveforms are compared in terms of PAPR χ.

Lastly, in Fig. 6.14 we can see the average PSD comparison of both waveforms (i.e., average from 4000 transmissions). It is clearly visible, that the superb OOB emissions of UW-OFDM have been preserved in UW-OTFS. Meanwhile, the CP-OTFS exhibits not only very poor OOB emissions but also countless spikes due to the embedded pilot's presence.
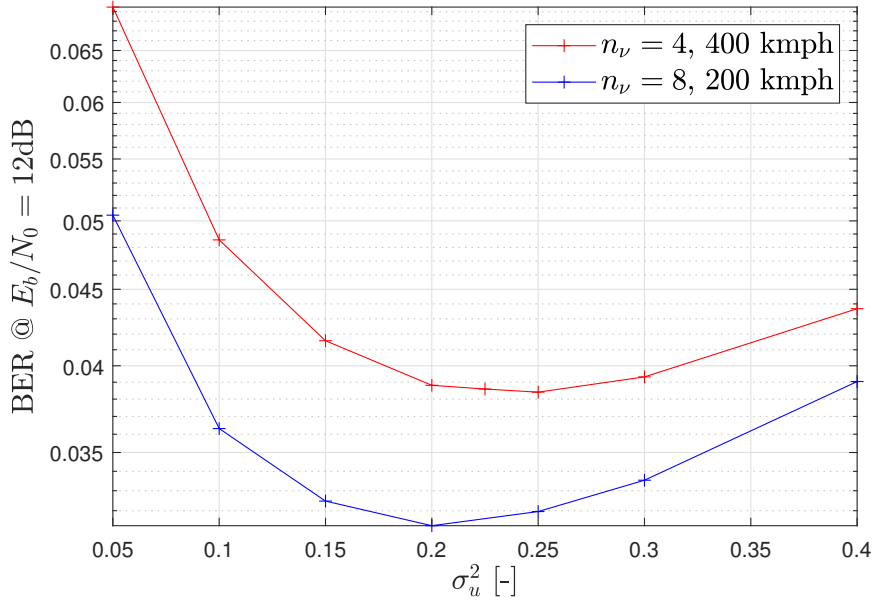
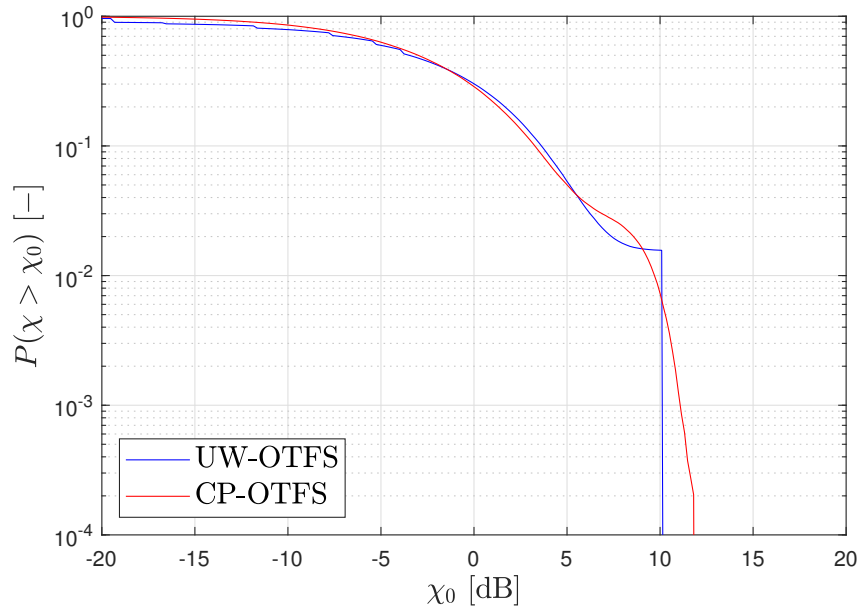Fig. 6.11: The search for optimal σ_u^2 in two LTV channel settings with $N_t = 4$.

Fig. 6.12: PAPR comparison of UW-OTFS and CP-OTFS in the presence of pilots.

6.8.3 Transmitter Complexity Comparison

The transmitter structures of both systems are very similar, as we can see if displayed in a matrix notation as

$$\bar{\mathbf{s}}_{uw} = \bar{\mathbf{F}}_{M'}^* \bar{\mathbf{B}} \bar{\mathbf{G}} \bar{\mathbf{F}}_M \bar{\mathbf{x}} \bar{\mathbf{F}}_N^*, \qquad (6.66)$$

Tab. 6.1: UW-OTFS and CP-OTFS Parameters

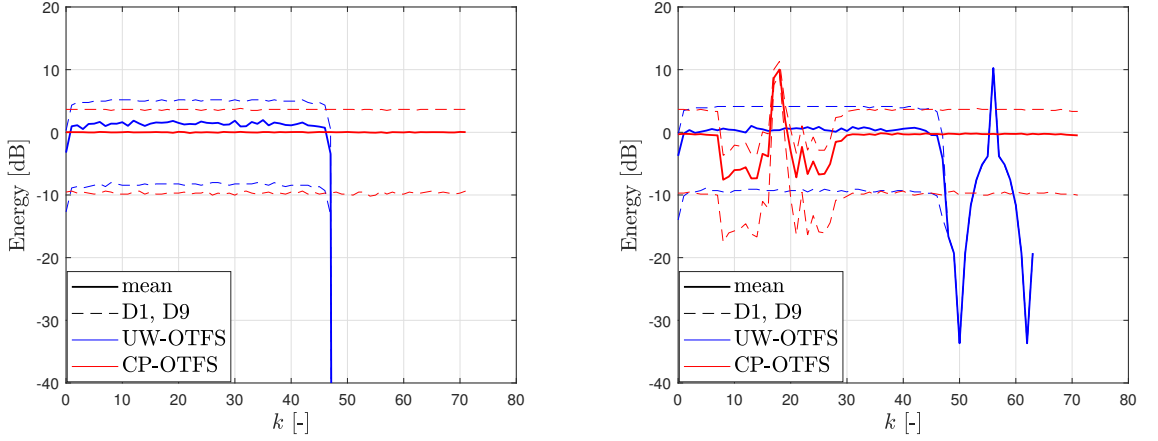| System	Δv	T_{tx}	M_d	R_s	η
-	Hz	ms	-	kBd	$bit/s/Hz$
UW-OTFS	937.5	1.066	832	540	2.717
CP-OTFS	833.3	1.200	611	509.2	2.562

Fig. 6.13: Statistical energy profile of a single OTFS symbol for UW-OTFS and CP-OTFS in the absence (left) and presence (right) of pilots.
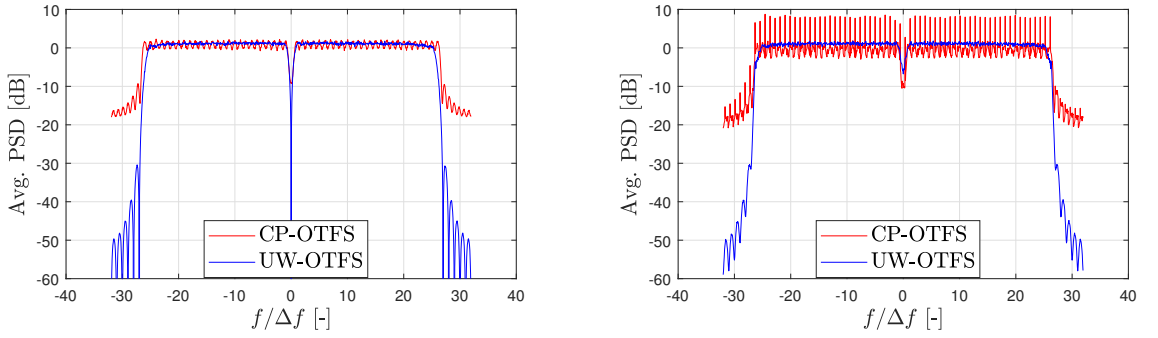

Fig. 6.14: Average PSD of UW-OTFS and CP-OTFS in the absence (left) and presence (right) of pilots.

for UW-OTFS, and

$$\bar{\mathbf{s}}_{cp} = \bar{\mathbf{F}}_{M'}^* \bar{\mathbf{B}} \bar{\mathbf{F}}_{M_s} \bar{\mathbf{x}} \bar{\mathbf{F}}_N^*, \tag{6.67}$$

for CP-OTFS, where $\bar{\mathbf{B}}$ is the guard band insertion matrix. In fact, the only difference is the presence of the UW precoding matrix $\bar{\mathbf{G}}$ in UW-OTFS.

The only way the computational complexity can be minimized is to use FFT for as many operations as possible. Due to the presence of the guard band, it is

very unlikely that an FFT algorithm will be used for $\bar{\mathbf{F}}_M$ as well as for $\bar{\mathbf{F}}_{M'}^*$. Since $M' > M$, and also $M' > M_s$, it is more beneficial to use the FFT for performing $\bar{\mathbf{F}}_{M'}^*$, and possibly utilize another FFT algorithm also for $\bar{\mathbf{F}}_N^*$ (therefore both M' and N must be powers of two). Now, since the product $\bar{\mathbf{G}}\bar{\mathbf{F}}_M$ can be pre-calculated and stored as a single matrix of size $M_s \times M$, e.g., $\check{\bar{\mathbf{F}}}_M = \bar{\mathbf{G}}\bar{\mathbf{F}}_M$, it turns out, that the computational complexity of the CP-OTFS transmitter is actually higher than that of UW-OTFS, because $M_s = M + M_r$ and $M_r = M_{gi}$. In other words, to compute $\bar{\mathbf{F}}_{M_s}\bar{\mathbf{x}}$ in CP-OTFS we need $M_s^2 N$ CME units [62], whereas to compute $\check{\bar{\mathbf{F}}}_M\bar{\mathbf{x}}$ in UW-OTFS, we need only $M_s M N$ CME units.

6.9 Numerical Simulations

The numerical simulations were done using a 16QAM constellation without any forward error code and the LTV channel model in (5.6) was used with different numbers of sparse channel taps, N_t. The maximum delay was fixed at $M_{\tilde{\tau}} = 7$ and the maximum velocity was $= \{200, 400\}$ km/h, which corresponds to the maximum Doppler spreads $\nu_m = \{926.5, 1853.1\}$ Hz. The UW-OTFS numerology is: $\Delta f = 15$ kHz, $M' = 64$, $M_s = 52$, $M_r = M_{gi} = 16$, $M = 36$ and $N = 16$. The E_b/N_0 is related to the AWGN variance σ_w^2 according to (6.58) In total, 2000 random channel realizations were used for each simulation. Unless otherwise noted, the simulations were done without subtracting the UW sequence on the RX side.

6.9.1 DSF Influence

In Fig. 6.15 we can see average BER vs E_b/N_0 characteristics for different values of n_ν, all for the same set of 2000 LTV channel realizations (400 km/h, $M_{\tilde{\tau}} = 7$). It is clear, that a proper choice of DSF is crucial. If n_ν is too small, the interpolation in (6.54) still prevails much of the DFT interpolation character. If n_ν exceeds the optimum for a given ν_m (in this case it is approx. $n_\nu = 3.75$), the Doppler frequency components of the channel no longer occupy the low NMSE region visible in Fig. 6.8 and this causes BER to increase. The $\delta(.)$ symbol in the legend in Fig. 6.15 means that the Dirac impulse UW sequence, defined in (6.10), were used.

In Fig. 6.16 we can see the NMSE representation of the BER analysis in Fig. 6.15. More precisely, the NMSE was calculated with (6.45) for the same set of 2000 random channel realizations as in Fig. 6.15. It is clear that the NMSE analysis reflects the behavior of the simplified case in Fig. 6.8 if a mean NMSE over $\langle -\nu_m, \nu_m \rangle$ was calculated for a given n_ν. Also, we can see from the $\delta(.)$ curves that the cost for having the superb OOB emissions is approx. 1.5 dB in terms of E_b/N_0.

6.9.2 UW Subtraction Influence

This section contains a numerical MSE analysis of UW-OTFS with and without the UW subtraction on the RX side. The top of Fig. 6.17 contains five MSE curves, each for a different system setting:

- estimated CSI ECM in (6.38) without UW subtraction
- perfect CSI ECM in (6.34) without UW subtraction
- estimated CSI ECM in (6.38), estimated UW in (6.32) was subtracted
- estimated CSI ECM in (6.38), perfect UW in (6.31) was subtracted
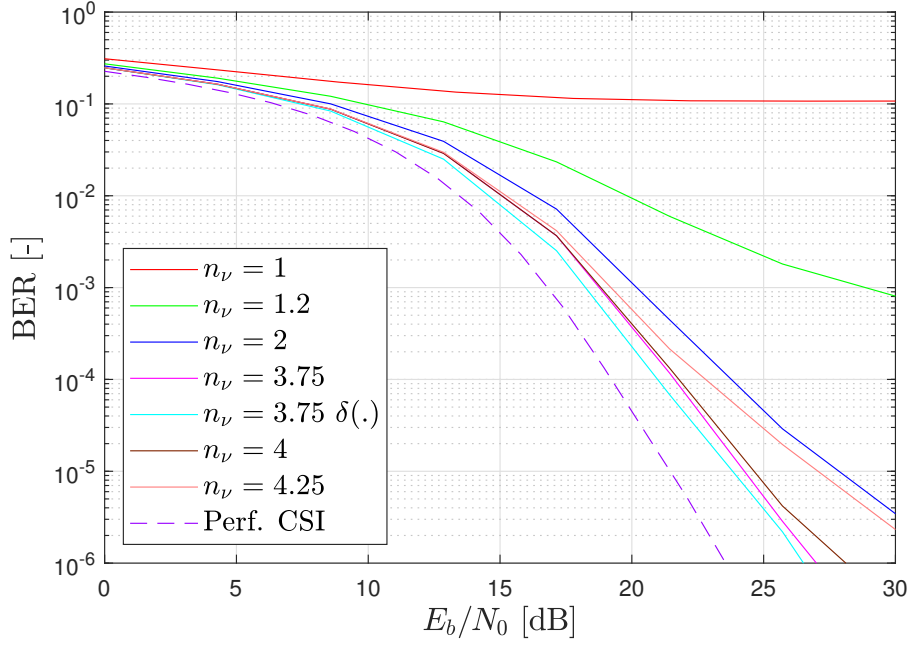- perfect CSI ECM in (6.34), perfect UWin (6.31) was subtracted.

93

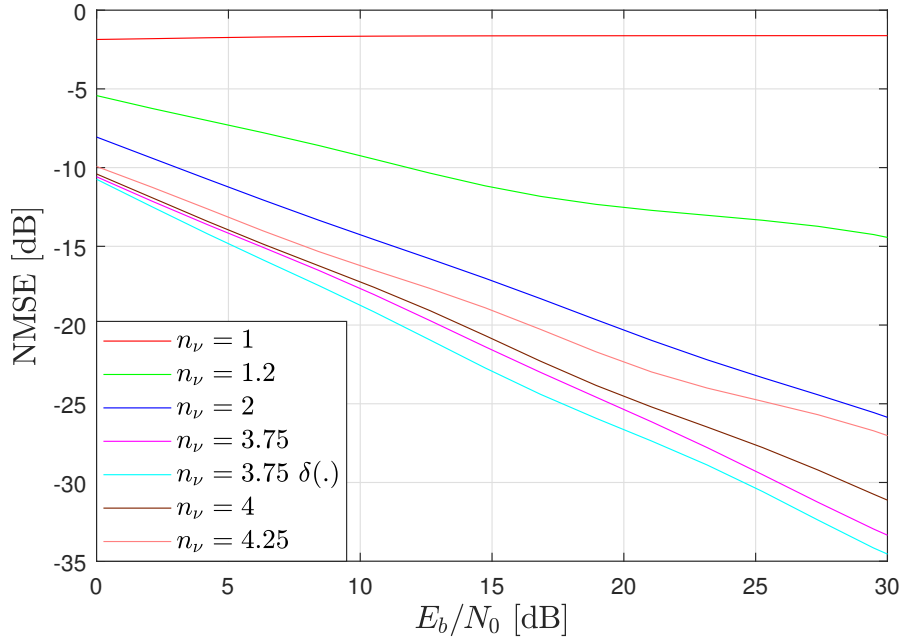Fig. 6.15: Avg. BER vs. E_b/N_0 for 400 km/h, $N_t = 4$ with various n_ν.

Fig. 6.16: Avg. NMSE vs E_b/N_0 for 400 km/h, $N_t = 4$ with various n_ν.

The LTV channel has $N_t = 4$, a maximum velocity 200 km/h and in the estimated CSI cases, the DSF was set to the optimal value 7.75. All five simulations were performed in the same recording of 2000 random channel realizations. The UW se-

quence designed in Section 6.3 was used where $\sigma_u^2 = 0.2$ according to the empirically found optimum in Fig. 6.11. The MSE is defined as

$$\text{MSE} = \frac{1}{MN} \sum_{m=0}^{M-1} \sum_{n=0}^{N-1} \text{E}\left\{ |\tilde{\bar{\mathbf{x}}}[m,n] - \bar{\mathbf{x}}[m,n]|^2 \right\} \tag{6.68}$$

where $\tilde{\bar{\mathbf{x}}}$ is the estimated DD domain symbol matrix (6.37). The results show that by subtracting the UW we may reduce the MSE floor by approximately 6 dB. However, such a benefit would remain unnoticed in moderate-order m-QAM constellations, such as the 16-QAM (see the bottom of Fig. 6.17). Also, UW subtraction comes at the cost of additional rise in computational complexity.

6.9.3 Various Channel Scenarios

In Fig. 6.18 we can see the avg. BER of UW-OTFS in various scenarios of the 400 km/h channel ($\sigma_u^2 = 0.2$ unless otherwise noted), without subtracting the UW. The estimated CSI case (solid lines; DSF set to 3.75 according to (6.57)) is compared to perfect CSI (solid lines with a + symbol) and also to the AWGN channel (dashed and dotted line correspond to situations with and without the UW sequence, respectively). The $N_t = 1$ scenario offers the best performance since the perfect CSI case matches the AWGN followed by the estimated CSI with approx. 2.5 dB loss. For $N_t > 1$ we witness a sudden loss in $Eb/N0$, caused by the *Inter-Carrier Interference* (ICI). After further increasing the N_t, we may observe the DD domain-induced diversity gain, which is manifested by an increased slope of BER in higher $Eb/N0$ regions.
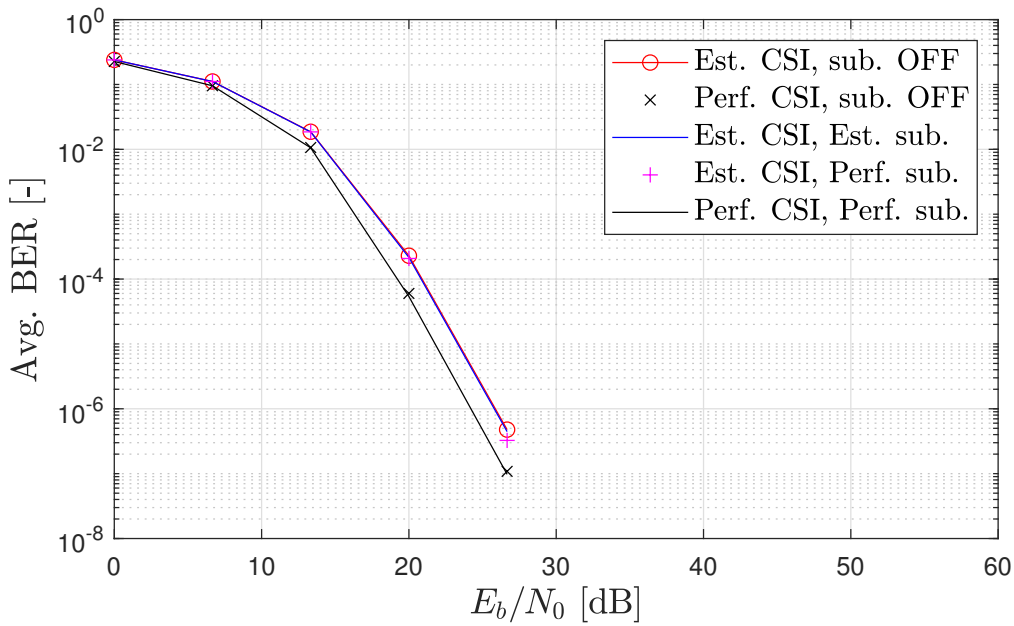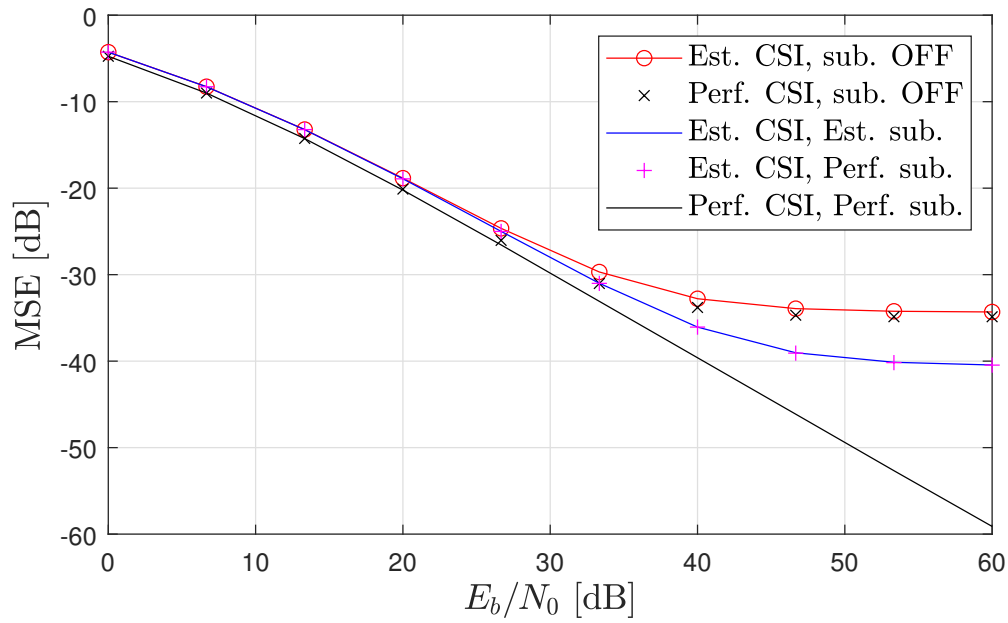
Fig. 6.17: MSE (top) and Avg. BER (bottom) vs E_b/N_0 analysis of the UW subtraction influence for 200 km/h, $N_t = 4$ and $n_\nu = 7.75$, using a 16-QAM constellation.
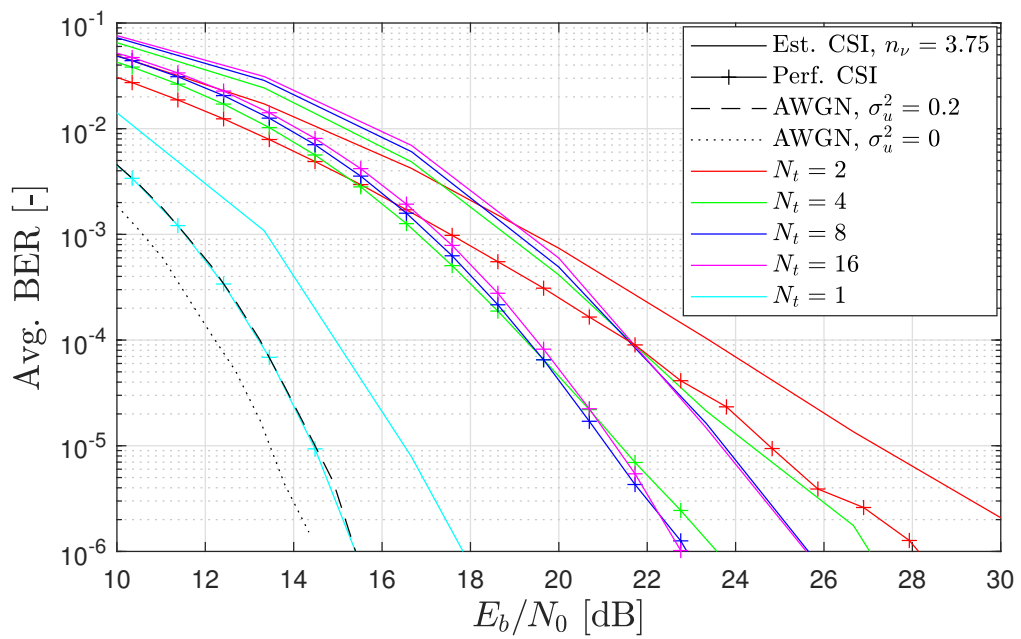
Fig. 6.18: Avg. BER vs E_b/N_0 in a 400 km/h channel with $N_t = \{1, 2, 4, 8, 16\}$.

Conclusions to the Second Part

In the second part of the thesis, a new type of OFDM-based OTFS was presented, which uses the UW-OFDM (with a guard band in the frequency domain) as an outer processing block. The proposed UW-OTFS uses the typical WLAN-style subcarrier mapping with a suppressed DC component for its symmetrical PSD, which is necessary for a successful optimization of the UW precoding matrix [63]. In the next step, an example of the UW sequence was proposed which is transmitted in superposition with the data waveform and which is designed to keep the OOB emissions low (as it is typical for the UW-OFDM) and simultaneously, to offer a sufficient CE quality. Both parameters were compared with an alternative UW sequence, i.e., the sequence of discrete Dirac impulses, which proved to be slightly better in CE quality (see Fig. 6.16) but much worse in terms of the OOB emissions (Fig. 6.3).

The proposed CE approach is different from the conventional embedded pilot CE in two aspects:

1. it is located at the receiver input, and therefore, it provides the channel estimate prior to any further data signal processing. For instance, the conventional embedded pilot CE requires passing the received waveform all the way to the DD domain, where the CSI can be estimated.
2. it is somehow similar to the GCE-BEM and it implements the DSF, which can be viewed as an analogy to the BEM resolution factor, except that the DSF can be (and it is intended to be) a positive real value and not just a positive integer, as in the case of GCE-BEM.

The DSF allows us to tune the receiver based on the expected maximum Doppler spread ν_m (see Formula (6.57) for the optimal DSF), so that we can get the most of the fractional-Doppler channel, i.e., minimize the BER, as shown in Fig 6.15. The exact mechanism of the DSF phenomenon was theoretically analyzed in a simplified scenario in Section 6.7 and it shows resemblance to the DFT or sinc interpolation, especially as the DSF approaches unity. Also, the complexity of our CE method is not dependent on the sparsity of the LTV channel, neither the method requires a prior knowledge of the number of channel taps N_t, which is not the case for the popular iterative methods, such as the message passing [41].

Section 6.5.1 introduced a dilemma of whether the UW should be subtracted before the data estimation on the receiver, or not. The reason to do so was found by a numerical MSE simulation with the results shown in Fig. 6.17, where the subtraction of the UW causes the MSE floor to drop by approximately 6 dB, which would be visible in the BER simulations in case of higher modulation formats. On the other hand, a strong argument not to subtract the UW relates to the associated

increase in computational complexity. According to the analysis in Section 6.6.2, UW subtraction requires almost three times the amount of memory space required for the ECM calculation, that is used for data estimation.

The data is estimated in the FT domain one OTFS symbol after another, using the LMMSE estimator with a matrix inversion of size $M \times M$, which is another advantage of the UW-OTFS compared to the conventional single-CP OTFS, which uses either a full matrix inversion of size $MN \times MN$ or the message passing algorithm.

Unable to find any OTFS publication that would take into account the system's OOB emissions i.e., implement the frequency domain guard band, and at the same time provide a complete system design with the CE, the only option left was to try to design it by ourselves.

Section 6.8 contains experimental design of the CP-OTFS, which shares many similarities to the proposed UW-OTFS, such as the guard band, the presence of GI in each OTFS symbol and therefore also the FT domain data estimation and also the utilization of the DSF. The standard embedded pilot method was used, and the CE was done by extracting the pilot surroundings in the DD domain. However, as it was elaborated in Appendix A.5, the guard band's presence (and also the fractional-Doppler channel) causes severe damage to the CE because the data interfere with the pilot, regardless of the guard region surrounding the pilot in the DD domain. Because of this interference, we were unable to construct an appropriate data estimator for the CP-OTFS and therefore, it could not be compared with the proposed UW-OTFS in terms of BER. Instead, their transmit waveforms were compared, set for (almost) the same system numerology. The results show that the UW-OTFS matches the CP-OTFS in PAPR (Fig. 6.12), outperforms it in OOB emissions (Fig. 6.14) and also in terms of the TX computational complexity.

An interesting future research topics would be to experiment with other variants of BEM for the CE, to optimize the UW sequence for lower PAPR and also to research the synchronization capabilities of the UW-OTFS.

List of appendices

A Appendices

A.1 UW on the Receiver - Perfect CSI Knowledge

The n-th UW vector $\mathbf{Y}_{uw,n}$ of size $M' \times 1$ is derived here. We begin by evaluating the FT domain RX matrix (6.29), where $r(k)$ now represents the UW waveform (6.21) after passing through the LTV channel (5.6) without AWGN. This yields

$$\bar{\mathbf{Y}}_{uw}[m,n] = \sigma_u \sum_{i=0}^{N_t-1} \mathbf{h}[i] \sum_{m'=0}^{M'-1} \sum_{n'=0}^{N-1} \bar{\mathbf{C}}[m',n'] \sum_{k=-\infty}^{\infty} e^{j2\pi \frac{m'(k-\mathbf{k}_{\tilde{\tau}}[i])}{M'}}$$

$$\times g_0(k-nM')g_0(k-\mathbf{k}_{\tilde{\tau}}[i]-n'M')e^{-j2\pi \frac{mk}{M'}} e^{j2\pi \frac{\mathbf{v}[i]k}{\Delta f M'}}. \tag{A.1}$$

where $\bar{\mathbf{C}} = \bar{\mathbf{F}}_{M'}\bar{\mathbf{c}}$. In order to obtain a closed-form expression, we must substitute $k' = k - \mathbf{k}_\tau[i] - n'M'$, which yields

$$\bar{\mathbf{Y}}_{uw}[m,n] = \sigma_u \sum_{i=0}^{N_t-1} \mathbf{h}[i] \sum_{n'=0}^{N-1} \sum_{m'=0}^{M'-1} \bar{\mathbf{C}}[m',n'] e^{-j2\pi \frac{m\mathbf{k}_{\tilde{\tau}}[i]}{M'}} e^{j2\pi \frac{\mathbf{v}[i]n'}{\Delta f}}$$

$$\times e^{j2\pi \frac{\mathbf{v}[i]\mathbf{k}_{\tilde{\tau}}[i]}{\Delta f M'}} \left\{ \sum_{k'=-\infty}^{\infty} g_0(k' - (n-n')M' + \mathbf{k}_{\tilde{\tau}}[i]) g_0(k') \right.$$

$$\left. \times e^{j2\pi \frac{k'}{M'}\left(m'-m+\frac{\mathbf{v}[i]}{\Delta f}\right)} \right\}. \tag{A.2}$$

The section in curly brackets will now be analyzed. By considering the definitions of $g_d(.)$ and $g_0(.)$, we can set the summation limits for $k' \in \langle m_1, m_2 \rangle$ in (A.2) as

$$m_1 = \max\left\{0, \; qM' - \mathbf{k}_{\tilde{\tau}}[i]\right\}, \tag{A.3}$$

$$m_2 = \min\left\{0, \; qM' - \mathbf{k}_{\tilde{\tau}}[i]\right\} + M' - 1, \tag{A.4}$$

where $q = n - n'$. A non-zero outcome of the summation is obtained for $q = 0$, (when $m_1 = 0$ and $m_2 = M' - \mathbf{k}_{\tilde{\tau}}[i] - 1$) and for $q = 1$ when $m_1 = M' - \mathbf{k}_{\tilde{\tau}}[i]$ and $m_2 = M' - 1$. Therefore, (A.2) can be simplified into

$$\bar{\mathbf{Y}}_{uw}[m,n] = \frac{\sigma_u}{M'} \sum_{i=0}^{N_t-1} \mathbf{h}[i] e^{-j2\pi \frac{m\mathbf{k}_\tau[i]}{M'}} e^{j2\pi \frac{\mathbf{v}[i]n}{\Delta f}} e^{j2\pi \frac{\mathbf{v}[i]\mathbf{k}_\tau[i]}{\Delta f M'}}$$

$$\times \sum_{m'=0}^{M'-1} \left\{ \bar{\mathbf{C}}[m',n-1] e^{-j2\pi \frac{\mathbf{v}[i]}{\Delta f}} \sum_{k'=M'-\mathbf{k}_\tau[i]}^{M'-1} e^{j2\pi \frac{k'}{M'}\left(m'-m+\frac{\mathbf{v}[i]}{\Delta f}\right)} \right.$$

$$\left. + \bar{\mathbf{C}}[m',n] \sum_{k'=0}^{M'-\mathbf{k}_\tau[i]-1} e^{j2\pi \frac{k'}{M'}\left(m'-m+\frac{\mathbf{v}[i]}{\Delta f}\right)} \right\}, \tag{A.5}$$

where $\bar{\mathbf{C}}[m',-1] = 0$ for all $m' \in \{0,1,\ldots,M'-1\}$.

A.2 UW on the Receiver - Estimated CSI

Our goal here is to derive the n-th UW vector $\tilde{\mathbf{Y}}_{uw,n}$ of size $M' \times 1$ that needs to be subtracted on the RX side. Similarly to Appendix A.1, we begin by evaluating the FT domain RX matrix (6.29), with $r(k)$ being the UW waveform (6.21), only now we propagate it through the discrete LTV channel (6.15) without AWGN. This yields

$$\tilde{\bar{\mathbf{Y}}}_{uw}[m,n] = \sigma_u \sum_{k_{\tilde{\tau}}=0}^{M_{gi}/2-1} \sum_{k_{\nu}=0}^{N-1} \bar{\mathbf{h}}[k_{\tilde{\tau}}, k_{\nu}] \sum_{n'=0}^{N-1} \sum_{m'=0}^{M'-1} \bar{\mathbf{C}}[m',n'] \sum_{k=-\infty}^{\infty} g_0(k-nM')g_0(k-k_{\tilde{\tau}}-n'M')$$

$$\times e^{-j2\pi\frac{mk}{M'}} e^{j2\pi\frac{m'(k-k_{\tilde{\tau}})}{M'}} e^{j2\pi\frac{\mathcal{V}[k_{\nu}]k}{n_{\nu}NM'}}, \tag{A.6}$$

which can be equivalently written as

$$\tilde{\bar{\mathbf{Y}}}_{uw}[m,n] = \sum_{k_{\tilde{\tau}}=0}^{M_{gi}/2-1} \sum_{k_{\nu}=0}^{N-1} \bar{\bar{\mathbf{A}}}_{uw}[m,n,k_{\tilde{\tau}},k_{\nu}]\bar{\mathbf{h}}[k_{\tilde{\tau}},k_{\nu}], \tag{A.7}$$

where after substituting $k' = k - k_{\tilde{\tau}} - n'M'$ we define the $M' \times N \times M_{gi}/2 \times N$ tensor as

$$\bar{\bar{\mathbf{A}}}_{uw}[m,n,k_{\tilde{\tau}},k_{\nu}] = \sigma_u \sum_{n'=0}^{N-1} \sum_{m'=0}^{M'-1} \bar{\mathbf{C}}[m',n']e^{-j2\pi\frac{mk_{\tilde{\tau}}}{M'}} e^{j2\pi\frac{n'\mathcal{V}[k_{\nu}]}{n_{\nu}N}} e^{j2\pi\frac{\mathcal{V}[k_{\nu}]k_{\tilde{\tau}}}{n_{\nu}NM'}}$$

$$\times \left\{ \sum_{k'=-\infty}^{\infty} g_0(k' - (n-n')M' + k_{\tilde{\tau}})g_0(k')e^{j2\pi\frac{k'}{M'}\left(m'-m+\frac{\mathcal{V}[k_{\nu}]}{n_{\nu}N}\right)} \right\}. \tag{A.8}$$

The section in curly brackets is non-zero only if $n' = n - 1$, where it equals

$$\frac{1}{M'} \sum_{k'=M'-k_{\tilde{\tau}}}^{M'-1} e^{j2\pi\frac{k'}{M'}\left(m'-m+\frac{\mathcal{V}[k_{\nu}]}{n_{\nu}N}\right)}, \tag{A.9}$$

and for $n' = n$, which equals

$$\frac{1}{M'} \sum_{k'=0}^{M'-k_{\tilde{\tau}}-1} e^{j2\pi\frac{k'}{M'}\left(m'-m+\frac{\mathcal{V}[k_{\nu}]}{n_{\nu}N}\right)}. \tag{A.10}$$

The tensor (A.8) is now evaluated as

$$\bar{\bar{\mathbf{A}}}_{uw}[m,n,k_{\tilde{\tau}},k_{\nu}] = \frac{\sigma_u}{M'}e^{-j2\pi\frac{mk_{\tilde{\tau}}}{M'}} e^{j2\pi\frac{n\mathcal{V}[k_{\nu}]}{n_{\nu}N}} e^{j2\pi\frac{k_{\tilde{\tau}}\mathcal{V}[k_{\nu}]}{n_{\nu}NM'}}$$

$$\times \sum_{m'=0}^{M'-1} \left\{ \bar{\mathbf{C}}[m',n-1]e^{-j2\pi\frac{\mathcal{V}[k_{\nu}]}{n_{\nu}N}} \sum_{k'=M'-k_{\tilde{\tau}}}^{M'-1} e^{j2\pi\frac{k'}{M'}\left(m'-m+\frac{\mathcal{V}[k_{\nu}]}{n_{\nu}N}\right)} \right.$$

$$\left. +\bar{\mathbf{C}}[m',n] \sum_{k'=0}^{M'-k_{\tilde{\tau}}-1} e^{j2\pi\frac{k'}{M'}\left(m'-m+\frac{\mathcal{V}[k_{\nu}]}{n_{\nu}N}\right)} \right\}, \tag{A.11}$$

where $\bar{\mathbf{C}}[m',-1] = 0$ for all $m' \in \{0, 1, \ldots, M'-1\}$.

A.3 ECM Derivation - Perfect CSI Knowledge

We begin by deriving the input-output ratio in the FT domain. The FT domain RX matrix of the data part of the UW-OTFS waveform is defined in (6.29), where

$$r_d(k) = \sum_{i=0}^{N_t-1} \mathbf{h}[i] s_d(k - \mathbf{k}_{\tilde{\tau}}[i]) e^{j2\pi \mathbf{v}[i]k\Delta T} + w(k), \tag{A.12}$$

and where $s_d(k)$ is defined in (6.6). The matrix $\bar{\mathbf{R}}_d$ can be evaluated using (6.29) as

$$\bar{\mathbf{R}}_d[m,n] = \alpha \sum_{n'=0}^{N-1} \sum_{m'=0}^{M_s-1} \check{\mathbf{X}}[m',n'] \sum_{i=0}^{N_t-1} \mathbf{h}[i] \sum_{k=-\infty}^{\infty} g_0(k - nM')$$

$$\times g_d(k - n'M' - \mathbf{k}_{\tilde{\tau}}[i]) e^{j2\pi \frac{\mathcal{M}_s[m']}{M'}(k-\mathbf{k}_{\tilde{\tau}}[i])} e^{-j2\pi \frac{m}{M'}k} e^{j2\pi \frac{\mathbf{v}[i]k}{\Delta f M'}}$$

$$+ \bar{\mathbf{W}}[m,n]. \tag{A.13}$$

Our goal is to obtain a closed-form solution, therefore we substitute $k' = k - n'M' - \mathbf{k}_{\tilde{\tau}}[i]$ to get

$$\bar{\mathbf{R}}_d[m,n] = \alpha \sum_{n'=0}^{N-1} \sum_{m'=0}^{M_s-1} \check{\mathbf{X}}[m',n'] \sum_{i=0}^{N_t-1} \mathbf{h}[i] e^{-j2\pi \frac{m\mathbf{k}_{\tilde{\tau}}[i]}{M'}}$$

$$\times e^{j2\pi \frac{\mathbf{v}[i]\mathbf{k}_{\tilde{\tau}}[i]}{\Delta f M'}} e^{j2\pi \frac{\mathbf{v}[i]n'}{\Delta f}} \left\{ \sum_{k'=-\infty}^{\infty} g_0(k' + \mathbf{k}_{\tilde{\tau}}[i] - (n-n')M') \right.$$

$$\left. \times g_d(k') e^{j2\pi \frac{k'}{M'}\left(\mathcal{M}_s[m']-m+\frac{\mathbf{v}[i]}{\Delta f}\right)} \right\} + \bar{\mathbf{W}}[m,n], \tag{A.14}$$

where we now focus on the section in the curly brackets. From the definitions of $g_d(.)$ and $g_0(.)$, we determine that the range of k' for a non-zero outcome yields

$$k' \in \{0, 1, \ldots, M' - M_{gi} - 1\}, \tag{A.15}$$

and

$$k' \in \{0, 1, \ldots, M' - 1\} + qM' - \mathbf{k}_{\tilde{\tau}}[i]. \tag{A.16}$$

where $q = n - n'$. The summation limits for k' then are

$$m_1 = \max\left\{0, \ qM' - \mathbf{k}_{\tilde{\tau}}[i]\right\}, \tag{A.17}$$

$$m_2 = \min\left\{-M_{gi}, \ qM' - \mathbf{k}_{\tilde{\tau}}[i]\right\} + M' - 1. \tag{A.18}$$

The only non-zero outcome occurs for $q = 0$ (i.e., OTFS symbol separation due to the guard interval), where $m_1 = 0$ and $m_2 = M' - M_{gi} - 1$. The section in curly brackets in (A.14) may now be simplified into

$$\frac{1}{M'} \sum_{k=0}^{M'-M_{gi}-1} e^{j2\pi \frac{k}{M'}\left(\mathcal{M}_s[l]-m+\frac{\mathbf{v}[i]}{\Delta f}\right)}, \tag{A.19}$$

and the FT domain input-output relation may now be expressed by

$$\bar{\mathbf{R}}_d[m,n] = \sum_{m'=0}^{M-1} \bar{\mathbf{H}}_n[m,m']\bar{\mathbf{X}}[m',n] + \bar{\mathbf{W}}[m,n],$$

where $\bar{\mathbf{H}}_n[m,m']$ matches the definition in (6.34).

A.4 ECM Derivation - Estimated CSI

The derivation follows a similar approach to Appendix A.3. The time domain RX waveform for the data part is defined (using the discrete LTV channel model) as

$$r_d(k') = \sum_{k_{\tilde{\tau}}=0}^{M_{gi}/2-1} \sum_{k_{\nu}=0}^{N-1} \bar{\mathbf{h}}[k_{\tilde{\tau}}, k_{\nu}]s_d(k' - k_{\tilde{\tau}})e^{j2\pi\frac{\mathcal{V}[k_{\nu}]k'}{n_{\nu}NM'}} + w(k'), \qquad (A.20)$$

which is expanded to

$$r_d(k') = \alpha \sum_{k_{\tilde{\tau}}=0}^{M_{gi}/2-1} \sum_{k_{\nu}=0}^{N-1} \bar{\mathbf{h}}[k_{\tilde{\tau}}, k_{\nu}] \sum_{n'=0}^{N-1} \sum_{m'=0}^{M_s-1} \check{\mathbf{X}}[m',n']g_d(k' - n'M' - k_{\tilde{\tau}})$$

$$\times e^{j2\pi\mathcal{M}_s[m']\frac{k'-k_{\tilde{\tau}}}{M'}} e^{j2\pi\frac{\mathcal{V}[k_{\nu}]k'}{n_{\nu}NM'}}, \qquad (A.21)$$

where $\check{\mathbf{X}} = \bar{\mathbf{G}}\mathbf{F}_M\bar{\mathbf{x}}\mathbf{F}_N^*$. The FT domain representation, defined by (6.29) yields

$$\bar{\mathbf{R}}_d[m,n] = \alpha \sum_{n'=0}^{N-1} \sum_{m'=0}^{M_s-1} \check{\mathbf{X}}[m',n'] \sum_{k_{\tilde{\tau}}=0}^{M_{gi}/2-1} \sum_{k_{\nu}=0}^{N-1} \bar{\mathbf{h}}[k_{\tilde{\tau}}, k_{\nu}] \sum_{k=-\infty}^{\infty} g_0(k - nM')$$

$$\times g_d(k - n'M' - k_{\tau})e^{j2\pi\frac{\mathcal{M}_s[m']}{M'}(k-k_{\tilde{\tau}})}e^{-j2\pi\frac{mk}{M'}}e^{j2\pi\frac{\mathcal{V}[k_{\nu}]k}{n_{\nu}NM'}} + \bar{\mathbf{W}}[m,n]. \qquad (A.22)$$

We now define $k' = k - n'M' - k_{\tilde{\tau}}$, therefore

$$\bar{\mathbf{R}}_d[m,n] = \alpha \sum_{n'=0}^{N-1} \sum_{m'=0}^{M_s-1} \check{\mathbf{X}}[m',n'] \sum_{k_{\tau}=0}^{M_{gi}/2-1} \sum_{k_{\nu}=0}^{N-1} \bar{\mathbf{h}}[k_{\tilde{\tau}}, k_{\nu}]e^{j2\pi\frac{\mathcal{V}[k_{\nu}]n}{n_{\nu}N}}e^{j2\pi\frac{\mathcal{V}[k_{\nu}]k_{\tilde{\tau}}}{n_{\nu}NM'}}e^{-j2\pi\frac{pk_{\tilde{\tau}}}{M'}}$$

$$\times \left\{ \sum_{k'=-\infty}^{\infty} g_0(k' + k_{\tilde{\tau}} - (n-n')M')g_d(k')e^{j2\pi\frac{k'}{M'}\left(\mathcal{M}_s[l]-m+\frac{\mathcal{V}[k_{\nu}]}{n_{\nu}NM'}\right)} \right\} + \bar{\mathbf{W}}[m,n]. \quad (A.23)$$

From the definitions of $g_d(.)$ and $g_0(.)$, we again determine the range of k' for a non-zero outcome. After some manipulations, the section in curly brackets of (A.23) is simplified to

$$\frac{1}{M'} \sum_{k=0}^{M'-M_{gi}-1} e^{j2\pi\frac{k}{M'}\left(\mathcal{M}_s[l]-m+\frac{\mathcal{V}[k_{\nu}]}{n_{\nu}NM'}\right)}, \qquad (A.24)$$

which yields the final ECM formula in (6.38).

106

A.5 CP-OTFS Channel Estimation

This section serves as a proof that the guard band and consequently the fractional delay causes interference of data with the channel estimate in CP-OTFS. Because the current OTFS literature does not offer any publications regarding CP-OTFS with embedded pilot and a guard band, the following design is only partially functional, i.e. a proper data estimation method is missing. The CP-OTFS concept presented in the remainder of this section was inspired by [52, 53, 79] with some reservations:

- The system in [52] uses an entire OTFS transmission for the pilot alone and the next transmission for data, therefore, avoiding the embedded pilot idea altogether.
- [79] presents a similar transmitter structure, however, CE is done in the time domain instead of the DD domain.
- The transmitter structure in [53] also uses multiple CPs per transmission, but the absence of guard band (i.e., absence of the guard band addition matrix $\bar{\mathbf{B}}$) makes it possible to completely remove the M-point DFT in formula (1) in [53]. In other words, $\bar{\mathbf{F}}_{M'}^* \bar{\mathbf{B}} \bar{\mathbf{F}}_M \bar{\mathbf{x}} \bar{\mathbf{F}}_N^*$ becomes $\bar{\mathbf{x}} \bar{\mathbf{F}}_N^*$.

A.5.1 Transmitter

First, let us define the CP-OTFS transmit waveform as

$$s(k) = \sum_{n=0}^{N-1} \sum_{m=0}^{M_s-1} \bar{\mathbf{X}}[m,n] g_{tx}(k - nM_x') e^{j2\pi \frac{\mathcal{M}_s[m](k-nM_{cp})}{M'}}, \qquad (A.25)$$

where $M = M_s$ is the number of active subcarriers, $\mathcal{M}_s$ is the active subcarrier set (6.4), $M_x' = M' + M_{cp}$ is the CP-OTFS symbol length and $\bar{\mathbf{X}} = \bar{\mathbf{F}}_M \bar{\mathbf{x}} \bar{\mathbf{F}}_N^*$. The DD matrix with an embedded pilot is defined as

$$\bar{\mathbf{x}}[p,q] = \begin{cases} 0 & \forall \quad p \in \mathcal{M}_\tau \cap q \in \mathcal{M}_\nu \\ \rho_0 \sqrt{M_0} & \forall \quad p = M_\tau - 1 \cap q = M_\nu - 1 \\ \text{m-QAM symbols} & \text{otherwise}, \end{cases} \qquad (A.26)$$

where the sets of indices of the pilot guard region are (the white area in Fig. 6.10)

$$\mathcal{M}_\tau := \{0, 1, \ldots 2M_\tau - 2\}, \ \mathcal{M}_\nu := \{0, 1, \ldots, 2M_\nu - 2\}, \qquad (A.27)$$

for the delay domain and Doppler domain, respectively.

A.5.2 Discrete LTV Channel Model

Similarly to UW-OTFS, in order to unify the CSI format into a single matrix $\bar{\mathbf{h}}$ with a known size, we present the discrete LTV channel, defined as

$$r(k') = \sum_{k_{\tilde{\tau}}=0}^{M_{cp}-1} \sum_{k_\nu=0}^{M_\nu-1} \bar{\mathbf{h}}[k_{\tilde{\tau}}, k_\nu] s(k' - k_{\tilde{\tau}}) e^{j2\pi \frac{k'\mathcal{V}[k_\nu]}{n_\nu N M_x'}} + w(k'), \qquad (A.28)$$

where the receiver Doppler grid is defined as

$$\mathcal{V} := \left\{ \frac{1 - M_\nu}{2}, \dots, \frac{M_\nu - 1}{2} \right\}, \qquad (A.29)$$

where M_ν must be an odd number. Notice that (A.28) involves the DSF, n_ν, as it uses a similar CE approach to the UW-OTFS. Note that $\mathcal{V}$ is defined differently for CP-OTFS to that of UW-OTFS in (6.14). While in UW-OTFS we could utilize all N Doppler grid entries (upper bounded by number of OTFS symbols N), the CE region in CP-OTFS (see Fig. 6.10) only allows M_ν entries in the Doppler grid. The dimension of the root matrix in (A.28) is therefore $M_{cp} \times M_\nu$ and not $M_{gi}/2 \times N$, as it is in UW-OTFS.

A.5.3 Input-Output Relation in the FT Domain

On the receiver of CP-OTFS, we perform the Vigner transform as

$$\bar{\mathbf{Y}}[m, n] = \sum_{k'=-\infty}^{\infty} g_0(k' - nM_x') r(k') e^{-j2\pi \frac{m(k' - nM_{cp})}{M'}}. \qquad (A.30)$$

where

$$g_0(k) = \begin{cases} 1/\sqrt{M'} & \forall \quad k \in \langle 0, M' - 1 \rangle \\ \\ 0 & \text{otherwise.} \end{cases} \qquad (A.31)$$

Next, we perform a sequence of manipulations similar to what was shown in A.3 to derive the ECM formula. Here, the input-output relation in the FT domain is given by (AWGN left out for clarity)

$$\bar{\mathbf{Y}}[m, n] = \sum_{m'=0}^{M-1} \bar{\mathbf{H}}_n[m, m'] \bar{\mathbf{X}}[m', n], \qquad (A.32)$$

where the $M' \times M$ ECM is defined as

$$\bar{\mathbf{H}}_n[p, q] = \sum_{k_{\tilde{\tau}}=0}^{M_{cp}-1} \sum_{k_\nu=0}^{M_\nu-1} \bar{\bar{\mathbf{A}}}[p, q, n, k_{\tilde{\tau}}, k_\nu] \bar{\mathbf{h}}[k_{\tilde{\tau}}, k_\nu], \qquad (A.33)$$

where the pre-calculated tensor is defined as

$$\bar{\bar{\mathbf{A}}}[p, q, n, k_{\tilde{\tau}}, k_\nu] = \frac{1}{\sqrt{MM'}} e^{-j2\pi \frac{\mathcal{M}_s[q]k_{\tilde{\tau}}}{M'}} e^{j2\pi \frac{\mathcal{V}[k_\nu]n}{n_\nu N}} \sum_{k=0}^{M'-1} e^{-j2\pi \frac{k}{M'} \left(p - \mathcal{M}_s[q] - \frac{\mathcal{V}[k_\nu]M'}{n_\nu N M_x'} \right)}. \qquad (A.34)$$

A.5.4 Channel Estimation

After transforming the RX data back into the delay-Doppler domain, we may estimate the DD channel root matrix $\bar{\mathbf{h}}$ since it is 2D circularly convoluted to the data matrix $\bar{\mathbf{x}}$ and to the embedded pilot. We start by extracting the active subcarriers of the $M' \times N$ matrix $\bar{\mathbf{Y}}$, thus reducing its size to $M \times N$ and then we perform the SFT to obtain the DD domain representation,

$$\bar{\mathbf{y}}[p,q] = \frac{1}{\sqrt{MN}} \sum_{m=0}^{M-1} \sum_{n=0}^{N-1} \bar{\mathbf{Y}}[\mathcal{M}_s[m],n] e^{j2\pi\left(\frac{pm}{M} - \frac{qn}{N}\right)}, \tag{A.35}$$

which is expanded to

$$\bar{\mathbf{y}}[p,q] = \frac{1}{\sqrt{MN}} \sum_{n=0}^{N-1} \sum_{m'=0}^{M-1} \bar{\mathbf{X}}[m',n] \sum_{k_{\tilde{\tau}}=0}^{M_{gi}-1} \sum_{k_\nu=0}^{M_\nu-1} \sum_{m=0}^{M-1} \bar{\bar{\mathbf{A}}}[\mathcal{M}_s[m],m',n,k_{\tilde{\tau}},k_\nu]$$

$$\times \bar{\mathbf{h}}[k_{\tilde{\tau}},k_\nu] e^{j2\pi\left(\frac{pm}{M} - \frac{qn}{N}\right)}. \tag{A.36}$$

We now need to extract the CE region (red bordered area in Fig. 6.10) determined by the row and column sets of indices $\mathcal{N}_\tau$ and $\mathcal{N}_\nu$, respectively. These are defined as

$$\mathcal{N}_\tau := \{0,1,\ldots M_\tau - 1\} + M_\tau - 1, \tag{A.37}$$

and

$$\mathcal{N}_\nu := \{(1-M_\nu)/2,\ldots,(M_\nu-1)/2\} + M_\nu - 1. \tag{A.38}$$

The extracted DD domain matrix of size $M_\tau \times M_\nu$ is defined as

$$\hat{\bar{\mathbf{y}}}[p,q] = \bar{\mathbf{y}}\Big[\mathcal{N}_\tau[p],\mathcal{N}_\nu[q]\Big],$$

and it is expanded to

$$\hat{\bar{\mathbf{y}}}[p,q] = \frac{1}{MN} \sum_{n=0}^{N-1} \sum_{m'=0}^{M-1} \sum_{l=0}^{M-1} \sum_{k=0}^{N-1} \bar{\mathbf{x}}[l,k] e^{-j2\pi\left(\frac{m'l}{M} - \frac{nk}{N}\right)}$$

$$\times \sum_{k_{\tilde{\tau}}=0}^{M_{cp}-1} \sum_{k_\nu=0}^{M_\nu-1} \sum_{m=0}^{M-1} \bar{\bar{\mathbf{A}}}[\mathcal{M}_s[m],m',n,k_{\tilde{\tau}},k_\nu] \bar{\mathbf{h}}[k_{\tilde{\tau}},k_\nu] e^{j2\pi\left(\frac{\mathcal{N}_\tau[p]m}{M} - \frac{\mathcal{N}_\nu[q]n}{N}\right)}. \tag{A.39}$$

At this point, we define another tensor which will include the data matrix $\bar{\mathbf{x}}$,

$$\bar{\bar{\mathbf{A}}}_x[p,q,k_{\tilde{\tau}},k_\nu] = \frac{1}{MN} \sum_{l=0}^{M-1} \sum_{k=0}^{N-1} \bar{\mathbf{x}}[l,k] \sum_{n=0}^{N-1} \sum_{m'=0}^{M-1} \sum_{m=0}^{M-1} \bar{\bar{\mathbf{A}}}[\mathcal{M}_s[m],m',n,k_{\tilde{\tau}},k_\nu]$$

$$\times e^{-j2\pi\left(\frac{m'l}{M} - \frac{nk}{N}\right)} e^{j2\pi\left(\frac{\mathcal{N}_\tau[p]m}{M} - \frac{\mathcal{N}_\nu[q]n}{N}\right)}, \tag{A.40}$$

so that (A.39) becomes

$$\hat{\bar{\mathbf{y}}}[p,q] = \sum_{k_{\tilde{\tau}}=0}^{M_{cp}-1} \sum_{k_\nu=0}^{M_\nu-1} \bar{\mathbf{h}}[k_{\tilde{\tau}}, k_\nu] \bar{\bar{\mathbf{A}}}_x[p,q,k_{\tilde{\tau}}, k_\nu]. \tag{A.41}$$

Since $\bar{\bar{\mathbf{A}}}_x$ contains both data and pilot, it is possible to split it in two separate tensors, defined as

$$\bar{\bar{\mathbf{A}}}_{x0}[p,q,k_{\tilde{\tau}}, k_\nu] = \frac{\rho_0\sqrt{M_0}}{MN} \sum_{n=0}^{N-1} \sum_{m'=0}^{M-1} \sum_{m=0}^{M-1} \bar{\bar{\mathbf{A}}}[\mathcal{M}_s[m], m', n, k_{\tilde{\tau}}, k_\nu]$$

$$\times e^{-j2\pi\left(\frac{m'l_0}{M} - \frac{nk_0}{N}\right)} e^{j2\pi\left(\frac{\mathcal{N}_\tau[p]m}{M} - \frac{\mathcal{N}_\nu[q]n}{N}\right)}, \tag{A.42}$$

for the embedded pilot part, and

$$\bar{\bar{\mathbf{A}}}_{x1}[p,q,k_{\tilde{\tau}}, k_\nu] = \frac{1}{MN} \sum_{l\in\langle 0,M-1\rangle\backslash\mathcal{M}_\tau} \sum_{k\in\mathcal{M}_\nu} \bar{\mathbf{x}}[l,k]$$

$$\times \sum_{n=0}^{N-1} \sum_{m'=0}^{M-1} \sum_{m=0}^{M-1} \bar{\bar{\mathbf{A}}}[\mathcal{M}_s[m], m', n, k_{\tilde{\tau}}, k_\nu] e^{-j2\pi\left(\frac{m'l}{M} - \frac{nk}{N}\right)} e^{j2\pi\left(\frac{\mathcal{N}_\tau[p]m}{M} - \frac{\mathcal{N}_\nu[q]n}{N}\right)}, \tag{A.43}$$

and

$$\bar{\bar{\mathbf{A}}}_{x2}[p,q,k_{\tilde{\tau}}, k_\nu] = \frac{1}{MN} \sum_{l\in\langle 0,M-1\rangle} \sum_{k\in\langle 0,N-1\rangle\backslash\mathcal{M}_\nu} \bar{\mathbf{x}}[l,k]$$

$$\times \sum_{n=0}^{N-1} \sum_{m'=0}^{M-1} \sum_{m=0}^{M-1} \bar{\bar{\mathbf{A}}}[\mathcal{M}_s[m], m', n, k_{\tilde{\tau}}, k_\nu] e^{-j2\pi\left(\frac{m'l}{M} - \frac{nk}{N}\right)} e^{j2\pi\left(\frac{\mathcal{N}_\tau[p]m}{M} - \frac{\mathcal{N}_\nu[q]n}{N}\right)}, \tag{A.44}$$

for the data and part (split in two rectangular data regions, notice the presence of the pilot guard index sets $\mathcal{M}_\tau$ and $\mathcal{M}_\nu$). We may now express $\hat{\bar{\mathbf{y}}}$ as

$$\hat{\bar{\mathbf{y}}}[p,q] = \sum_{k_{\tilde{\tau}}=0}^{M_{cp}-1} \sum_{k_\nu=0}^{M_\nu-1} \left(\bar{\bar{\mathbf{A}}}_{x0}[p,q,k_{\tilde{\tau}}, k_\nu] + \bar{\bar{\mathbf{A}}}_{x1}[p,q,k_{\tilde{\tau}}, k_\nu] + \bar{\bar{\mathbf{A}}}_{x2}[p,q,k_{\tilde{\tau}}, k_\nu] \right)$$

$$\times \bar{\mathbf{h}}[k_{\tilde{\tau}}, k_\nu]. \tag{A.45}$$

Once we have a direct relation between the CE region extraction matrix $\hat{\bar{\mathbf{y}}}$ and the root matrix $\bar{\mathbf{h}}$, we may construct the LMMSE estimator (similar to (A.36)), which would treat $\bar{\bar{\mathbf{A}}}_{x1}$ and $\bar{\bar{\mathbf{A}}}_{x2}$ as an interference.

A.5.5 Single-Tap Zero-Doppler Case

To examine the effect of the guard band, we use a simple scenario with zero Doppler frequency and a single tap, defined by

$$r(k') = h_0 s(k' - k_{\tilde{\tau},0}) + w(k'), \tag{A.46}$$

which is a *Linear-Time-Invariant* (LTI) channel and $h_0 \sim \mathcal{CN}(0,1)$. Note that in this simplified case the actual channel model (5.6) and the discrete channel model (A.28) both yield the same result, i.e., (A.46). The input-output relation is given by

$$\bar{\mathbf{Y}}[m,n] = \sum_{m'=0}^{M-1} \bar{\mathbf{H}}[m,m']\bar{\mathbf{X}}[m',n], \qquad (A.47)$$

where the $M' \times M$ ECM, no longer a function of n, is defined as

$$\bar{\mathbf{H}}[p,q] = \frac{h_0\sqrt{M'}}{\sqrt{M}}e^{-j2\pi\frac{\mathcal{M}_s[q]k_{\tilde{\tau},0}}{M'}}\delta\big((p - \mathcal{M}_s[q])_{M'}\big). \qquad (A.48)$$

The extraction matrix (A.45) is simplified to

$$\hat{\bar{\mathbf{y}}}[p,q] = h_0\big(\bar{\mathbf{A}}_{x0}[p,q] + \bar{\mathbf{A}}_{x1}[p,q] + \bar{\mathbf{A}}_{x2}[p,q]\big), \qquad (A.49)$$

where

$$\bar{\mathbf{A}}_{x0}[p,q] = \frac{\rho_0\sqrt{M_0 M'}}{M\sqrt{M}}\sum_{m=0}^{M-1}e^{-j2\pi\frac{\mathcal{M}_s[m]k_{\tilde{\tau},0}}{M'}}e^{j2\pi\frac{m(\mathcal{N}_\tau[p]-l_0)}{M}}\delta\big((\mathcal{N}_\nu[q] - k_0)_N\big), \qquad (A.50)$$

for the embedded pilot part, and

$$\bar{\mathbf{A}}_{x1}[p,q] = \frac{\sqrt{M'}}{M\sqrt{M}}\sum_{l\in\langle 0,M-1\rangle\setminus\mathcal{M}_\tau}\sum_{k\in\mathcal{M}_\nu}\bar{\mathbf{x}}[l,k]$$

$$\times\sum_{m=0}^{M-1}e^{-j2\pi\frac{\mathcal{M}_s[m]k_{\tilde{\tau},0}}{M'}}e^{j2\pi\frac{m(\mathcal{N}_\tau[p]-l)}{M}}\delta\big((\mathcal{N}_\nu[q] - k)_N\big), \qquad (A.51)$$

and

$$\bar{\mathbf{A}}_{x2}[p,q] = \frac{\sqrt{M'}}{M\sqrt{M}}\sum_{l\in\langle 0,M-1\rangle}\sum_{k\in\langle 0,N-1\rangle\setminus\mathcal{M}_\nu}\bar{\mathbf{x}}[l,k]$$

$$\times\sum_{m=0}^{M-1}e^{-j2\pi\frac{\mathcal{M}_s[m]k_{\tilde{\tau},0}}{M'}}e^{j2\pi\frac{m(\mathcal{N}_\tau[p]-l)}{M}}\delta\big((\mathcal{N}_\nu[q] - k)_N\big), \qquad (A.52)$$

for the data part. The presence of $\delta\big((\mathcal{N}_\nu[q]-k_0)_N\big)$ in (A.50) indicates that only the column index q_0 that satisfies $\mathcal{N}_\nu[q_0] = k_0$ contains the CSI. Therefore, we evaluate this particular column of $\hat{\bar{\mathbf{y}}}$ as

$$\hat{\bar{\mathbf{y}}}[p,q_0] = h_0\big(\bar{\mathbf{A}}_{x0}[p,q_0] + \bar{\mathbf{A}}_{x1}[p,q_0] + \bar{\mathbf{A}}_{x2}[p,q_0]\big), \qquad (A.53)$$

where

$$\bar{\mathbf{A}}_{x0}[p,q_0] = \frac{\rho_0\sqrt{M_0 M'}}{M\sqrt{M}}\sum_{m=0}^{M-1}e^{-j2\pi\frac{\mathcal{M}_s[m]k_{\tilde{\tau},0}}{M'}}e^{j2\pi\frac{m(\mathcal{N}_\tau[p]-l_0)}{M}}, \qquad (A.54)$$

and from the data part we have

$$\bar{\mathbf{A}}_{x1}[p,q_0] = \frac{\sqrt{M'}}{M\sqrt{M}}\sum_{l\in\langle 0,M-1\rangle\setminus\mathcal{M}_\tau}\sum_{m=0}^{M-1}e^{-j2\pi\frac{\mathcal{M}_s[m]k_{\tilde{\tau},0}}{M'}}e^{j2\pi\frac{m(\mathcal{N}_\tau[p]-l)}{M}}\bar{\mathbf{x}}[l,k_0], \qquad (A.55)$$

and $\bar{\mathbf{A}}_{x2}[p, q_0] = 0 \ \forall \ p \in \langle 0, M_\tau - 1 \rangle$. While $\bar{\mathbf{A}}_{x0}[p, q_0] \ \forall \ p \in \langle 0, M_\tau - 1 \rangle$ is a fully deterministic complex-valued vector, we can see that $\bar{\mathbf{A}}_{x1}[p, q_0] \ \forall \ p \in \langle 0, M_\tau - 1 \rangle$ is a random complex-valued vector, therefore, the CSI in (A.53) is damaged by interference.

Finally, we may reveal the cause of the interference by removing the guard band. This is achieved if we replace $\mathcal{M}_s[m]/M'$ by m/M, which yields

$$\bar{\mathbf{A}}_{x0}[p, q_0] = \frac{\rho_0 \sqrt{M_0 M'}}{M \sqrt{M}} \sum_{m=0}^{M-1} e^{j2\pi \frac{m(\mathcal{N}_\tau[p] - l_0 - k_{\tilde{\tau},0})}{M}} = \frac{\rho_0 \sqrt{M_0 M'}}{\sqrt{M}} \delta\big((\mathcal{N}_\tau[p] - l_0 - k_{\tilde{\tau},0})_M\big),$$

(A.56)

for the pilot part and

$$\bar{\mathbf{A}}_{x1}[p, q_0] = \frac{\sqrt{M'}}{M \sqrt{M}} \sum_{l \in \langle 0, M-1 \rangle \setminus \mathcal{M}_\tau} \bar{\mathbf{x}}[l, k_0] \sum_{m=0}^{M-1} e^{j2\pi \frac{m(\mathcal{N}_\tau[p] - l - k_{\tilde{\tau},0})}{M}},$$

$$\bar{\mathbf{A}}_{x1}[p, q_0] = \frac{\sqrt{M'}}{\sqrt{M}} \sum_{l \in \langle 0, M-1 \rangle \setminus \mathcal{M}_\tau} \bar{\mathbf{x}}[l, k_0] \delta\big((\mathcal{N}_\tau[p] - l - k_{\tilde{\tau},0})_M\big), \qquad \text{(A.57)}$$

for the data part. We can easily find that $\mathcal{N}_\tau[p] - l - k_{\tilde{\tau},0} \in \langle 1 - M, -1 \rangle$, therefore, to remove the Dirac delta function and obtain the only non-zero outcome, we would need $\mathcal{N}_\tau[p] - l - k_{\tilde{\tau},0} = 0$. However, we must also respect the summation range which is $l \in \langle 0, M-1 \rangle \setminus \mathcal{M}_\tau$ or equivalently, $l \in \langle 2M_\tau - 1, M - 1 \rangle$. Since there is no conjunction, we obtain $\bar{\mathbf{A}}_{x1}[p, q_0] = 0 \ \forall \ p \in \langle 0, M_\tau - 1 \rangle$. We have now proved that the guard band's presence was causing interference to the channel estimate.

Bibliography

[1] R. Zedka, M. Bobula, J. Blumenstein, and L. Polak, "Space-time line code based on quasi-orthogonal design," in *2022 32nd International Conference Radioelektronika (RADIOELEKTRONIKA)*, 2022, pp. 01–05.

[2] R. Zedka, M. Bobula, J. Blumenstein, L. Polak, and M. Rupp, "Full-rate space-time line code with asymptotic SNR gain," *IEEE Communications Letters*, vol. 27, no. 5, pp. 1307–1311, May 2023.

[3] R. Zedka, T. Gotthans, R. Marsalek, J. Blumenstein, and M. Bobula, "SC-FDE and OFDM in MISO frequency-selective fading channels," in *2020 30th International Conference Radioelektronika (RADIOELEKTRONIKA)*. IEEE, Apr. 2020, pp. 1–5.

[4] R. Zedka, T. Gotthans, and R. Marsalek, "Spectral efficient time-domain equalization single-carrier system," in *2021 31th International Conference Radioelektronika (RADIOELEKTRONIKA)*. IEEE, 2021, pp. 1–5.

[5] L. Polak, J. Milos, R. Zedka, J. Blumenstein, and C. Mecklenbräuker, "BER and throughput performances of IEEE 802.11ay SC-PHY over measured 60 GHz indoor channels," *Telecommunication Systems*, vol. 80, no. 4, pp. 573–587, Jun. 2022.

[6] R. Maršálek, R. Zedka, E. Zöchmann, J. Vychodil, R. Závorka, G. Ghiaasi, and J. Blumenstein, "Persistent homology approach for human presence detection from 60 ghz OTFS transmissions," *Sensors (Basel, Switzerland)*, vol. 23, no. 4, p. 2224, 2023.

[7] R. Zedka, R. Marsalek, and M. Bobula, "Unique word orthogonal time frequency space," *IEEE Transactions on Wireless Communications*, In submission.

[8] J. Joung, "Space-time line code," *IEEE Access*, vol. 6, pp. 1023–1041, 2018.

[9] S. chan Lim and J. Joung, "Transmit antenna selection for space-time line code systems," *IEEE transactions on communications*, vol. 69, no. 2, pp. 786–798, 2021.

[10] J. Joung, J. Choi, and B. C. Jung, "Double space-time line codes," *IEEE transactions on vehicular technology*, vol. 69, no. 2, pp. 2316–2321, 2020.

[11] S. chan Lim and J. Joung, "Ergodic capacity of space-time line code systems with transmit antenna selection," *IEEE Transactions on vehicular technology*, pp. 1–6, early access.

[12] W. Su and X.-g. Xia, "Signal constellations for quasi-orthogonal space-time block codes with full diversity," *IEEE Transactions on Information Theory*, vol. 50, no. 10, pp. 2331–2347, 2004.

[13] J.-K. Zhang, J. Liu, and K. M. Wong, "Linear toeplitz space time block codes," in *Proceedings. International Symposium on Information Theory, 2005. ISIT 2005.*, 2005, pp. 1942–1946.

[14] Y. Shang and X.-G. Xia, "Space–time block codes achieving full diversity with linear receivers," *IEEE Transactions on Information Theory*, vol. 54, no. 10, pp. 4528–4547, Oct. 2008.

[15] H. Wang, X.-G. Xia, Q. Yin, and B. Li, "A family of space-time block codes achieving full diversity with linear receivers," *IEEE Transactions on Communications*, vol. 57, no. 12, pp. 3607–3617, Dec. 2009.

[16] J. Choi and J. Joung, "Generalized space-time line code with receive combining for MIMO systems," *IEEE Systems journal*, vol. 16, no. 2, pp. 1–12, Mar. 2021.

[17] S.-C. Lim and J. Joung, "Full-rate space–time line code for four receive antennas," *IEEE Wireless Communications Letters*, vol. 11, no. 3, pp. 602–606, Mar. 2022.

[18] H. Xu, N. Pillay, and F. Yang, "Rotated golden codewords based space-time line code systems," *IEEE Access*, vol. 10, pp. 54 784–54 793, May 2022.

[19] H. Jafarkhani, "A quasi-orthogonal space-time block code," *IEEE Transactions on Communications*, vol. 49, no. 1, pp. 1–4, Jan. 2001.

[20] M. Rupp and C. F. Mecklenbräuker, "Asymptotic behavior of extended Alamouti schemes for large number of transmit and receive antennas," in *2006 Fortieth Asilomar Conference on Signals, Systems and Computers*, May 2006, pp. 1279–1283.

[21] C. F. Mecklenbräuker and M. Rupp, "Generalized Alamouti codes for trading quality of service against data rate in MIMO UMTS," *EURASIP Journal on advances in signal processing*, vol. 2004, no. 5, pp. 1279–1283, Dec. 2004.

[22] B. Sklar, "Rayleigh fading channels in mobile digital communication systems part I: Characterization," *IEEE Communications Magazine*, vol. 35, no. 7, p. 90, 1997.

[23] F. Yilmaz, "On the relationships between average channel capacity, average bit error rate, outage probability, and outage capacity over additive white gaussian noise channels," *IEEE Transactions on Communications*, vol. 68, no. 5, pp. 2763–2776, May 2020.

[24] J. Tellado, *Multicarrier modulation with low PAR*. Boston: Kluwer Academic Publishers, 2000.

[25] M. Khan and B. Rajan, "Single-symbol maximum likelihood decodable linear stbcs," *IEEE Transactions on Information Theory*, vol. 52, no. 5, pp. 2062–2091, May 2006.

[26] P. Balaban and J. Salz, "Optimum diversity combining and equalization in digital data transmission with applications to cellular mobile radio. theoretical considerations," *IEEE Transactions on Communications*, vol. 40, no. 5, pp. 885–894, May 1992.

[27]

[28] V. Tarokh, H. Jafarkhani, and A. C. Calderbank, "Space-time block codes from orthogonal designs," *IEEE Transactions on Information Theory*, vol. 45, no. 5, pp. 1456–1467, Jul. 1999.

[29] S. Alamouti, "A simple transmit diversity technique for wireless communications," *IEEE Journal on Selected Areas in Communications*, vol. 16, no. 8, pp. 1451–1458, Oct. 1998.

[30] O. Tirkkonen, A. Boariu, and A. Hottinen, "Minimal non-orthogonality rate 1 space-time block code for 3+ tx antennas," in *2000 IEEE Sixth International Symposium on Spread Spectrum Techniques and Applications. ISSTA 2000. Proceedings (Cat. No.00TH8536)*, vol. 2. IEEE, Sep. 2000, pp. 429–432 vol.2.

[31] W. Su and X.-G. Xia, "On space-time block codes from complex orthogonal designs," *Wireless Personal Communications*, vol. 25, no. 1, pp. 1–26, Apr. 2003.

[32] S. Diggavi, N. Al-dhahir, A. Stamoulis, and A. Calderbank, "Differential space-time coding for frequency-selective channels," *IEEE Communications Letters*, vol. 6, no. 6, pp. 253–255, 2002.

[33] M. Rupp, C. Mecklenbräuker, and G. Gritsch, "High diversity with simple space time block-codes and linear receivers," in *GLOBECOM '03. IEEE Global Telecommunications Conference*, Jan. 2004, pp. 302–306.

[34] I. S. I. S. Gradshteyn, A. Jeffrey, and I. M. I. M. Ryzhik, *Table of integrals, series, and products*, 7th ed. San Diego: Academic Press, 2007.

[35] I. M. Tanash and T. Riihonen, "Global minimax approximations and bounds for the Gaussian Q-function by sums of exponentials," *IEEE Transactions on Communications*, vol. 68, no. 10, pp. 6514–6524, Jul. 2020.

[36] B. Badic, M. Rupp, and H. Weinrichter, "Quasi-orthogonal space-time block codes: Approaching optimality," in *2005 13th European Signal Processing Conference*, Apr. 2005, pp. 1–8.

[37] G. E. Andrews, R. Askey, and R. Roy, *Special Functions*, 1st ed. Cambridge: Cambridge University Press, 1999.

[38] R. Hadani, S. Rakib, M. Tsatsanis, A. Monk, A. J. Goldsmith, A. F. Molisch, and R. Calderbank, "Orthogonal time frequency space modulation," in *2017 IEEE Wireless Communications and Networking Conference (WCNC)*, 2017, pp. 1–6.

[39] G. D. Surabhi, R. M. Augustine, and A. Chockalingam, "On the diversity of uncoded OTFS modulation in doubly-dispersive channels," *IEEE Transactions on Wireless Communications*, vol. 18, no. 6, pp. 3049–3063, Jun. 2019.

[40] P. Raviteja, Y. Hong, E. Viterbo, and E. Biglieri, "Practical pulse-shaping waveforms for reduced-cyclic-prefix OTFS," *IEEE Transactions on Vehicular Technology*, vol. 68, no. 1, pp. 957–961, Jan. 2019.

[41] P. Raviteja, K. T. Phan, Y. Hong, and E. Viterbo, "Interference cancellation and iterative detection for orthogonal time frequency space modulation," *IEEE Transactions on Wireless Communications*, vol. 17, no. 10, pp. 6501–6515, Oct. 2018.

[42] P. Raviteja, K. T. Phan, and Y. Hong, "Embedded pilot-aided channel estimation for OTFS in delay–Doppler channels," *IEEE Transactions on Vehicular Technology*, vol. 68, no. 5, pp. 4906–4917, May 2019.

[43] H. Liu, Y. Liu, M. Yang, and Q. Zhang, "On the characterizations of OTFS modulation over multipath rapid fading channel," *IEEE Transactions on Wireless Communications*, vol. 22, no. 3, pp. 2008–2021, Mar. 2023.

[44] L. Gaudio, G. Colavolpe, and G. Caire, "OTFS vs. OFDM in the presence of sparsity: A fair comparison," *IEEE Transactions on Wireless Communications*, vol. 21, no. 6, pp. 4410–4423, Jun. 2022.

[45] A. Pfadler, P. Jung, and S. Stanczak, "Mobility modes for pulse-shaped OTFS with linear equalizer," in *GLOBECOM 2020 - 2020 IEEE Global Communications Conference*, Feb. 2021, pp. 1–6.

[46] S. Tiwari, S. S. Das, and V. Rangamgari, "Low complexity LMMSE receiver for OTFS," *IEEE Communications Letters*, vol. 23, no. 12, pp. 2205–2209, Dec. 2019.

[47] X. He, P. Fan, and Q. Wang, "A two-stage channel estimation algorithm for OTFS in fractional Doppler channels," *IEEE Communications Letters*, vol. 27, no. 7, pp. 1839–1843, Jul. 2023.

[48] Z. Wei, W. Yuan, S. Li, J. Yuan, and D. W. K. Ng, "Off-grid channel estimation with sparse bayesian learning for otfs systems," *IEEE Transactions on Wireless Communications*, vol. 21, no. 9, pp. 7407–7426, Sep. 2022.

[49] A. RezazadehReyhani, A. Farhang, M. Ji, R. R. Chen, and B. Farhang-Boroujeny, "Analysis of discrete-time MIMO OFDM-based orthogonal time frequency space modulation," in *2018 IEEE International Conference on Communications (ICC)*, 2018, pp. 1–6.

[50] S. E. Zegrar and H. Arslan, "A novel cyclic prefix configuration for enhanced reliability and spectral efficiency in OTFS systems," *IEEE Wireless Communications Letters*, vol. 12, no. 5, pp. 888–892, May. 2023.

[51] A. Farhang, A. RezazadehReyhani, L. E. Doyle, and B. Farhang-Boroujeny, "Low complexity modem structure for OFDM-based orthogonal time frequency space modulation," *IEEE Wireless Communications Letters*, vol. 7, no. 3, pp. 344–347, Jun. 2018.

[52] N. Hashimoto, N. Osawa, K. Yamazaki, and S. Ibi, "Channel estimation and equalization for CP-OFDM-based OTFS in fractional Doppler channels," in *2021 IEEE International Conference on Communications Workshops (ICC Workshops)*, 2021, pp. 1–7.

[53] X. Huang, A. Farhang, and R.-R. Chen, "Channel estimation and turbo equalization for coded OTFS and OFDM: A comparison," *IEEE Wireless Communications Letters*, vol. 12, no. 9, pp. 1613–1617, Sep. 2023.

[54] P. Raviteja, K. T. Phan, Q. Jin, Y. Hong, and E. Viterbo, "Low-complexity iterative detection for orthogonal time frequency space modulation," in *2018 IEEE Wireless Communications and Networking Conference (WCNC)*, 2018, pp. 1–6.

[55] S. Li, W. Yuan, Z. Wei, R. Schober, and G. Caire, "Orthogonal time frequency space modulation—part ii: Transceiver designs," *IEEE Communications Letters*, vol. 27, no. 1, pp. 9–13, Jan. 2023.

[56] W.-C. Chen, C.-H. Lu, and C.-D. Chung, "Spectrally precoded OTFS modulation," in *2022 IEEE 96th Vehicular Technology Conference (VTC2022-Fall)*, 2022, pp. 1–7.

[57] H. Witschnig, T. Mayer, A. Springer, A. Koppler, L. Maurer, M. Huemer, and R. Weigel, "A different look on cyclic prefix for SC/FDE," in *The 13th IEEE International Symposium on Personal, Indoor and Mobile Radio Communications*, vol. 2, 2002, pp. 824–828 vol.2.

[58] H. Witschnig, T. Mayer, A. Springer, L. Maurer, M. Huemer, and R. Weigel, "The advantages of a known sequence versus cyclic prefix in a SC/FDE system," in *The 5th International Symposium on Wireless Personal Multimedia Communications*, vol. 3, 2002, pp. 1328–1332 vol.3.

[59] J. Coon, M. Beach, and J. Mcgeehan, "Minimum mean-square error frequency-domain equalisation in unique-word based single-carrier systems," *Electronics letters*, vol. 40, no. 16, pp. 1003–1005, 2004.

[60] M. Huemer, C. Hofbauer, and J. B. Huber, "Unique word prefix in SC/FDE and OFDM," in *2010 IEEE Globecom Workshops*. IEEE, 2010, pp. 1296–1301.

[61] J. Coon, M. Sandell, M. Beach, and J. McGeehan, "Channel and noise variance estimation and tracking algorithms for unique-word based single-carrier systems," *IEEE Transactions on Wireless Communications*, vol. 5, no. 6, pp. 1488–1496, Jun. 2006.

[62] M. Huemer, A. Onic, and C. Hofbauer, "Classical and bayesian linear data estimators for unique word OFDM," *IEEE Transactions on Signal Processing*, vol. 59, no. 12, pp. 6073–6085, Aug. 2011.

[63] M. Huemer, C. Hofbauer, and J. B. Huber, "Non-systematic complex number RS coded OFDM by unique word prefix," *IEEE Transactions on Signal Processing*, vol. 60, no. 1, pp. 285–299, 2012.

[64] H. Steendam, "On the selection of the redundant carrier positions in UW-OFDM," *IEEE Transactions on Signal Processing*, vol. 61, no. 5, pp. 1112–1120, Mar. 2013.

[65] C. S. Reddy, P. Priya, D. Sen, and C. Singhal, "Spectral efficient modem design with OTFS modulation for vehicular-IoT system," *IEEE Internet of Things Journal*, vol. 10, no. 3, pp. 2444–2458, Feb. 2023.

[66] Z. Tang, R. C. Cannizzaro, G. Leus, and P. Banelli, "Pilot-assisted time-varying channel estimation for OFDM systems," *IEEE Transactions on Signal Processing*, vol. 55, no. 5, pp. 2226–2238, May 2007.

[67] P. Cheng, Z. Chen, Y. Rui, Y. J. Guo, L. Gui, M. Tao, and Q. T. Zhang, "Channel estimation for OFDM systems over doubly selective channels: A distributed compressive sensing based approach," *IEEE Transactions on Communications*, vol. 61, no. 10, pp. 4173–4185, Oct. 2013.

[68] L. Zhao, W. Guo, Y. Liu, J. Yang, and W. Wang, "Pilot optimization for OFDM-based OTFS systems over doubly selective channels," in *GLOBECOM 2020 - 2020 IEEE Global Communications Conference*, 2020, pp. 1–6.

[69] F. Long, K. Niu, and J. Lin, "Joint channel estimation and equalization for OTFS based on EP," in *2021 IEEE Global Communications Conference (GLOBECOM)*, 2021, pp. 01–06.

[70] Y. Liu, Y. L. Guan, and D. G. G., "Near-optimal BEM OTFS receiver with low pilot overhead for high-mobility communications," *IEEE Transactions on Communications*, vol. 70, no. 5, pp. 3392–3406, May 2022.

[71] S. P. S. and A. Farhang, "A practical pilot for channel estimation of OTFS," in *ICC 2023 - IEEE International Conference on Communications*, 2023, pp. 1319–1325.

[72] X. Huang, A. Farhang, and R.-R. Chen, "Channel estimation and turbo equalization for coded OTFS and OFDM: A comparison," *IEEE Wireless Communications Letters*, vol. 12, no. 9, pp. 1613–1617, Sep. 2023.

[73] Y. Zhang, X. Zhu, Y. Liu, Y. Jiang, Y. L. Guan, D. G. G., and V. K. N. Lau, "A cross-domain iterative OTFS receiver for sparse doubly selective channels," *IEEE Wireless Communications Letters*, vol. 13, no. 1, pp. 54–58, Jan. 2024.

[74] Y. Liu, Y. L. Guan, and D. G. G., "Turbo BEM OTFS receiver with optimized superimposed pilot power," *IEEE Transactions on Communications*, vol. 72, no. 1, pp. 601–617, Jan. 2024.

[75] R. Bomfin, M. Chafii, A. Nimr, and G. Fettweis, "A robust baseband transceiver design for doubly-dispersive channels," *IEEE Transactions on Wireless Communications*, vol. 20, no. 8, pp. 4781–4796, Aug. 2021.

[76] ——, "Channel estimation for MIMO space time coded OTFS under doubly selective channels," in *2021 IEEE International Conference on Communications Workshops (ICC Workshops)*, 2021, pp. 1–6.

[77] S. Ehsanfar, M. Chafii, and G. P. Fettweis, "On UW-based transmission for MIMO multi-carriers with spatial multiplexing," *IEEE Transactions on Wireless Communications*, vol. 19, no. 9, pp. 5875–5890, Jun. 2020.

[78] S. Ehsanfar, K. Moessner, A. K. Gizzini, and M. Chafii, "Performance comparison of IEEE 802.11p, 802.11bd-draft and a unique-word-based PHY in doubly-dispersive channels," in *2022 IEEE Wireless Communications and Networking Conference (WCNC)*. Austin, Texas, USA: IEEE, 2022, pp. 1815–1820.

[79] S. S. Das, V. Rangamgari, S. Tiwari, and S. C. Mondal, "Time domain channel estimation and equalization of CP-OTFS under multiple fractional Dopplers and residual synchronization errors," *IEEE Access*, vol. 9, pp. 10 561–10 576, Dec. 2020.

[80] H.-T. Sheng and W.-R. Wu, "Time-frequency domain channel estimation for OTFS systems," *IEEE Transactions on Wireless Communications*, vol. Early Access, pp. 1–1, 2023.

[81] H. B. Mishra, P. Singh, A. K. Prasad, and R. Budhiraja, "OTFS channel estimation and data detection designs with superimposed pilots," *IEEE Transactions on Wireless Communications*, vol. 21, no. 4, pp. 2258–2274, Apr. 2022.

[82] X. Wang, X. Shi, J. Wang, and J. Song, "On the Doppler squint effect in OTFS systems over doubly-dispersive channels: Modeling and evaluation," *IEEE Transactions on Wireless Communications*, vol. 22, no. 12, pp. 8781–8796, Dec. 2023.

Symbols and abbreviations

BER   Bit Error Ratio

SNR   Signal to Noise Ratio

PAPR   Peak to Average Power Ratio

PMEPR Peak to Mean-Average Power Ratio

TX   Transmitter

RX   Receiver

FD   Frequency Domain

FDE   Frequency Domain Equalization

TD   Time Domain

CP   Cyclic Prefix

SC   Single Carrier

UW   Unique Word

QAM   Quadrature Amplitude Modulation

TDD   Time Division Duplex

MSE   Mean Square Error

MIMO Multiple Input Multiple Output

MISO   Multiple Input Single Output

SIMO   Single Input Multiple Output

SISO   Single Input Single Output

MRC   Maximum Ratio Combining

MRT   Maximum Ratio Transmission

EBF   Eigen-beamforming

ZF   Zero Forcing

LMMSE Linear Minimum Mean Square Error

IoT	Internet of Things
CSI	Channel State Information
PDF	Probability Density Function
CDF	Cummulative Density Function
RF	Radio Frequency
WLAN	Wireless Local Area Network
AWGN	Additive White Gaussian Noise
CFO	Carrier Frequency Offset
STC	Space Time Code
STBC	Space Time Block Code
STTC	Space Time Trellis Code
ML	Maximum Likelihood
CISTBC	Coordinate-Interleaved Space-Time Block Code
ASNR	Average Signal to Noise Ratio
ABER	Average Bit Error Rate
BPSK	Binary Phase Shift Keying
OSTBC	Orthogonal Space Time Block Code
OSTBCs	Orthogonal Space Time Block Codes
QSTBC	Quasi-orthogonal Space Time Block Code
STLC	Space Time Line Code
OSTLC	Orthogonal Space Time Line Code
QSTLC	Quasi-orthogonal Space Time Line Code
TAS	Transmit Antenna Selection
CIR	Channel Impulse Response
PDP	Power Delay Profile

CFR	Channel Frequency Response
FFT	Fast Fourier Transform
IFFT	Inverse Fast Fourier Transform
LOTUS	Law Of The Unconscious Statistician
OFDM	Orthogonal Frequency Domain Multiplexing
SC-FDE	Single-Carrier Frequency Domain Equalization
MSE	Mean Square Error
BEM	Basis Expansion Model
GCE-BEM	Generalized Complex-Exponential Basis Extension Model
CE-BEM	Complex-Exponential Basis Extension Model
NMSE	Normalized Mean Square Error
GI	Guard Interval
ISI	Inter-Symbol Interference
IDI	Inter-Doppler Interference
ICI	Inter-Carrier Interference
OOB	Out-of-Band
BLUE	Best Linear Unbiased Estimator
UW-SC-FDE	Unique-Word Single-Carrier Frequency Domain Equalization
UW-OFDM	Unique-Word Orthogonal Frequency Division Multiplexing
WLAN	Wireless Local Area Network
PSD	Power Spectral Density
LTV	Linear-Time-Variant
LTI	Linear-Time-Invariant
OTFS	Orthogonal Time Frequency Space
UW-OTFS	Unique-Word Orthogonal Time Frequency Space

CP-OTFS	Cyclic-Prefix Orthogonal Time Frequency Space
DSF	Doppler Scaling Factor
DSE	Doppler Squint Effect
SFT	Symplectic Fourier Transform
ISFT	Inverse Symplectic Fourier Transform
DFT	Discrete Fourier Transform
IDFT	inverse Discrete Fourier Transform
FT	Frequency-Time
DD	Delay-Doppler
IBI	Inter-Block-Interference
CE	Channel Estimation
ECM	Equivalent Channel Matrix
CME	Complex Multiplication Equivalent
LU	Lower-Upper
ZC	Zadoff-Chu
$(.)^*$	complex conjugate
$(.)^T$	matrix transpose
$(.)^H$	Hermitian transpose
$\text{tr}\{.\}$	trace operator
$\text{E}\{.\}$	expectation operator
$diag\{.\}$	operator for turning vectors into diagonal matrices
$\otimes$	Kronecker product
$s(.)$	discrete sequence
$\mathbf{s}, \mathbf{S}$	column vector
$\bar{\mathbf{A}}$	matrix

$\bar{\bar{\mathbf{A}}}$ tensor (3 or more dimensions)

$\bar{\mathbf{F}}$ DFT matrix

List of Figures

List of Tables